

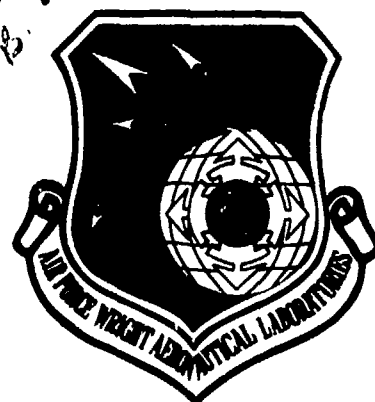
AD A090497

LEVEL II

(2)

AFML-TR-79-4209

FATIGUE CRACK PROPAGATION AND CORROSION
FATIGUE OF AF 1410 STEEL



S. D. ANTOLOVICH

DEPARTMENT OF MATERIALS SCIENCE AND METALLURGICAL ENGINEERING
UNIVERSITY OF CINCINNATI
CINCINNATI, OHIO 45221

JANUARY 1980



TECHNICAL REPORT AFML-TR-79-4209

Report Period May 1976 - May 1978

Approved for public release; distribution unlimited.

AIR FORCE MATERIALS LABORATORY
AIR FORCE WRIGHT AERONAUTICAL LABORATORIES
AIR FORCE SYSTEMS COMMAND
WRIGHT-PATTERSON AIR FORCE BASE, OHIO 45433

DDC FILE COPY

80 10 10 143

NOTICE

When Government drawings, specifications, or other data are used for any purpose other than in connection with a definitely related Government procurement operation, the United States Government thereby incurs no responsibility nor any obligation whatsoever; and the fact that the government may have formulated, furnished, or in any way supplied the said drawings, specifications, or other data, is not to be regarded by implication or otherwise as in any manner licensing the holder or any other person or corporation, or conveying any rights or permission to manufacture use, or sell any patented invention that may in any way be related thereto.

This report has been reviewed by the Office of Public Affairs (ASD/PA) and is releasable to the National Technical Information Service (NTIS). At NTIS, it will be available to the general public, including foreign nations.

This technical report has been reviewed and is approved for publication.

LR Bidwell

Lawrence R. Bidwell
Program Manager

FOR THE COMMANDER

G. E. Eichelman
G. E. Eichelman, Chief
Structural Metals Branch
Metals and Ceramics Division

"If your address has changed, if you wish to be removed from our mailing list, or if the addressee is no longer employed by your organization please notify AFML/LLS, W-PAFB, OH 45433 to help us maintain a current mailing list".

Copies of this report should not be returned unless return is required by security considerations, contractual obligations, or notice on a specific document.

SECURITY CLASSIFICATION OF THIS PAGE (When Data Entered)

19 REPORT DOCUMENTATION PAGE		READ INSTRUCTIONS BEFORE COMPLETING FORM
1. REPORT NUMBER AFML-TR-79-4209	2. GOVT ACCESSION NO. AD-A090497	3. RECIPIENT'S CATALOG NUMBER 7
4. TITLE (and Subtitle) Fatigue Crack Propagation and Corrosion Fatigue of AF 1410 Steel.		5. TYPE OF REPORT & PERIOD COVERED Technical Report. May 1976 - May 1978
7. AUTHOR(s) S. D. ANTOLOVICH		8. CONTRACT OR GRANT NUMBER(s) F33615-76-C-5227
9. PERFORMING ORGANIZATION NAME AND ADDRESS Department of Materials Science and Metallurgical Engineering University of Cincinnati, Cincinnati, OH 45221		10. PROGRAM ELEMENT, PROJECT, TASK AREA & WORK UNIT NUMBERS Project 7351
11. CONTROLLING OFFICE NAME AND ADDRESS Air Force Materials Laboratory Air Force Systems Command Wright-Patterson Air Force Base, OH 45433		12. REPORT DATE January 1980
14. MONITORING AGENCY NAME & ADDRESS (if different from Controlling Office) 121		13. NUMBER OF PAGES 122
		15. SECURITY CLASS. (of this report) Unclassified
		15a. DECLASSIFICATION/DOWNGRADING SCHEDULE
16. DISTRIBUTION STATEMENT (of this Report) Approved for Public Release; Distribution Unlimited		
17. DISTRIBUTION STATEMENT (of the abstract entered in Block 20, if different from Report)		
18. SUPPLEMENTARY NOTES		
19. KEY WORDS (Continue on reverse side if necessary and identify by block number) Steel AF 1410 Fatigue Crack Production Corrosion Fatigue Low Cycle Fatigue		
20. ABSTRACT (Continue on reverse side if necessary and identify by block number) The fatigue crack propagation (FCP) and corrosion fatigue (CF) behavior of AF 1410 steel was studied, primarily in the 950°F/5h aged condition. In addition some LCF tests were carried out to investigate fundamental mechanisms. It was shown that the FCP behavior of this steel was similar to many other alloy steels and could be described by conventional models. The material was sensitive to environmental effects in lab air at low frequencies		

DTIC
SELECTED
OCT 16 1980

20.

and stress intensities. ←

In CF, the rate was significantly accelerated in a 3 1/2% NaCl solution and this acceleration was most pronounced at low frequencies, stress intensities and at higher temperatures. The results were consistent with a thermally activated process having an activation energy of 2-3 k-cal/mol. The LCF behavior was such that a very large Coffin-Manson exponent characterized the process. The value was about 1.2 and, through a theoretical model developed by the author was consistent with the FCP test results. Some LCF and FCP tests were run on materials aged at 750°F and 975°F to study the effect of different phases at a constant strength level. The 750°F aged material exhibited the longest LCF life but this was not reflected in the FCP test results.

FOREWORD

This investigation was conducted by Dr. S. D. Antolovich of the University of Cincinnati for the Air Force Materials Laboratory, Wright-Patterson Air Force Base, Ohio under Contract F33615-76-C-5227. Dr. Lawrence R. Bidwell served as the Air Force Program Manager. The program is documented under Project 7351, Task 735101.

Accession For	
NTIS GRA&I	<input checked="checked" type="checkbox"/>
DTIC TAB	<input type="checkbox"/>
Unannounced	<input type="checkbox"/>
Justification	
By	
Distribution/	
Availability Codes	
Dist	Avail and/or
	Special
A	

TABLE OF CONTENTS

	<u>Page</u>
LIST OF FIGURES	ii
LIST OF TABLES	ix
LIST OF SYMBOLS	x
SECTION I	1
INTRODUCTION	1
SECTION II	2
BACKGROUND	2
A. Physical Metallurgy	2
B. Mechanical Properties	3
SECTION III	5
EXPERIMENTAL PROCEDURE AND RESULTS	5
A. Material, Specimen Fabrication and Heat Treatment	5
B. Test Procedures	6
C. Metallographic Examination	9
SECTION IV	12
DISCUSSION OF EXPERIMENTAL RESULTS	12
A. Characterization of Initial Structures	12
B. Low Cycle Fatigue	13
C. TEM Analysis	23
D. Fatigue Crack Propagation (FCP)	24
E. Corrosion Fatigue	29
SECTION V	32
CONCLUSIONS	32
TABLES	33
FIGURES	38
REFERENCES	105

LIST OF FIGURES

<u>FIGURE NO.</u>	<u>CAPTION</u>	<u>PAGE</u>
1.	Specimen configuration relative to the rolling direction of plate.	38
2.	Tensile test specimen. (Dimensions are in inches)	39
3.	Smooth bar longitudinal strain control LCF specimen. All dimensions are in inches.	40
4.	Single edge notch specimen (SEN), (dimensions are in inches). Thicknesses of 0.08" and 0.25" were used.	41
5.	Standard compact specimen (W = 1 inch). Thicknesses of 0.25" and 0.5" were used.	42
6.	Typical LCF specimen showing multiple initiation as indicated by the arrows.	43
7a.	Cumulative glide behavior of AF 1410 in the annealed condition.	44
7b.	Cumulative glide behavior at AF 1410 aged at 950°F for 5 hrs.	45
8a.	Cyclic stress-strain curve of annealed AF 1410.	46
8b.	Cyclic stress-strain curve for AF 1410 heat treated at 950° for 5 hrs. and air cooled.	47
9a.	Coffin-Manson curve of annealed AF 1410.	48
9b.	Coffin-Manson curve of AF 1410 heat treated at 950° for 5 hrs. air cooled.	49
10a.	Representative hysteresis loops for AF 1410. Aged at 950°F for 5 hrs. The numbers refer to cycles. $\Delta\epsilon_p^L = 0.29\%$.	50
10b.	Representative hysteresis loops for AF 1410. Aged at 950°F for 5 hrs. The numbers refer to cycles and σ_R is the Bauschinger stress. $\Delta\epsilon_p^L = .803\%$.	51
10c.	Representative hysteresis loops for AF 1410 in the annealed condition. The numbers refer to cycles. $\Delta\epsilon_p^L = 0.134\%$.	52
10d.	Representative hysteresis loops for AF 1410 in the annealed condition. The numbers refer to cycles and the Bauschinger stress is denoted σ_R . $\Delta\epsilon_p^L = 0.702\%$.	53

List of Figures (Continued)

<u>FIGURE NO.</u>	<u>CAPTION</u>	<u>PAGE</u>
11.	Fatigue crack growth rate versus stress intensity range for AF 1410 steel aged at 950°F, tested at 10 Hz with $R = 0.1$. SEN specimen, $B = 0.08$ ". Solid line is the data fit in all FCP figures.	54
12.	Fatigue crack growth rate versus stress intensity range for AF 1410 steel, 950°F/5 hrs. age, tested at 10 Hz. and $R = 0.1$.	55
13.	Fatigue crack growth rate versus stress intensity range for AF 1410 steel, 950°F/5 hrs. age, tested at 10 Hz. and $R = 0.1$.	56
14.	Fatigue crack growth rate versus stress intensity range for AF 1410 steel, 950°F/5 hrs. age, tested at 10 Hz. and $R = 0.1$.	57
15.	Fatigue crack growth rate versus stress intensity range for AF 1410 steel aged 5 hrs. at 975°F, tested at $f = 10$ Hz. and $R = 0.1$. SEN specimen, $B = 0.08$ ".	58
16.	Fatigue crack growth rate versus stress intensity range for AF 1410 steel aged 5 hrs. at 750°F, tested at 10 Hz. and $R = 0.1$. SEN specimen, $B = 0.08$ ".	59
17.	Effect of ageing temperature on fatigue crack growth rate of AF 1410 steel. All tests run at 10 Hz. and $R = 0.1$. SEN specimens, $B = 0.08$ ".	60
18.	Effect of thickness on fatigue crack growth rate of AF 1410 steel, 950°F/4 hrs. age, tested at 10 Hz. and $R = 0.1$.	61
19.	Effect of specimen geometry on fatigue crack growth rate of AF 1410 steel, 950°F/5 hrs. age, tested at 10 Hz. and $R = 0.1$.	62
20.	Effect of "R" ratio on fatigue crack growth rate of AF 1410 steel, aged at 950°F for 5 hrs., tested at 10 Hz. SEN specimen, $B = 0.08$ ".	63
21.	FCP curve of AF 1410 steel, 950°F/5 hrs. age, in 3.5% NaCl solution. $R = 0.1$. SEN specimen.	64
22.	FCP curve of AF 1410 steel aged at 950°F for 5 hrs. and tested in 3.5% NaCl solution. $R = 0.1$, SEN specimen.	65

List of Figures (Continued)

<u>FIGURE NO.</u>	<u>CAPTION</u>	<u>PAGE</u>
23.	FCP curve of AF 1410 steel aged at 950°F for 5 hrs., tested in 3.5% NaCl solution. R = 0.1, SEN specimen, B = 0.08".	66
24.	FCP curve of AF 1410 steel aged at 950°F for 5 hrs., tested in 3.5% NaCl solution. R = 0.1, SEN specimen, B = 0.08".	67
25.	FCP curve of AF 1410 steel aged at 950°F for 5 hrs., tested in 3.5% NaCl solution. R = 0.1, SEN specimen, B = 0.08".	68
26.	Comparative fatigue crack growth rates of AF 1410 steel aged at 950°F for 5 hrs. Tested in different environments SEN specimens of 0.08" thickness were used at R = 0.1.	69
27a and b.	Optical photomicrographs of AF 1410 steel. (a) As-quenched (annealed) microstructure. Note the banded structure. (b) 950°F/5 hrs. age microstructure. Grain size is ASTM #16.	70
27c and d.	(c) Microstructure for the 750°F/5 hrs. age. (d) Microstructure for the 975°F/5 hrs. age.	71
28a and b.	Microstructure of AF 1410 steel as obtained by TEM replicas. (a) As-quenched (annealed) micrograph showing the large carbides and plate shaped martensite laths. (b) 950°F/5 hrs. age. Fine (MoCr) ₂ C precipitates are seen.	72
28c and d.	(c) 750°F/5 hrs. age microstructure. Precipitates are larger than the 950°F age. (d) 975°F/5 hrs. age microstructure.	73
29a and b.	(a) Orientation of TEM foils in fractured LCF specimens. (b) Fracture surface for SEM analysis relative to the stress axis in SEN and CT specimens.	74
30.	TEM micrograph of the as-quenched annealed substructure showing the dislocated martensitic structure and needle shaped twins.	75

List of Figures (Continued)

FIGURE NO.	CAPTION	PAGE
31.	TEM micrograph of the 950°F/5 hrs. ageing treatment, obtained using two beam diffracting conditions. Note the highly dislocated lath martensitic structure. Retained austenite is seen around lath boundaries and fine precipitates appear in the lath interiors apparently nucleated on dislocations.	76
32.	Undeformed structure of the 975°F/5 hrs. ageing treatment. Fine precipitates within and at lath boundaries are seen. Retained austenite is also present in lath boundaries.	77
33.	Undeformed structure of the 750°F/5 hrs. ageing treatment. Carbides are much larger than were seen in the 950°F age. Internal twins and plate shaped Fe ₃ C precipitates are also visible.	78
34a and b.	TEM micrographs of 950°F age LCF specimen tested at $\Delta\epsilon_p^L = 0.8\%$ ($N_f = 400$ cycles). (a & b) Dislocations are rearranged into quasi cells as compared to the undeformed structure. No slip bands are seen. Microtwins appear inside martensite laths are seen in (b).	79
34c.	(c) Martensite lath containing extremely high dislocation density.	80
35.	Substructure of 950°F age LCF specimen tested at $\Delta\epsilon_p^L = 0.03\%$ ($N_f = 5000$ cycles). No slip bands are seen and dislocations appear rearranged into quasi cells.	81
36.	TEM micrographs of 750°F age LCF specimen tested at $\Delta\epsilon_p^L = 0.14\%$. Some thin elongated twins are seen inside martensite laths along with plate shaped Fe ₃ C which is always located within laths.	82
37.	TEM micrographs of 975°F age LCF specimen tested at $\Delta\epsilon_p^L = 0.14\%$. Precipitation appears along the lath boundaries in (a). A quasi cell structure appears to be developing in (b).	83
38a and b.	SEM micrographs of the fracture surface of annealed LCF specimens. In (a) the origin of a low strain specimen is shown, while (b) is the overload region of the same specimen. In (c) the origin region of a high strain specimen is shown.	84

List of Figures (Continued)

<u>FIGURE NO.</u>	<u>CAPTION</u>	<u>PAGE</u>
38c.	SEM micrographs of the fracture surface of annealed LCF specimens. In (a) the origin of a low strain specimen is shown, while (b) is the overload region of the same specimen. In (c) the origin region of a high strain specimen is shown.	85
39a and b.	SEM micrographs of the fracture surface of 950°F/5h aged LCF specimens. In (a) and (b) the origin and near-origin regions of a low strain specimen are shown while in (c) and (d) the near origin and overload regions of a high strain specimen are shown.	86
39c and d.	SEM micrographs of the fracture surface of 950°F/5h aged LCF specimens. In (a) and (b) the origin and near-origin regions of a low strain specimen are shown while in (c) and (d) the near origin and overload regions of a high strain specimen are shown.	87
40.	SEM micrograph of LCF specimen aged at 750°F. The photograph was taken in the near-origin region.	88
41.	SEM micrograph of fracture surface of LCF specimen that was aged at 975°F. The photo was taken in the near-origin region.	89
42.	SEM fractographs of 950°F for 5 hr. age FCP specimens. Stress intensity levels are indicated on each fractograph. The arrow marks the crack propagation direction. a & b are for low ΔK levels and exhibit a generally transgranular mode. Extensive branch cracking (marked A) is obvious. Note the dimples in the upper right hand corner of (a) indicative of localized normal rupture.	90
43.	SEM fractographs for 950°F for 5 hr. aged material at intermediate stress intensities. (a) Stereo-pair showing large branch cracks. (b) Small dimples indicating localized normal rupture.	91
44.	SEM fractographs for 950°F for 5 hr. aged material at intermediate stress intensities. (a) Fracture surface is rough and dimpling is more pronounced. This fractograph was taken from a test run in lab air. (b) Striations, marked B are clearly seen. FCP rate computed from these striation spacings is 4.33×10^{-5} inch/cycle as compared to the experimental rate of 3.5×10^{-5} inch/cycle. Tested in dry argon.	92

List of Figures (Continued)

<u>FIGURE NO.</u>	<u>CAPTION</u>	<u>PAGE</u>
45a.	SEM fractographs for 950°F for 5 hr. aged material at intermediate stress intensities. (a) Stereo-pair at a high stress intensity level. Fracture surface is rough and branch cracks are much larger than before. Again cracking is transgranular.	93
45b and c.	(b) Tensile overload region showing large dimples, indicative of normal rupture and brittle striations (marked C). (c) Brittle striations and branch cracks.	94
46a.	SEM fractographs of 750°F for 5 hr. age FCP specimens. Stress intensity levels indicated on the fractographs. (a) Stereo-pair at low stress intensity level. Extensive carbide cleavage is obvious. No striations or branch cracking is seen.	95
46b.	(b) Stereo-pair at slightly higher ΔK .	96
47a.	SEM fractograph of material aged at 750°F for 5 hr. and tested at intermediate ΔK levels. In (a) extensive cleavage of carbides is seen along with some fine dimples.	97
47b.	(b) Stereo-pair, showing extensive branch cracks and dimples. No striations were seen in the FCP specimens for this treatment.	98
48a and b.	SEM fractographs of 975°F for 5 hr. age FCP specimens. Stress intensity levels are indicated on each fractograph. Arrows indicate the crack propagation direction. In (a) and (b) branch cracking and a few areas of carbide cleavage are visible. Cracking appears to be transgranular.	99
48c.	(c) Stereo-pair showing rough fracture surface and extensive branch cracking.	100
49.	Cycles to failure vs. plastic work/cycle for AF 1410 in the annealed condition.	101
50.	Cycles to failure vs. plastic work/cycle for AF 1410 aged at 950°F for 5 hrs.	102
51.	Comparison of fatigue crack growth behavior of AF 1410 steel with D6Ac, HY 180 and 300 maraging steel. Data for these materials, except AF 1410 steel, obtained from ref. 28.	103

List of Figures (Continued)

<u>FIGURE NO.</u>	<u>CAPTION</u>	<u>PAGE</u>
52.	Plot of $\ln \left(\frac{da}{dt} \right)_{cf}$ versus $\frac{1}{T}$ (K^{-1}) at indicated stress intensity levels.	104
53.	Plot of Q versus $\frac{\Delta K^2}{E}$ to obtain the characteristic activation energy. ($E = 29 \times 10^3$ ksi)	105

LIST OF TABLES

<u>TABLE NO.</u>	<u>CAPTION</u>	<u>PAGE</u>
1.	Composition of AF-1410 Steel (Wt.%)	33
2.	Mechanical Properties of AF-1410 Aged for 5 Hrs. at 950°F.	34
3.	LCF Test Results	35
4.	Paris Equation Constants	36
5.	Summary of LCF Parameters Used to Predict Coffin-Manson Exponent	37

LIST OF SYMBOLS

K_{ISCC}	threshold stress intensity level in stress corrosion
R_c	hardness, Rockwell C scale
$\frac{da}{dn}$	crack growth/cycle
R	rate constant in the Paris equation
m	exponent in the Paris equation
ΔK	cyclic stress intensity range
$\frac{da}{dt}$	crack extension rate
A	constant
Q_{cf}	activation energy for corrosion fatigue
Q_o	apparent activation energy
α	constant
E	modulus of elasticity
K_c	critical stress intensity parameter
ΔK_o	threshold stress intensity
ϵ_f	monotonic fracture strain
σ_{ys}	yield strength
B	Coffin-Manson exponent
l	process zone size
s	constant
R_p^f	fatigue plastic zone size
$\Delta \epsilon_p^l$	longitudinal plastic strain range
N_f	number of cycles to failure
μ	micron
MPa	Mega Pascals (units of stress)

SECTION I

INTRODUCTION

Recently a program has been completed under Air Force sponsorship that has resulted in the development of a high strength steel (yield strength in the range of 210-230 ksi) with good fracture toughness (at least 115 ksi√in.) and good resistance to stress corrosion cracking ($K_{ISCC} > 100 \text{ ksi}\sqrt{\text{in.}}$). This steel was developed using the existing HY-180 as a basis. The composition was statistically varied and an alloy having the composition and properties shown in Tables 1 and 2 was the result. The material is a strong candidate to replace other steels and in some cases titanium in advanced air frame structures.

While AF14-10 is very attractive for air frame applications, additional information is required before it can be confidently used in critical components. In many air frame applications fatigue crack propagation (FCP), corrosion fatigue (CF), and to a lesser extent low cycle fatigue (LCF) are critical properties that must be characterized and understood. The object of this investigation was then to examine FCP and CF properties in depth along with some LCF studies.

SECTION II

BACKGROUND

In this section a very brief review of the physical and mechanically metallurgy of AF14-10 steel is given.

A. Physical Metallurgy

a. As-Quenched Structure

The structure is macroscopically banded with Ni and Mo variations apparently accounting for this (1,2).

The grain size is very fine (ASTM #16) and the martensite has a lath morphology that is highly dislocated. Because of a rather high M_s temperature, auto-tempering tends to take place (Fe_3C carbides form). The dislocation substructure is quite stable as high as 1100°F and this stability has been attributed to the high cobalt content of AF14-10 steel (3).

b. Ageing

Ageing is normally carried out at 950°F for 5 hours to produce peak hardness. Strengthening is a result of the formation of $(MoCr)_2C$ precipitates and along with the precipitation of carbides, austenite (approximately 3%) also forms in the lath boundaries and is retained at room temperature (3). From room temperature to 800°F strengthening occurs primarily by the formation of Fe_3C carbides. These carbides lie on {110} martensite planes and have a Widmanstatten structure. From 800-1000°F strengthening occurs, as was previously mentioned, by the formation of $(MoCr)_2C$.

c. Transformation Temperatures

The transformation temperatures have been measured dilatometrically as a function of heating and cooling rate ⁽ⁱ⁾ The M_s temperature is relatively insensitive to cooling rate and is approximately 610°F with an M_f in the range of 200-212°F. The martensite→austenite transformation, on the other hand, is dependent upon the heating rate. The A_s and A_f temperatures for high heating rates (i.e. 400°F per second) are 1405 and 1517°F, respectively, and transformation occurs by a reverse shear mechanism. At low heating rates (i.e. 0.2-1.1°F per second) the A_s transformation temperature is lower and heating rate dependent.

B. Mechanical Properties

In general, those properties most studied have been yield strength, ultimate tensile strength, and fracture toughness ⁽¹⁾ and typical mechanical properties are shown in Table 2. It has been found that the toughness/strength relationship is optimized by the 950°F/5 hour ageing cycle. The increasing strength and toughness when the material is aged in the temperature range of 800-900°F has been attributed to secondary hardening ^(1, 2) (i.e. replacement of coarse Fe_3C with a fine dispersion of $(MoCr)_2$ particles that nucleate preferentially on dislocations). Above 900°F over-ageing and austenite reversion occur and there is a great increase in toughness (approximately a factor of 5 as measured by CVN) with a small reduction in strength (approximately 10%). It would thus appear that to a large extent the excellent fracture toughness properties can be attributed to

the presence of retained austenite. For example, it has been shown that for many steels austenite undergoes a strain-induced phase transformation to martensite (4-6). The author of this report has shown theoretically (5, 7) and experimentally (5, 8) that the strain induced austenite to martensite transformation is an extremely efficient toughening mechanism. Another possibility is that the energy dissipation associated with plastically deforming the austenite contributes very significantly to the toughness (6). These ideas are strengthened by the results of a weld simulation study (1) in which various combinations of peak temperature, energy input, number of passes, and heat treatment sequence (i.e. pre-weld, post-weld age) were investigated. It was found that the retained austenite was present in fairly significant amounts. In simulated studies of one pass to peak temperature, the toughness was higher than the non-cycled and aged specimens provided that the peak temperature was below A_f . The very large toughness increases were attributed to the formation of retained austenite although the exact mechanism was not delineated. These observations are consistent with what the author has observed in a 300 grade maraging steel in a program under AFOSR sponsorship (9). When multiple weld pass cycles were simulated, qualitatively similar results were obtained except in some cases the toughness was higher even when the peak temperature exceeded A_f .

SECTION III

EXPERIMENTAL PROCEDURE AND RESULTS

A. Material, Specimen Fabrication and Heat Treatment

1. Composition and Processing

The chemical composition of this material is listed in Table 1

Slabs of 6 3/4" x 12" x 22" were heated to 2150°F and rolled parallel to the ingot axis to obtain 2" thick plates. These plates were then cross rolled (normal to ingot axis) to 0.625" thickness. All plates were water quenched immediately after rolling.

Four plates of 0.625" x 12.5" x 21", weighing about 165 lbs. each, were received in the rolled and annealed condition from N. A. Rockwell. These plates had been double austenitized at 1650°F and 1500°F (1 hour/inch) water quenched at each interim.

2. Specimen Fabrication

Specimens for tensile LCF, FCP testing were machined from as-received plate as shown in Fig. 1. Drawings for each specimen type are shown in Figs. 2 - 5.

3. Heat Treatments

a) 950°F Age.

This consisted of ageing the specimen for five hours in a laboratory box furnace whose setting was so adjusted that the thermocouple attached to the specimen read 950°F. After ageing, the specimens were air cooled.

b) 975°F Age and 750°F Age.

Ageing was the same as the 950°F age except for the temperature differences. These two ages were selected because the material at these temperatures has the same strength (~ 215 ksi) but different structures ⁽¹⁾. At 750°F, Fe_3C carbide was mostly observed, while at 975°F, $(\text{Mo}, \text{Cr})_2\text{C}$ predominates.

B. Test Procedures

1. Mechanical Test Procedures

Tensile tests using standard ASTM recommended specimens, Fig. 2., were performed using an MTS system in the stroke control mode. The outputs from the load cell and the clip-on gage mounted directly on the specimen were plotted on the y and x axis, respectively of an x-y recorder. Thus, an engineering stress-strain diagram was obtained which characterized the various tensile properties shown in Table 2.

2. Low Cycle Fatigue (LCF)

LCF tests were conducted on smooth bar longitudinal specimens of the type shown in Fig. 3. The specimens were finished by low stress grinding to eliminate residual stresses and testing was carried out using an MTS machine in longitudinal strain control. The strain was varied linearly with an R ratio of 0.05 (i.e. zero+tension+zero) and the frequency was maintained at 0.2 Hz. An extensometer with knife edges spanning the gauge length of the specimen magnified the longitudinal displacement by a factor of 2. The displacement was

measured using an MTS clip-on gage whose output was used as the control signal. The plastic strain range was maintained approximately constant during a test by manually adjusting the total strain range whenever necessary. Hysteresis loops were recorded throughout the entire test and number of cycles to failure noted.

The LCF test results are summarized in Table 3. Multiple initiation sites were identified on all samples which is an indication of excellent alignment (Fig. 6).

The LCF data was utilized to form cumulative glide plots, Fig. 7, cyclic stress-strain curves, Fig. 8, and Coffin-Manson plots, Figs. 9. Typical hysteresis loops are shown in Fig. 10.

3. Fatigue Crack Propagation

Single edge notch (SEN) and Compact Tension (CT) specimens were machined to the dimensions shown in Figs. 4 & 5. The thickness of the SEN specimens was 0.08" and for the compact tension specimens, two thicknesses, 0.25" and 0.5" were used. The faces of the heat-treated specimens were polished to 600 grit and subsequently pre-cracked using a 50 kip MTS machine. Tests were run in the load control mode usually at an R ratio of 0.1 and a frequency of 10 Hz. In some cases the R ratio was varied to study this effect.

The rate of FCP was measured using Micromeasurement Type CPA - 02 crack propagation gages glued directly to the specimen. The fine wires on the gage were 0.02" apart and

break when the crack front reaches them, causing a change in the electrical resistance of an electric circuit. To provide an inert atmosphere, 99.996% pure argon containing 10 ppm moisture, dried further by passing through a U-tube containing drierite (anhydrous CaSO_4) was used. The Ar was fed into a plastic bag wrapped around the specimen and a positive Ar pressure was maintained in this way. The FCP data is plotted in Figs. 11-20. The data has been fit to the inverse hyperbolic (10) tangent model. A list of the Paris law constants is given in Table 4.

4. Corrosion Fatigue

SEN specimens 0.08" thick were tested at 0.4Hz and 0.08" and 0.25" thick specimens were tested at 10 Hz. The higher frequency tests were run on 50 kip MTS closed loop hydraulic system while the low frequency tests were run on a 20 kip Instron Universal Testing machine. Both these machines were run in load control mode.

All testing was carried out in a 3 1/2% NaCl solution. A large volume of corrosive solution to sample surface area was maintained by using a large acrylic chamber holding about three gallons. The system was recirculating, pH controlled and filtered. The grips were coated with an epoxy coating to minimize crevice and galvanic corrosion. The loading pin holes were lined with Teflon inserts to prevent the specimen from being galvanically coupled to the

grips. Constant temperature was maintained by a Tempstir immersion heater/propeller device. The corrosion fatigue test results are shown in Figs. 21-26.

C. Metallographic Examination

1. Light Microscopy of Initial Structures

For light microscopy, the samples were mounted in Bakelite, hand lapped through 600 grit SiC and polished on a 0.05 μ diamond wheel. A modified tint etchant was used for etching.

Etching was carried out as follows:

- 1) 25 ml. HNO_3 / 75 ml methyl alcohol
- 2) 1% Picric Acid / 5% HCl in methyl alcohol
- 3) 30 gm $\text{Na}_2\text{S}_2\text{O}_5$ / dist H_2O

Optical photomicrographs for the annealed, 950°F, 975°F and the 750°F age are shown in Fig. 27.

2. Transmission Electron Replica Microscopy

A standard two stage plastic replica technique was used to characterize the microstructure at higher magnifications. Replicas were made using cellulose acetate tape, carbon backing and shadowing with germanium. The plastic was dissolved in acetone and the replica was mounted on a Cu screen for subsequent Transmission Electron Microscopy. Typical micrographs are shown in Fig. 28.

3. Thin Foil Transmission Electron Microscopy (TEM)

Very small regions at extremely high magnifications were studied by TEM. A JEOL 200-A microscope was available for this

study which has a specimen holder that can accommodate foils 1/8" in diameter. Cylindrical rods of 1/8" diameter were machined from LCF specimens and thin wafers were cut from near the fracture surface and undeformed button heat regions as shown schematically in Fig. 29. A Bronwill thin sectioning machine was used to cut wafers 0.01" thick. These were then ground on 600 grit paper to a thickness of approximately 0.006" and finally electrothinned using a Fischione Unit. A 90% acetic acid--10% perchloric acid solution with a current density of 2.8 A/cm² (voltage setting 45V) was used.

In order to identify microstructural features, dislocation morphologies and precipitate/dislocation interactions, pictures at magnifications of 15K to 60K were taken, mostly in bright field mode.

The magnetic nature of the material deflects the electron beam off the optical axis, leading to various astigmatic effects (11). Even a small tilt deflects the beam considerably off the center. To overcome these difficulties, a high precision dark field beam deflector was used to re-center the beam as it shifted during tilting. Numerous laths in the structure were scanned until one was found in which a single Bragg reflection was operating. In this way, the clarity of the image could be greatly improved compared to what is usually seen for steels. The deflector capacity limited the extent of tilting to 10°

Similarly, the diffraction spots used for dark field imaging were brought to the optic axis rather than shifting the objective aperture to the spot. Using this technique good quality dark-field pictures could be obtained. TEM micrographs of the various conditions are shown in Figs. 30-37.

4. Scanning Electron Microscopy (SEM)

Detailed fractography was performed on the fracture surfaces of FCP and LCF specimens. A specimen containing the fracture surface and small enough to fit in the Cambridge 600 Stereo Scan Scanning Electron Microscope was cut. After ultrasonically cleaning in acetone, it was pasted to a specimen holder using a silver paint to provide electrical continuity. A 25 kV electron beam was used to scan the fracture surface. Photomicrographs with stereo pairs, wherever needed, were taken at magnifications of 20x to 2K to bring out the fracture characteristics.

FCP specimens were observed at different known locations and thus at known ΔK levels. Fractographs for both LCF and FCP are shown in Figs. 38-48.

SECTION IV

DISCUSSION OF EXPERIMENTAL RESULTS

A. Characterization of Initial Structures

The material composition is given in Table 1. Optical photomicrographs of the four conditions namely, the annealed condition, the 950°F age, the 975°F age and the 750°F age are shown in Fig. 27. Similarly, Fig. 28 shows the replicas observed by TEM.

In the annealed condition, Fig. 27a, bands of dark and light areas are clearly visible. In an electron microprobe analysis carried out by Snide⁽¹⁾, Ni and Mo appeared to be higher in the light etching areas. Little and Machmeier⁽³⁾ suggested that increased Ni lowers the M_s temperature enough to partially retard auto tempering that occurs at higher M_s temperatures. This results in the light/dark etching contrast. Fig. 28a is a TEM replica and the lath martensite is much more clearly visible. A TEM micrograph, Fig. 30, shows the highly dislocated martensitic structure of the annealed material. The carbides have been identified as Fe_3C ⁽¹⁾.

The optical microstructure of the material aged at 950°F is shown in Fig. 27b., while Fig. 28b shows the fine martensitic structure obtained from the TEM replica and the substructure is shown by TEM in Fig. 31. To obtain good diffraction conditions, two-beam conditions were utilized for imaging. The strain contrast tends to obscure the dislocation density but it is obvious that the dislocation density is quite high.

At the 950°F age, fine $(MoCr)_2C$ precipitates are formed and peak hardness is achieved. As discussed in a later section, this ageing treatment gave optimum properties for this material.

There was not any appreciable difference between structures of the 950°F age and the 975°F age, as can be seen from Figs. 27d, 28d and Fig. 32.

For the 750°F ageing treatment, it is clearly visible from Figs. 27c and 28c that the precipitates are coarser than in the 950°F age and tend to occur in lath boundaries. Some twinning is also present, Fig. 33. The presence of austenite in the interlath boundaries was also observed.

B. Low Cycle Fatigue

1. Annealed Structure

a. Analysis of Mechanical Test Results

Cyclic softening, as represented by a decrease in the height of the hysteresis loop occurs from the very first cycle. This is illustrated in Fig. 7, which is a plot of stress amplitude (obtained from the height of hysteresis loops) versus the number of cycles. This type of plot is characteristic of materials with high dislocation densities. The effect of cycling is to re-order the high initial dislocation density that is implanted by the austenite→martensite transformation. This behavior is observed for cold worked solid solutions⁽¹²⁾ and most steels⁽¹³⁾.

It is possible to evaluate the Baushinger effect in terms of σ_R , the stress at which reverse plastic flow is first observed, indicated as the first detectable departure from elasticity (linearity). A smaller σ_R implies a larger Baushinger effect. The Baushinger effect in this case, as indicated in Fig. 10b, is rather large which is indicative of a high dislocation density.

The longitudinal plastic strain range $\Delta \epsilon_p^L$ was plotted against the cycles to failure N_f , on a log-log basis to form a Coffin-Manson curve. The plot is shown in Fig. 9. It is important to note that a least-square analysis of data gave a best fit when two log-linear segments were considered. Such a break has been taken to imply a change in the deformation mode of the material⁽¹⁴⁻¹⁶⁾. Both segments were extrapolated to one quarter cycle where the plastic strain range corresponds to the fatigue ductility. It is interesting to note that the fatigue and tensile ductility are very different for the low strain regime, while in the high strain region there is better agreement.

The cyclic stress strain curve is represented in Fig. 8. The cyclic stress-strain behavior of a material is very useful when saturation occurs for a given applied plastic strain range. However in materials like AF 1410 where cyclic softening is observed, there is no unique cyclic stress-strain curve. For this study an average stress range at the mid-life was chosen for each test to represent a cyclic stress strain curve.

Various investigators have suggested energy as a LCF failure criterion. For example, Morrow related the number of cycles to failure N_f to the energy absorbed per cycle ΔW by the equation⁽¹⁷⁾:

$$N_f \Delta W = c \quad . . . (1)$$

where c = damage constant.

ΔW = the energy absorbed/cycle/unit volume of material
and is computed from the area enclosed by the
hysteresis loop.

This was later modified by Antolovich and Saxena⁽¹⁸⁾ to:

$$N_f (\Delta W)^\alpha = c' \quad . . . (2)$$

where c' = material constant

α = material constant, demonstrated to depend on slip
characters in Cu-Al alloys⁽¹⁸⁾

They demonstrated that ΔW can be approximated by the equation⁽¹⁸⁾:

$$\Delta W = \frac{\Delta \epsilon_p \Delta \sigma_m}{(n' + 1)} \quad . . . (3)$$

where n' is the cyclic strain hardening exponent.

Because considerable loop energy change was observed over the
length of a test, an average value of ΔW was obtained by
integrating the loop energy over the length of a test, and
dividing it by the number of cycles to failure. Figure 49
is a typical plot of ΔW against N_f on log-log basis; the
slope of the line gives α . Again, a change in the slope α ,
is observed.

Morrow's energy approach⁽¹⁷⁾ predicts the Coffin-Manson exponent
is given by the following equation:

$$\beta = \frac{1}{1 + 5n'} \quad . . . (4)$$

Tomkins⁽¹⁹⁾ considered crack growth to be decohesion across two slip planes, and obtained the following result:

$$\beta = \frac{1}{1 + 2n'} \quad . . . (5)$$

The derivation of this equation is questionable on theoretical grounds since the remote stress range in a cracked specimen was converted into plastic strain range using the cyclic stress strain curve, thus implying that the remote stresses are high enough to be in the plastic region. However, Tomkins also used the well-known Dugdale-Muskhelishvili plastic zone model⁽²⁰⁾ which presupposes that the remote stresses are elastic.

As already noted, Antolovich and Saxena⁽¹⁸⁾ modified the energy approach to take into account the fact that as the slip mode changes the fraction of the total plastic work stored as fatigue damage would be expected to change. This was expressed mathematically in equation 2. This approach thus predicts:

$$\beta = \frac{1}{\alpha(1 + n')} \quad . . . (6)$$

which has been demonstrated to effectively incorporate slip mode changes in Cu-Al alloys introduced by varying the Al content. Using the above equation yields good agreement with experimental AF 1410 observations as is seen in Table 5.

b. SEM Analysis of Annealed Structure

Typical SEM micrographs are shown in Fig. 38. In Fig. 38 fatigue features such as rough corrugations, branch cracks and faint striations (lower left) can be seen. In addition, numerous

dimples associated with impurity core are also visible. These features were observed near the fracture origin of a low strain specimen and are quite typical of many steels. A highly dimpled appearance is seen in Fig. 38b, which was taken from the overload region of the same specimen, which is typical of a ductile steel.

The features associated with high strain fatigue are shown in Fig. 38c. Note the secondary cracks and the more numerous density of tensile features compared to 38a, which indicates that tensile deformation processes are playing an increasingly important role.

2. Material Aged at 950°F

a. Analysis of Test Results

The cyclic softening characteristic of this treatment is shown in Fig. 7. The rate of cyclic softening differs from that in the annealed condition. In the 950° age condition, softening occurs very gradually until the later stages of life. This behavior is characteristic of a material undergoing particle shearing⁽¹³⁾. In evaluating the Bauchinger effect of the material in the 950° age condition, more evidence of particle shearing is uncovered. The Bauchinger effect is large, but the incremental effect is small compared to the annealed condition. This observation is compatible with a shearing deformation mode.

In analyzing the Coffin-Manson plot, no break was observed in the 950° age condition, in contrast to the break found in this material in the annealed condition. A large value of β and a high extrapolated fatigue ductility, Fig. 9, were other traits common to the 950° aged treatment. The large Coffin-Manson exponent would ordinarily render the tests suspect. However the value shown in Table 5 was obtained from numerous tests. Also, there were multiple initiation sites as seen in Fig. 6. Additional theoretical justification is given in the following section. An energy analysis of the material in this condition was carried out and ΔW vs N_f is shown in Fig. 50. The slope α was used to compute the Coffin-Manson exponent as indicated in equation 6 and the calculated results are in good agreement with the experiment as shown in Table 5.

b. SEM Analysis of Material Aged at 950°F

SEM micrographs of the fracture surfaces of LCF test specimens are shown in Fig. 39. In Figs. 39a and 39b the initiation and near initiation regions are shown for a low strain specimen. Note the cracked intermetallic in (a). In (b) the features have been obscured by rubbing but faint striations (upper center) and branch cracks can be seen.

Typical features of a high strain specimen are shown in Figs. 39c and 39d. In Fig. 39c extensive branch cracking has occurred in the near-origin region, while in (d), taken from the overload region, ductile dimples along with a hint of intergranular fracture can be seen.

c. TEM Analysis of LCF Specimens - 950°F Age

Transmission electron microscopy was done on foils prepared from the longitudinal LCF specimens. It was necessary to use LCF specimens because of the extremely small fatigue plastic zones ahead of the main crack tips and it was quite difficult to obtain a thin foil within that region from the FCP specimens. To simulate FCP substructures at high and low ΔK levels, LCF specimens at high and low plastic strains were used. Antolovich and Saxena have previously demonstrated the validity of this approach⁽¹⁸⁾.

The initial structure of the AF-1410 steel aged at 950°F consists of a highly dislocated lath martensite, Fig. 31. A small amount of stringer like retained austenite is present at interlath boundaries. Machmeier et. al.⁽³⁾ have also reported the formation of retained austenite at interlath boundaries in a 10Ni-Co-Cr-Mo-C alloy. Precipitate particles, which are very fine, are located in the interior of the lath and the lath boundaries. These particles could not be resolved due to their small size but have been identified as fine $(\text{MoCr})_2\text{C}$ by Speich et al.⁽²⁾. These small size finely dispersed particles seem to nucleate at dislocations.

The LCF results along with TEM observations can frequently be used to shed light on precipitate-dislocation interactions. It was difficult, however, to determine whether precipitates were cut or looped by dislocations since the precipitate size is very small. Consequently indirect methods must be used. For

example, Van Swam et al.⁽²¹⁾ in a study of fatigue in 300 grade maraging steel observed a large Baushinger effect from which they conclude that the particles are looped by dislocations and the cyclic softening results from a rearrangement of network of "geometrically necessary" dislocations formed around each precipitate. However this explanation does not take into account the large Baushinger effect due to the high dislocation density which is developed during the austenite→martensitic phase transformation⁽¹³⁾. Considering the closeness of the precipitates and their small size, with a high dislocation density in the matrix, bypassing seems a very unlikely mechanism. At higher strains, the cyclic softening can be explained if successive degeneration of precipitates is considered when dislocations cut through them. This approach has been used satisfactorily to explain cyclic softening in many other precipitate strengthened systems⁽²²⁻²⁵⁾. Based on this, it can be hypothesized that in the AF-1410 steel, particle shearing is probable. This, however, could not be substantiated directly by TEM analysis. Figure 34 shows high strain ($\Delta\epsilon_p^L = 0.8\%$, $N_f = 400$ cycles) TEM micrographs of deformed structures. There appears to be a tendency toward some fine cell formation and wavy dislocations were observed. No slip bands were seen at high strain. However, a small amount of twinning was seen at high strain. At low strain ($\Delta\epsilon_p^L = 0.03\%$, $N_f = 5000$ cycles) deformation seems to be more homogeneous and again no slip bands were observed, Fig. 35.

Saxena and Antolovich⁽¹⁸⁾ have shown that a break in the

slope of the Coffin-Manson plot is associated with a change in slip mode. For the LCF tests, no change in β was observed and it appears as if slip mode changes do not occur in the 950°F ageing treatment for this alloy. This is consistent with the TEM observations in which only wavy slip was seen.

3. 750° and 975° Age

a. Mechanical Test Results

A limited amount of LCF work was conducted on this material in the 750° age and 975° age conditions in order to evaluate microstructural effects and to provide a comparison to the material in 950°F age and annealed condition. Of the four treatments, the LCF life was found to be best at 750°F, and there was no essential difference in the fatigue life at 950° and 975°. This is shown in the Coffin-Manson curves in Fig. 10.

b. SEM Analysis of Materials Aged at 750°F and 975°F

(i) 750°F Age

The LCF appearance is shown in Fig. 40 in the near origin region. In this region there are areas that are apparently crystallographic in nature and which have either been rubbed during the fatigue process or which show evidence of fine slip. In view of the roughness of the surface in other areas the first explanation appears to be most probable.

(ii) 975°F Age

The features were similar to those seen for the 950°F aged specimens. Branch cracks and dimples can be seen in Fig. 41, taken from the near-origin region of a LCF specimen.

C. TEM Analysis

(i) 750°F Age

A very limited amount of LCF testing was done for the 750°F ageing treatment in order to study the effects of microstructure on deformation mechanisms. Figure 33 shows the initial microstructure for the 750°F age. The Lath martensite was highly dislocated and some internal twinning was also seen. Plate shaped Fe_3C was clearly visible and was always located within the martensite laths. Some thin elongated twins were present in the laths.

For the LCF tests run at a plastic strain range of 0.14%, Fig. 36 again shows a small number of thin elongated twins. No slip bands were observed. However, the dislocations were rearranged as compared to the untested condition. There appears to be a tendency to form very fine cells.

(ii) 975°F Age

The initial substructure of this alloy aged at 975°F is shown in Fig. 32. The structure is similar to the 950°F age except that the $(\text{MoCr})_2\text{C}$ carbides are coarser. The lath structure is again highly dislocated and plate-like. No twinning was observed. One noticeable difference, however, was the presence of a few thin plate shaped particles, similar to those observed in the 750°F age. These particles could not be identified.

As for the 750°F age, limited testing was conducted. The TEM micrograph in Fig. 37 was taken from a specimen tested at a plastic strain range of 0.14%. Cells were formed and the

initial highly dislocated substructure has given way to a rearranged substructure. No slip bands or twins were observed.

D. Fatigue Crack Propagation (FCP)

1. Analysis of Test Results

FCP results are plotted on a log-log basis in Figs. 11-20. Three ageing treatments, 950°F/5 hr. age, 975°F/5 hr. age and 750°F/5 hr. age, were investigated to evaluate the effect of different microstructures at the same strength levels. Fig. 17 summarizes the effect of ageing temperatures on FCP rates and it is obvious from this figure that microstructure has a definite effect on FCP rates in this alloy. Figs. 18 and 19 show the thickness and geometry effects, respectively, in dry argon. A slightly higher growth rate was observed for the CT specimen but there was no thickness effect. The mean stress effect, as shown in Fig. 20, was small.

The effect of environment, (i.e. lab air or dry air) was small at least at high test frequencies. This will be discussed more fully in the next section.

An Inverse Hyperbolic Tangent function, ARCTANH, developed by Rockwell International⁽¹⁰⁾ was used to fit the experimental data over the entire range. This function is based on the sigmoidal relationship between applied cyclic stress intensity and crack growth rates and takes into account all the three regions of an FCP curve. Mathematically, it is expressed as:

$$\frac{da}{dn} = C_1 \exp C_2 \tanh^{-1} \frac{\ln \left(\frac{\Delta K^2}{(1-R)K_c \Delta K_0} \right)}{\ln \left(\frac{(1-R)K_c}{\Delta K_0} \right)} \quad \dots (7)$$

where

$\frac{da}{dn}$ = crack growth/cycle

K = cyclic stress intensity range

R = load ratio = $\frac{\text{min. load}}{\text{max. load}}$

K_c = critical stress intensity parameter

ΔK_0 = threshold stress intensity

$C_1 = \ln \left(\frac{K_c}{\Delta K_0} \right)^{m/2}$

$C_2 = C_1 (K_c \Delta K_0)^{m/2}$

where "m" is the slope in the Paris equation.

Paris equation constants "R" and "m" were obtained by a least squares analysis and are listed in Table 4.

It was observed that the crack growth rate for the 750°F age was higher than for the 950°F and the 975°F age. There was no difference, however, in the 970°F and the 975°F ageing treatments. This could be attributed to coarser Fe_3C present at the 750°F age (Fig. 33). Predominant presence of this interlath carbide Fe_3C has also been reported by Das and Thomas⁽²⁶⁾ in an Fe-9Ni-4Co-0.4C steel. In another study⁽²⁷⁾, interlath carbides have been reported to cause a substantial decrease in toughness in Fe-Cr-C steels. The stress-

strain behavior in the AF-1410 steel shows decreased strain hardening with coarsening of alloy carbides⁽³⁾. The same study also shows that the same trend occurs with changes in ageing temperature. Another reason for this behavior appears to be the presence of retained austenite (about 3%) at the 950°F age providing greater ductility to the otherwise brittle martensite matrix.

An analytical approach taken by Saxena and Antolovich⁽¹⁸⁾ considers the existence of a small process zone ahead of the crack tip, where damage is accumulated as in LCF. By applying the Coffin-Manson law to this zone they predict the fatigue crack growth rate as:

$$\frac{da}{dn} = 4 \left\{ \frac{0.7\alpha}{E\sigma_{ys}(1+s)} \epsilon_f \right\}^{1/\beta} \frac{1}{l^{1/\beta-1}} (\Delta K)^{\frac{2+s}{\beta}} \dots (8)$$

where

α = a constant $\approx \frac{1}{24\pi}$

ϵ_f = monotonic fracture strain

E = Young's modulus

σ_{ys} = yield strength

β = Coffin-Manson exponent

ΔK = applied stress intensity range

l = process zone size

s = small constant (depending on crack sharpness)

Knowing R and assuming s to be zero, the process zone size was calculated and m , the Paris equation exponent, was approximated by $2/\beta$. The process zone size calculated by using this approach is $28.3 A^0$. This shows that the process zone ahead of the main

crack tip is extremely small and this could be due to the fact that the fatigue process is controlled by the finely spaced precipitates.

Barsom et al.⁽²⁸⁾ working with HY 80, HY 180, 10Ni-Cr-Mo-Co and 12Ni-5Cr-3Mo steels obtained an empirical equation for the crack growth rate;

$$\frac{da}{dn} = 0.66 \times 10^{-8} (\Delta K)^{2.25} \quad \dots (9)$$

They showed that this equation fits the FCP rates of 19 other high strength steels. A comparison of the FCP rates of AF-1410 steel with HY 180, 300 Maraging steel and D6Ac is shown in Fig. 51.

2. Fractography

(a) 950°F Age

At lower stress intensity levels, the fracture surface of the 950°F age samples exhibited a generally transgranular mode (Fig. 42a & 42b) indicating mode I failure. Some branch cracking is obvious in Fig. 42a. Significant cracking is observed around second phase particles and it could not be determined whether cracks nucleate at these particles or the main crack front deviates to these particles.

The fracture mode at intermediate ΔK levels, (Fig. 43a) again was transgranular propagation and branch cracking is quite evident, as before. Some dimple formation as seen in Fig. 43b, would indicate normal rupture which presumably initiated at precipitates and inclusions.

The FCP rate is the same in lab air and dry argon at a ΔK of about 70 ksi/in, (Fig. 26). This would mean similar fracture mechanisms should occur at this ΔK level and this in fact was observed.

Similarities could be observed in Figs. 44a and 44b, where there are some regions of striation formation and a tendency for dimpling is visible. The FCP rate measured from these striation spacings (Fig. 44b) gives a rate of 4.33×10^{-5} in/cycle as compared to the experimental rate of 3.5×10^{-5} in/cycle.

In the higher ΔK regimes of about 90 to 110 ksi/in, the fracture surface is very rough, Figs. 45a, 45b and 45c. In the tensile overload region of Fig. 45b, large areas of ductile dimples, indicative of normal rupture, along with brittle striations were seen. A stereo-pair at a $\Delta K=90$ ksi/in Fig. 45a shows extensive branch cracking and transgranular cracking. Fig. 45c shows some extremely brittle striations and a very rough fracture surface which is characteristic of this regime in this material. Again the FCP rate calculated from striation spacings in Fig. 45b gives a rate of 5.2×10^{-5} in/cycle as compared to the experimental rate of 4.8×10^{-5} in/cycle.

Overall, the fracture surface of the 950°F age has a ductile appearance in many areas, and as discussed earlier, shows lower growth rates. Retained austenite, being a ductile phase, would obstruct crack propagation.

(b) 750°F Age

In this treatment the fracture features are evidently very different from the 950°F age, as can be seen in Figs. 46-48. At low stress intensity levels Fig. 46, extensive carbide cleavage occurs. Snide⁽¹⁾ identified these cuboidal carbides as Ti(C,N) in Charpy V-notch slow bend tests. The feathery cleavage-like areas in the matrix could be attributed to cleavage in the matrix

and the reason for higher crack growth rates at this ΔK level, compared to the 950°F ageing treatment, could be due to this cleavage phenomenon occurring because of the presence of coarse Fe_3C particles. No branch cracking or striations were seen.

At higher ΔK , branch cracks are visible, Figs. 47a and 47b, and small particles on the fracture surface indicate a tensile type failure. In Fig. 47b which is at a stress intensity range of about 60 ksi/in, fracture features were similar to the 950°F age and this was expected since the crack growth rates of these two ageing treatments were comparable. No striations were, however, visible. Figure 47b, which is a stereo-pair shows extensive branch cracking and dimples.

(c) 975°F Age

The FCP behavior of both the 975°F and the 950°F age was the same and it was expected that similar fracture mechanisms are operating. This was observed and the similarities are quite evident as seen in Fig. 48. Similar features, i.e. branch cracking, transgranular fracture and a rough surface at higher ΔK s were observed for both the heat treatments.

E. Corrosion Fatigue

Fatigue crack growth rates ($\frac{da}{dn}$) versus stress intensity range (ΔK) for the corrosion fatigue tests run in 3.5% NaCl solution are plotted on a log-log basis in Figs. 21-25. These tests were run at frequencies of 0.4 Hz and 10 Hz and at three different solution temperatures of 74, 110 and 150°F. Figs. 21 and 22 are plots for higher frequency (10 Hz) at two different thicknesses of 0.08" and 0.25".

A comparison of this data shows that there is no thickness effect at this frequency. Figs. 23, 24 and 25 give results of tests run at 0.4 Hz at different temperatures. All the specimens were 0.08" thick. The FCP rate was generally higher at the higher temperature. The effect of environment and frequency is summarized in Fig. 26. It can be seen that for a given frequency the FCP rate increases with increasing severity of the environment (i.e. dry Ar, lab. air, 3 1/2% NaCl. Also as the frequency is reduced to .4Hz in 3 1/2% NaCl, the FCP rate is greatest and the relative change increases with decreasing stress intensity. This is characteristic of a classic corrosion fatigue process.

Antolovich and Bania⁽²⁹⁾ have shown that the phenomenon of corrosion fatigue is dependent on a thermally activated process (diffusion) and this occurs in conjunction with mechanical energy to produce sub-critical extension of a flaw. The total energy to overcome a barrier is supplied thermally and athermally. They assume that crack growth rate could be written as:

$$\left(\frac{da}{dt}\right)_{cf} = A \exp \frac{-Q_{cf}}{RT} \quad \dots (10)$$

where

$\left(\frac{da}{dt}\right)_{cf}$ = crack extension rate

A = a constant

Q_{cf} = apparent activation energy

T = temperature

R = gas constant \dots (11)

thus,

$$\ln \left(\frac{da}{dt}\right)_{cf} = \ln A - \frac{Q_{cf}}{RT}$$

A plot of $\ln \left(\frac{da}{dt} \right)_{cf}$ versus $\frac{1}{T}$ (Fig. 52) gives the apparent activation energy, Q_{cf} , for corrosion fatigue at the indicated ΔK levels, from the slope $\left(\frac{-Q_{cf}}{R} \right)$ of each line. These values of Q_{cf} are then plotted against $\frac{\Delta K^2}{E}$ in Fig. 53. Extrapolation of this plot to zero mechanical energy gives a characteristic activation energy value. This value comes out to 2.4 kcal/mol. This is small as compared to other activation energies reported⁽²⁹⁾ for diffusion of H in steel ($Q_{steel} \approx 10$ kcal/mol.). Again following the argument given by Antolovich and Bania, that this lower value could be due to a higher defect density in a plastic zone formed by cyclic loading which would result in increased ease of diffusion. Diffusion occurs more readily along grain boundaries, dislocations and high vacancy areas. This seems reasonable and it is suggested, tentatively, that hydrogen embrittlement seems to be the mechanism operating in corrosion fatigue. Moreover, this approach has been successfully applied in other works, details of which can be found in references 30 and 31. SEM fractography was of little value due to surface contamination.

SECTION V

CONCLUSIONS

1. Of the three different ageing treatments, 950°F/1 hr. ageing showed the best FCP characteristics.
2. The FCP rate is higher in lab air than in dry argon and is highest in the 3.5% NaCl solution, showing the effect of environment on FCP.
3. FCP rate in 3.5% NaCl solution is higher at lower ΔK levels for low frequency.
4. As compared to some other alloys, D6Ac, 300 maraging steel and HY 180, AF-1410 steel has a somewhat lower FCP rate at ΔK levels of 25 ksi $\sqrt{\text{in}}$ and above.
5. Dislocation rearrangement in martensite laths appears to be the predominant deformation mode in fatigue.
6. Corrosion fatigue is thermally activated and hydrogen diffusion is tentatively suggested to be the operative mechanism.
7. The relation between LCF and FCP suggested in another study by the author has been verified for AF 1410.
8. A very large value of the Coffin-Manson exponent was observed for all heat treatments studied. This indicates that application of this material in the high cycle régime is inadvisable.

TABLE 1 . COMPOSITION OF AF-1410 STEEL (Wt.%)^{*}

C	=	0.14
Ni	=	10.55
Co	=	13.69
Cr	=	2.06
Mo	=	1.08
Mn	=	0.14
P	=	0.01
S	=	0.006
Si	=	0.02
Al	=	0.035
Ti	=	0.011
N	=	0.020
O	=	<0.002
V	=	0.008
Fe	=	Balance

^{*} Exact composition of the plate received from U.S.Steel Corporation.

TABLE 2

MECHANICAL PROPERTIES OF AF 1410 AGED FOR 5 HRS AT 950°F

Yield Strength (0.2%) ksi	Tensile Strength ksi	%Red. Area	Toughness (K_Q) ksi $\sqrt{\text{in}}$	Mod. of Elasticity(E) ksi	CVN ft-lb
210	225	65	120	29×10^3	50

TABLE 3. LCF TEST RESULTS

Heat Treatment	Spec. #	Total Longitudinal Strain Range $\Delta \epsilon_t$	Longitudinal Plastic Strain Range $\Delta \epsilon_p$	Cycles to Failure	Average Stress $\Delta \sigma/2$ KSI
Aged at 950°F/5 hr age	2	0.013	0.0040	406	417
	4	0.020	0.0043	900	402
	11	0.017	0.0027	1000	400
	6	0.017	0.0029	1100	372
	19	0.011	0.0020	1300	374
	7	0.015	0.0014	1567	370
	8	0.03	0.0006	3410	336
	9	0.022	0.0004	5000	280
	1	0.034	0.0070	311	210
	3	0.023	0.0060	740	200
	14	0.018	0.0047	1638	195
	13	0.015	0.0033	1950	184
	12	0.013	0.0020	3030	162
	10	0.012	0.0013	3600	148
975°F/5 hr age	1		0.0014	2048	169
	1		0.0014	2405	181
750°F/5 hr age					

Annealed

TABLE 4. PARIS EQUATION CONSTANTS

Heat Treatment	Test Condition	m^*	R^{**}
950°F/5 hr. age	Lab air, R=0.1, f=10 Hz SEN, B=0.08"	1.83	1.73×10^{-10}
	Dry argon, R=0.1, f=10 Hz, SEN, B=0.08"	2.32	2.30×10^{-9}
	Dry argon, R=0.1, f=10 Hz, SEN, B=0.25"	2.16	9.0×10^{-10}
	Dry argon, R=0.4, f=10 Hz, SEN, B=0.08"	2.60	8.0×10^{-10}
	Dry argon, R=0.1, f=10 Hz, CT, B=0.25"	2.62	3.72×10^{-10}
	Dry argon, R=0.1, f=10 Hz, CT, B=0.5"	2.70	8.0×10^{-10}
750°F/5 hr. age	Lab air, R=0.1, f=10 Hz SEN, B=0.08"	1.61	4.90×10^{-10}
975°F/5 hr. age	Lab air, R=0.1, f=10 Hz SEN, B=0.08"	2.0	7.40×10^{-9}

** Rate constant in FCP equation when $\frac{da}{dn}$ is in in/cycle
(cm/cycle) and ΔK in ksi/in (MPa/m).

* m = FCP exponent in the Paris' FCP equation.

TABLE 5. SUMMARY OF LCF PARAMETERS USED TO PREDICT COFFIN-MANSON EXPONENT

Treatment	Cyclic Strain Hardening Exponent, n'	Plastic Work Exponent α	Predicted Coffin-Manson* Exponent β_p	Experimental Coffin-Manson Exponent β_e
Annealed (high strain)	0.207	3.42	0.24	0.24
Annealed (low strain)	0.207	0.54	1.45	1.53
950°F age	0.122	0.68	1.32	1.34

* Predicted using eq. 6

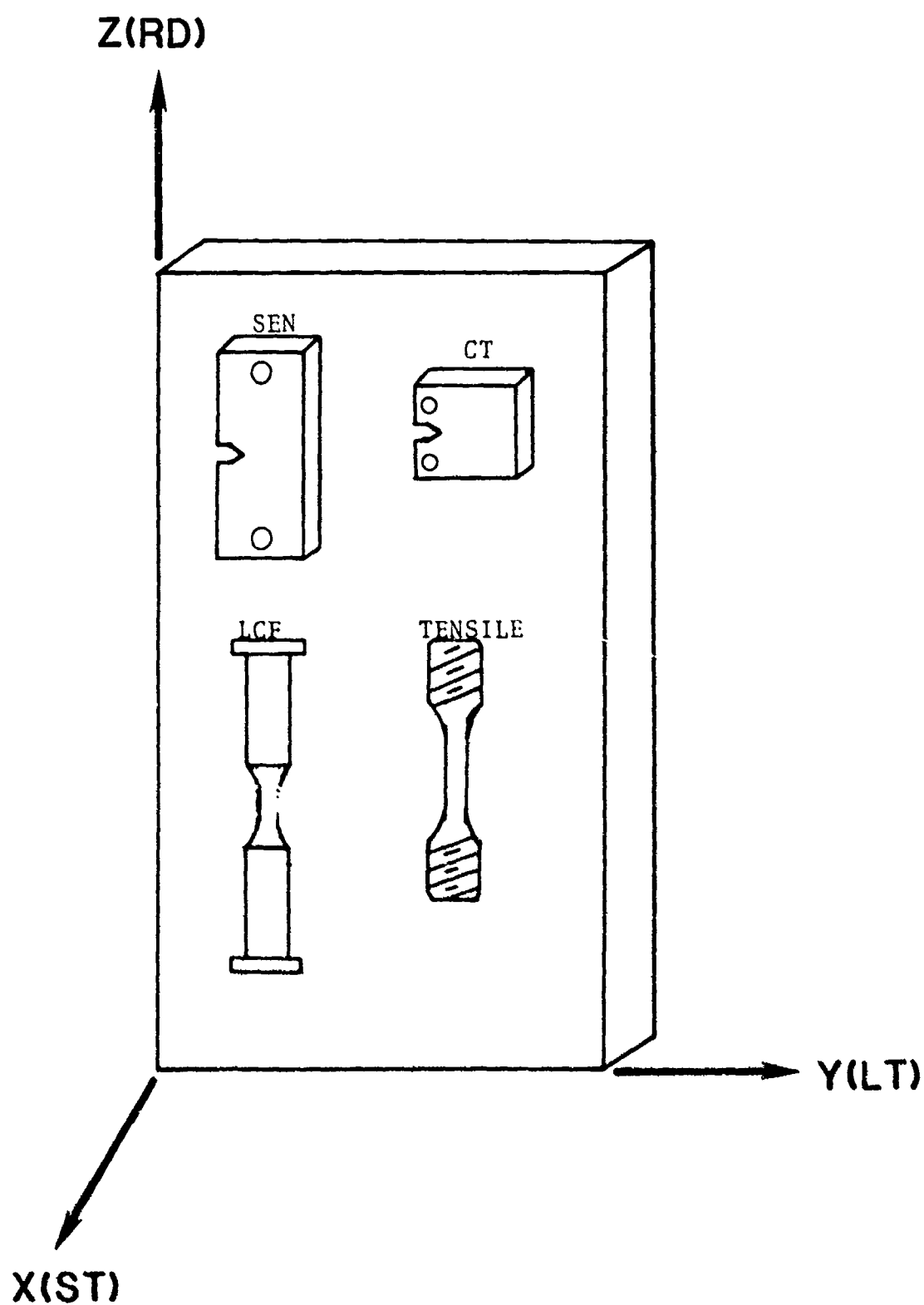


Fig. 1. Specimen configuration relative to the rolling direction of plate.

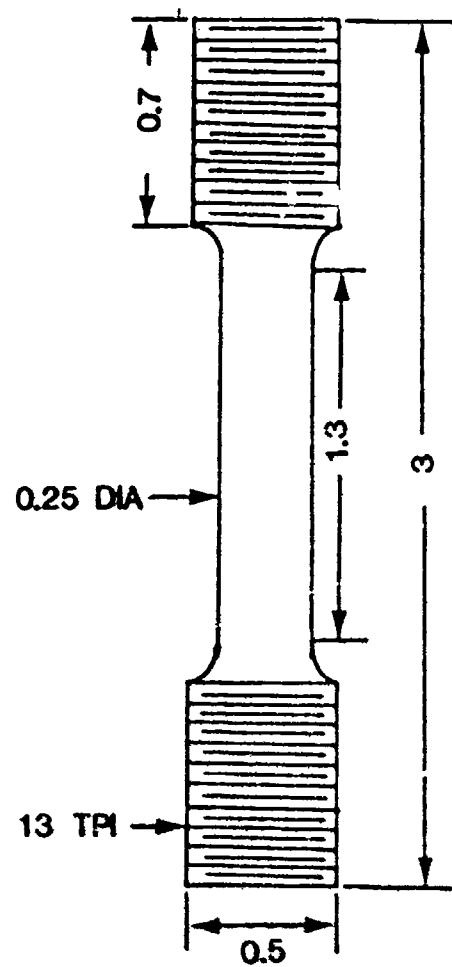


Fig. 2. Tensile test specimen.
(dimensions are in inches)

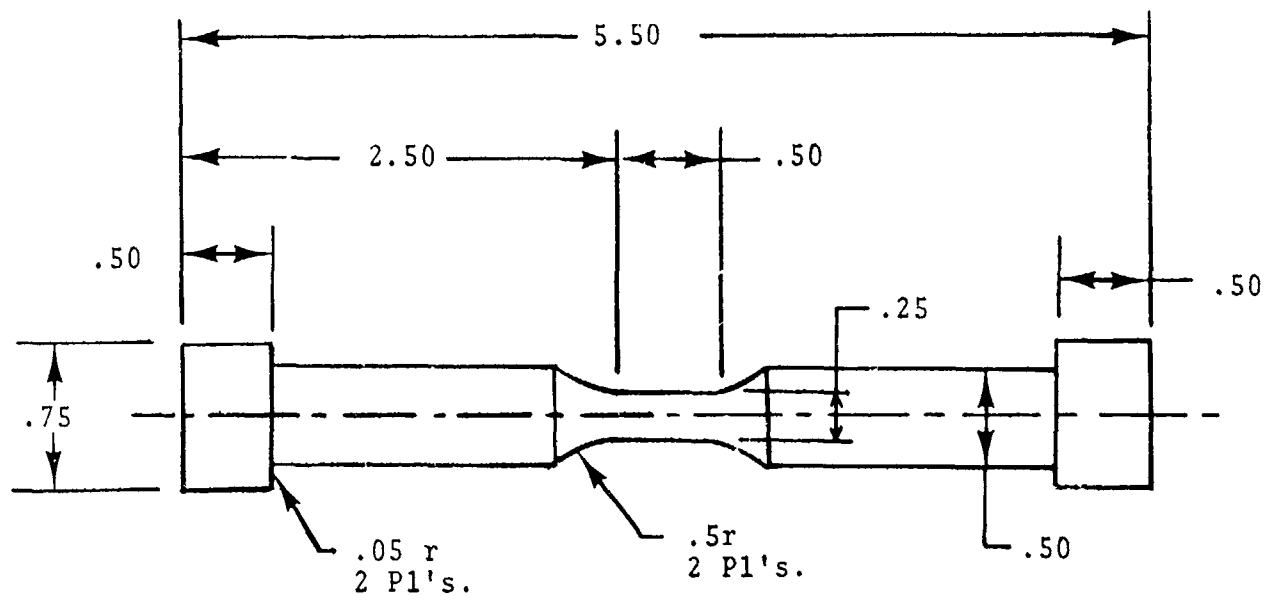


Fig. 3. Smooth bar longitudinal strain control LCF specimen.
All dimensions are in inches.

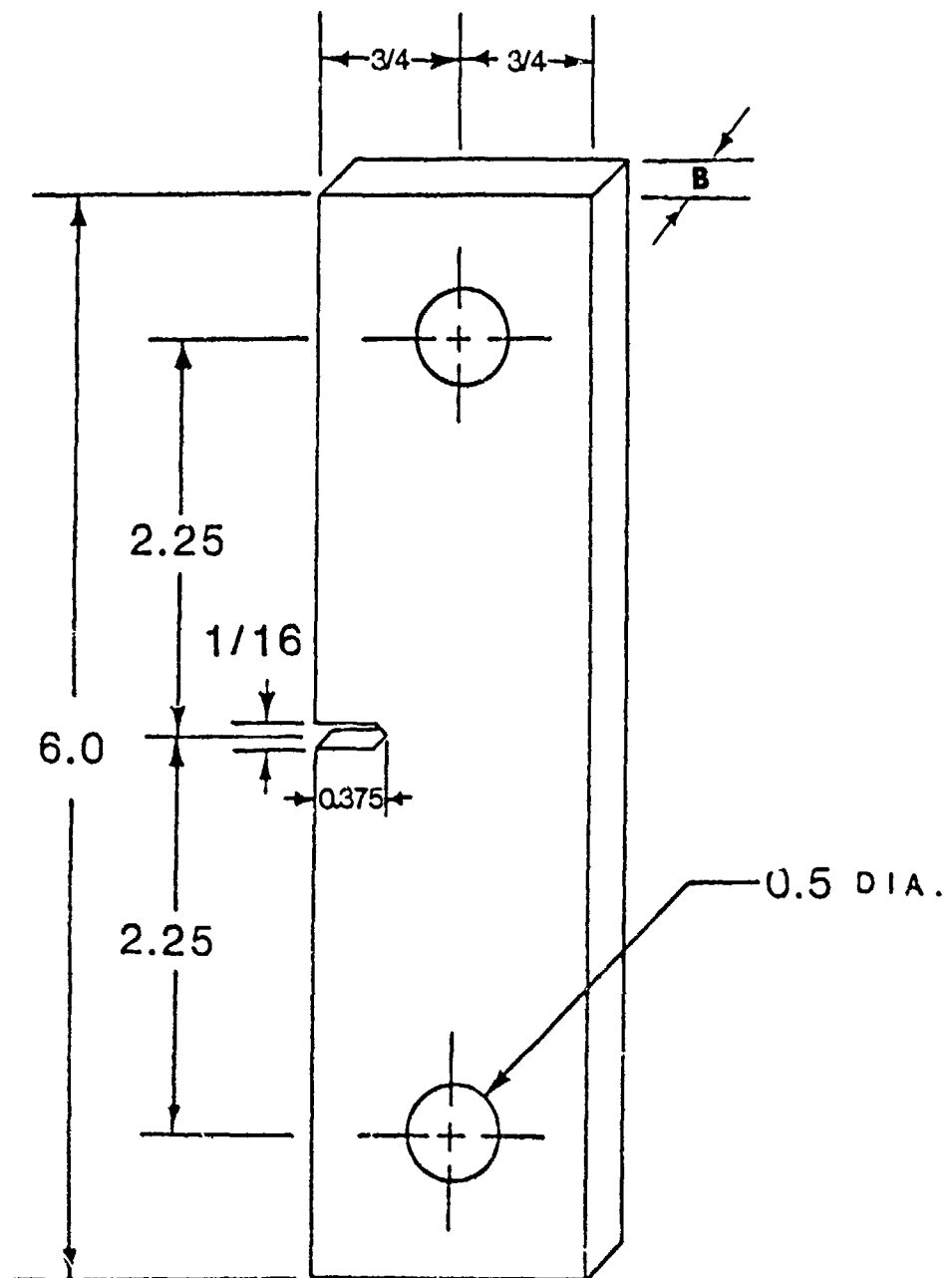


Fig. 4. Single edge notch specimen (SEN).
 (dimensions are in inches)
 Thicknesses of 0.08" and 0.25"
 were used.

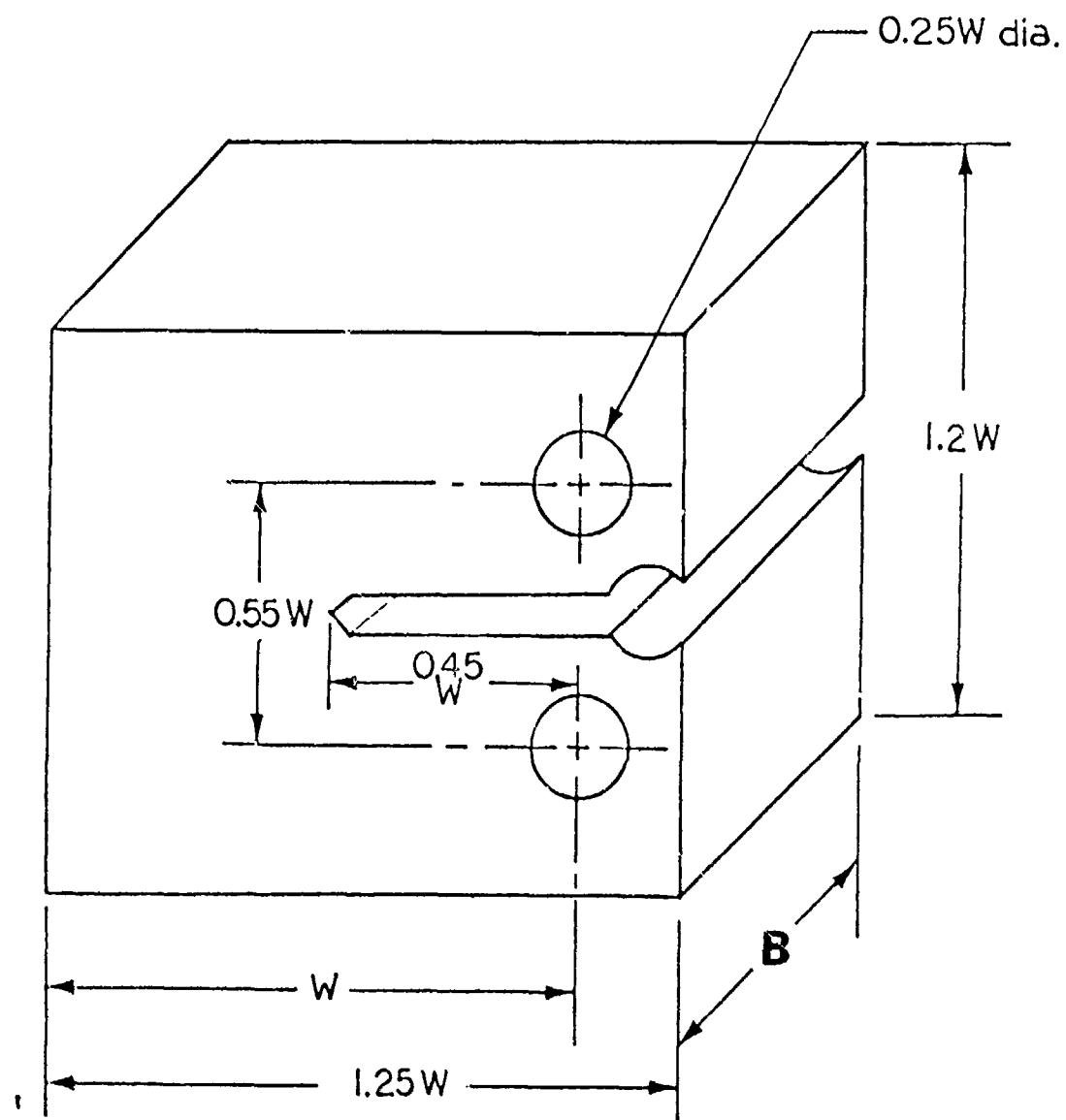


Fig. 5. Standard Compact specimen ($W=1$ inch).
 Thicknesses of 0.25" and 0.5" were used.

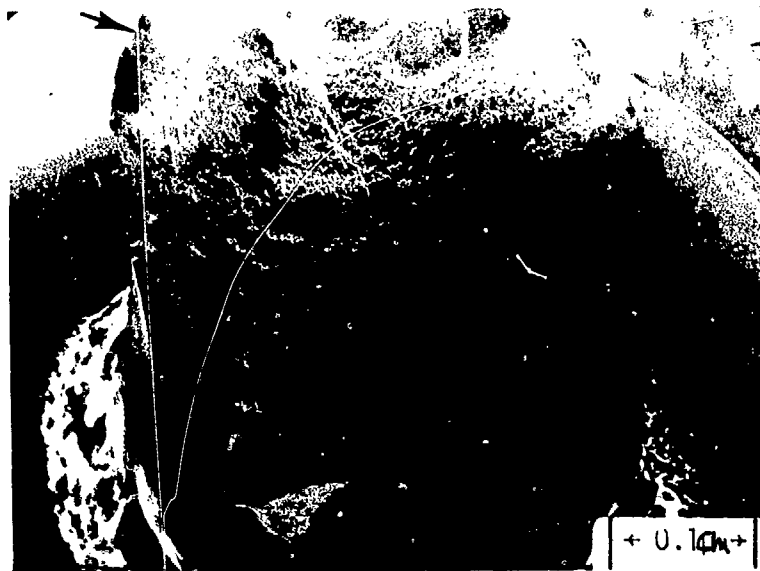


Fig. 6. Typical LCF specimen showing multiple initiation as indicated by the arrows.

Fig. 7a. Cumulative glide behavior of AF 1410 in the annealed condition.

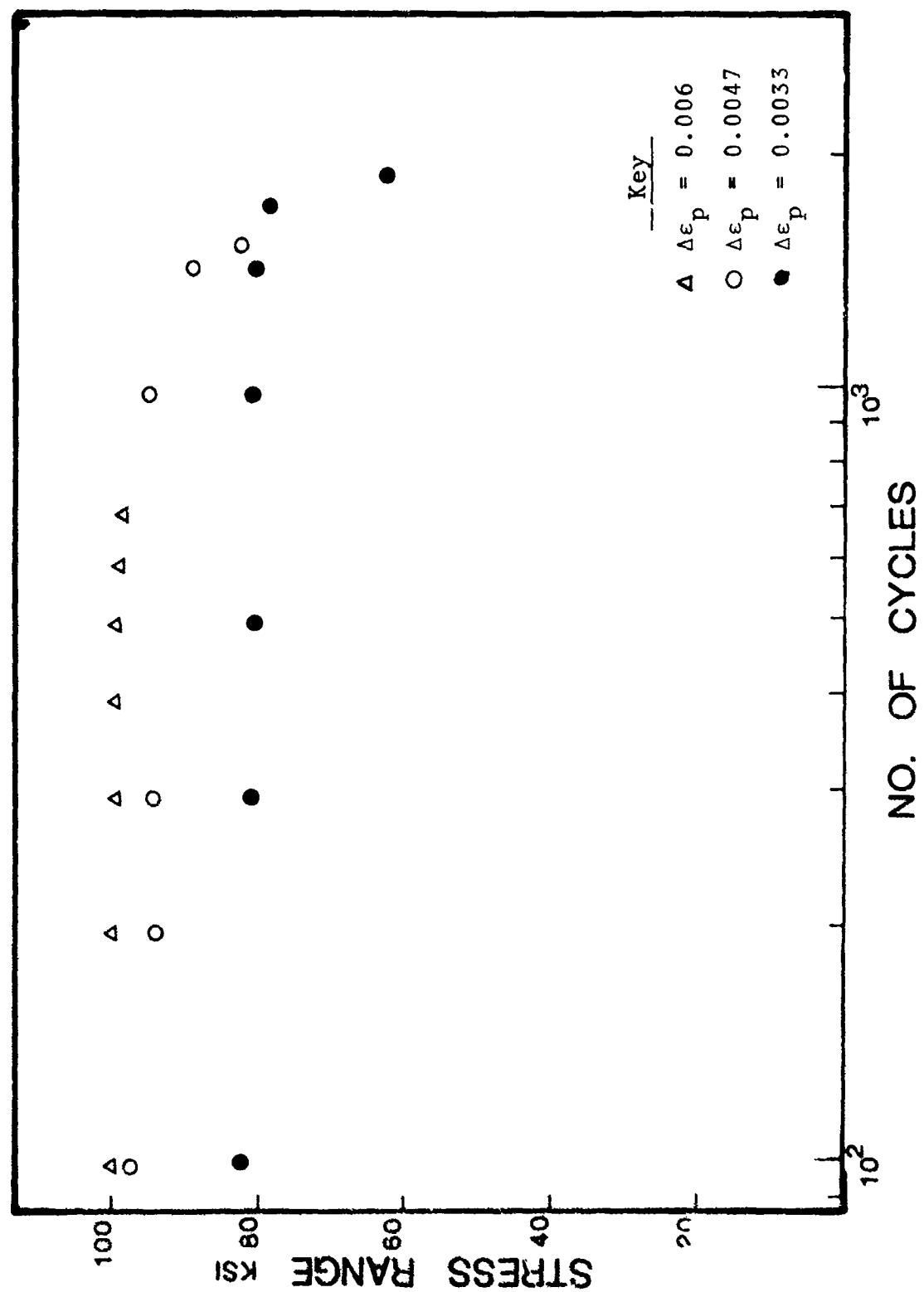
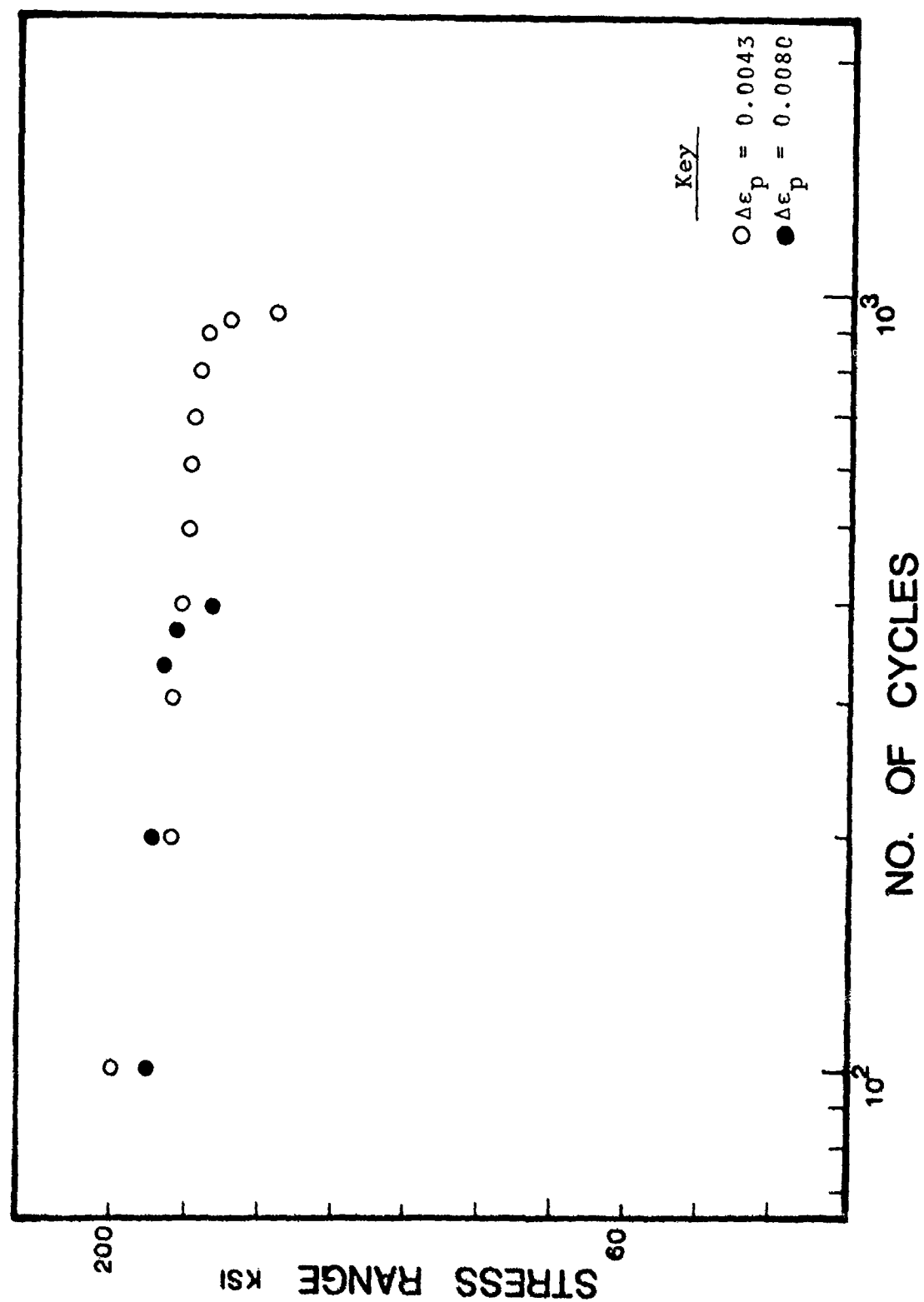


Fig. 7b. Cumulative glide behavior at AF 1410 aged at 950°F for 5 hr.



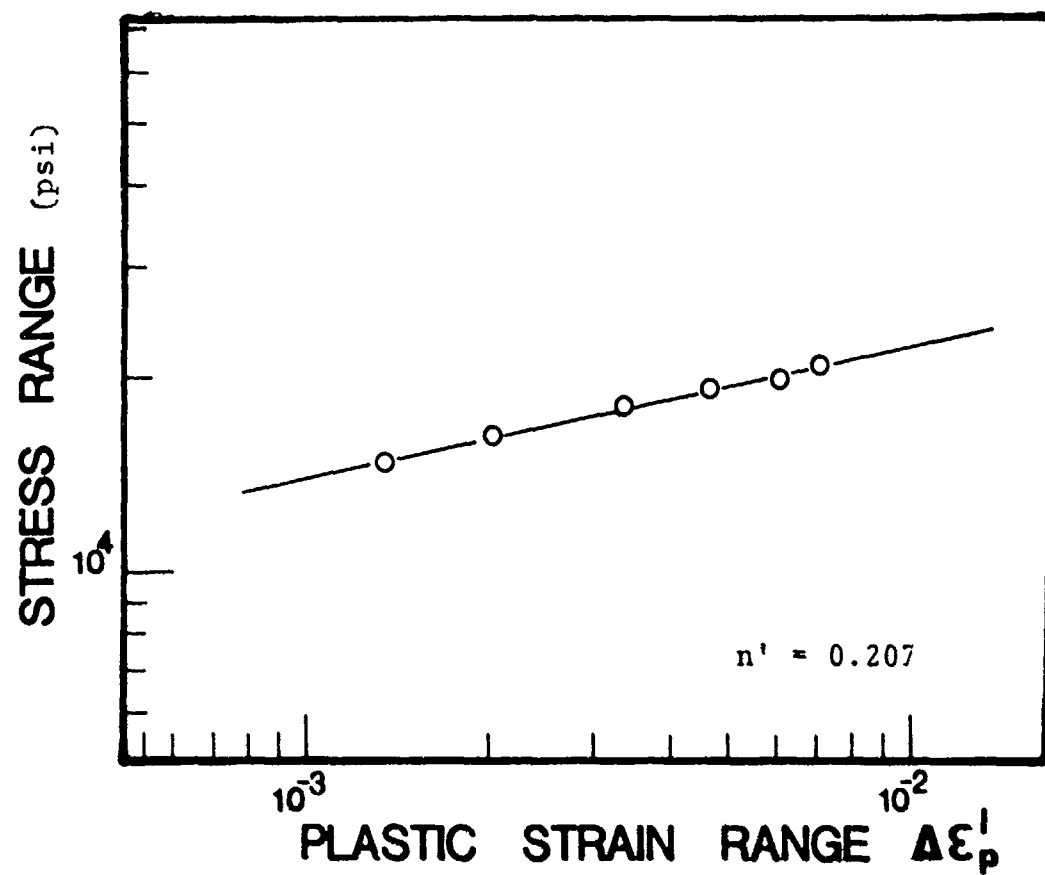


Fig. 8a. Cyclic stress/strain curve of annealed AF 1410.

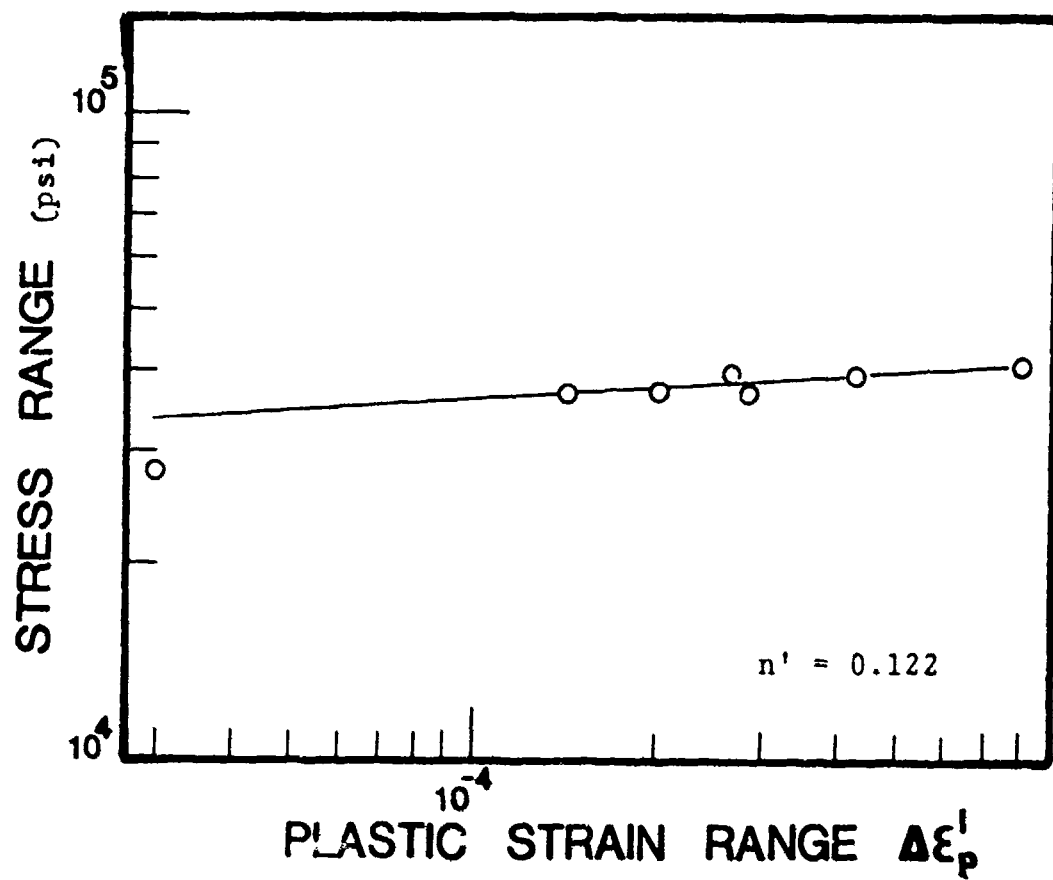


Fig. 8b. Cyclic stress-strain curve for AF 1410 heat treated at 950° for 5 hrs and air cooled.

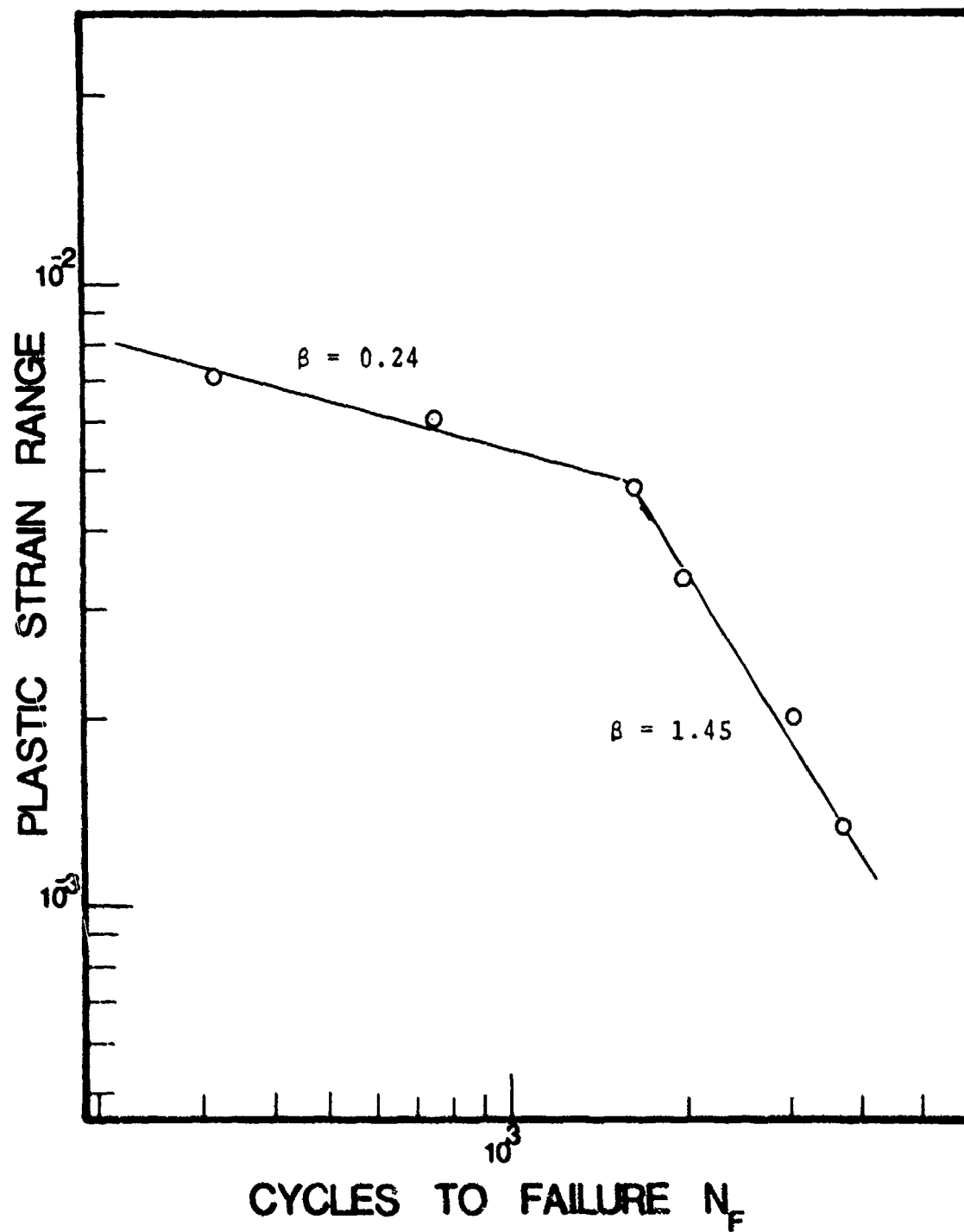


Fig. 9a. Coffin-Manson curve of annealed AF 1410.

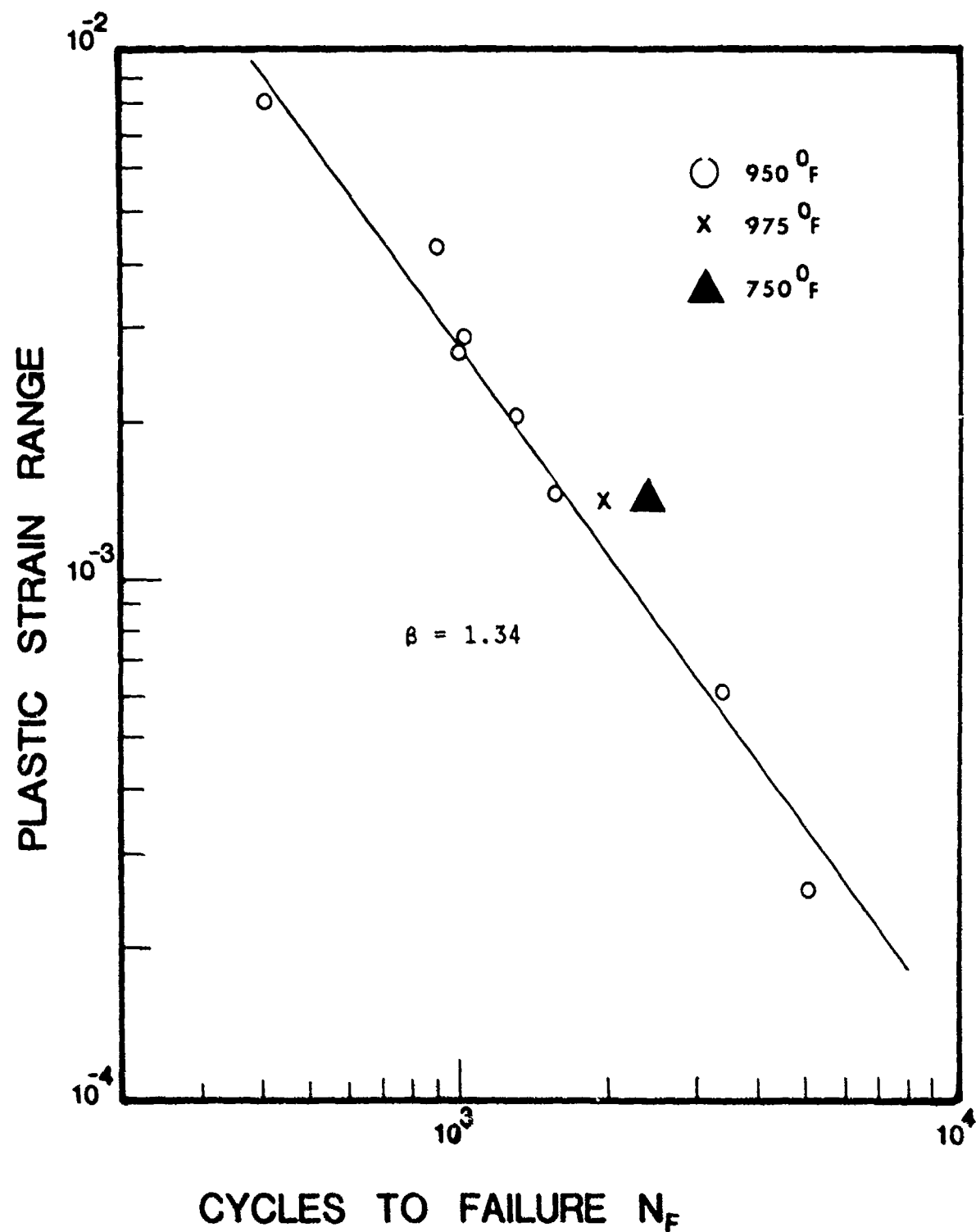


Fig. 9b. Coffin-Manson curve of AF 1410 heat treated at 950° for 5 hrs. air cooled.

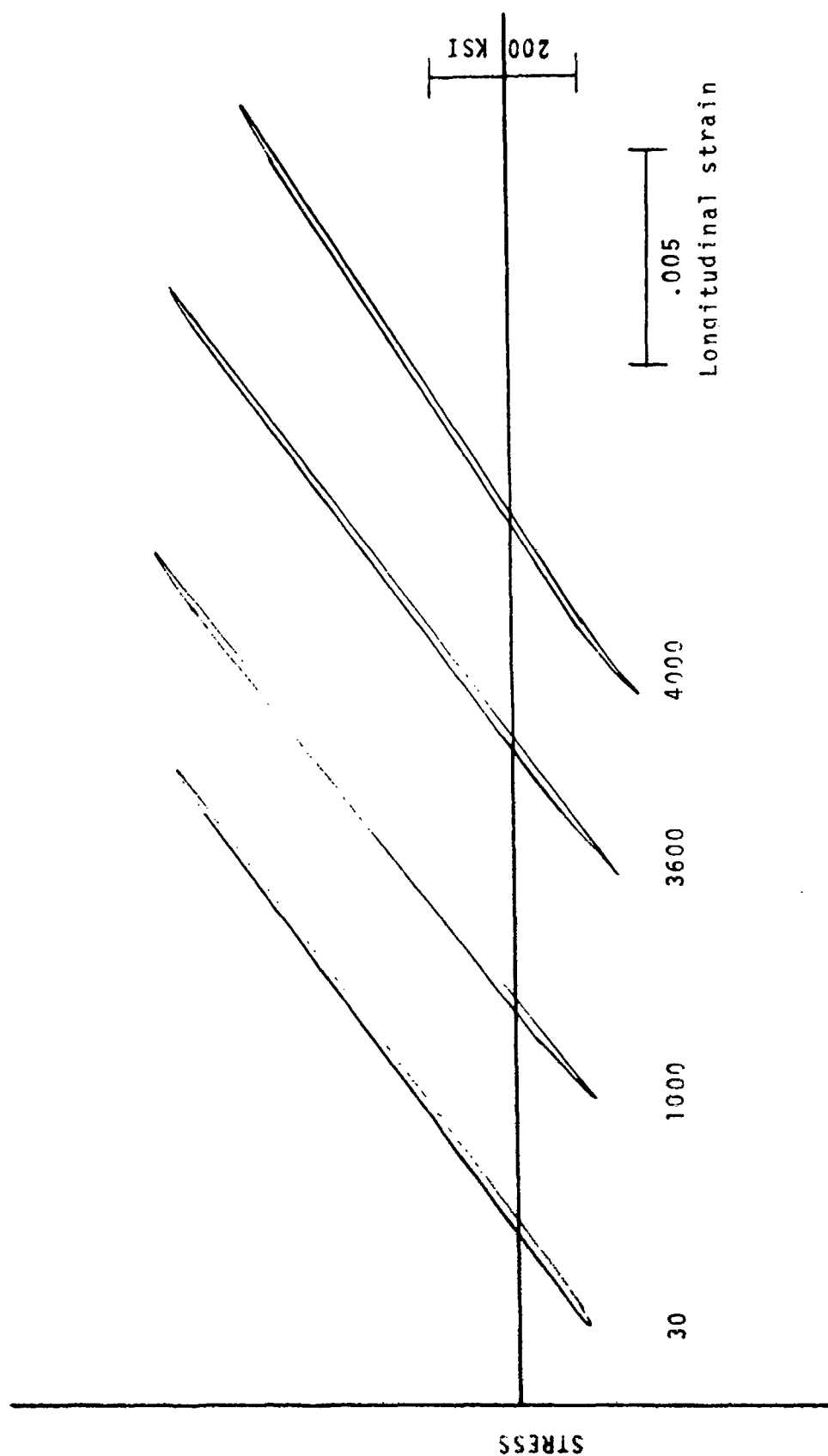


Fig. 10a. Representative hysteresis loops for AF 1410. Aged at 950°F for 5 hrs.
The numbers refer to cycles. $\Delta\epsilon_p^L = 0.29\%$.

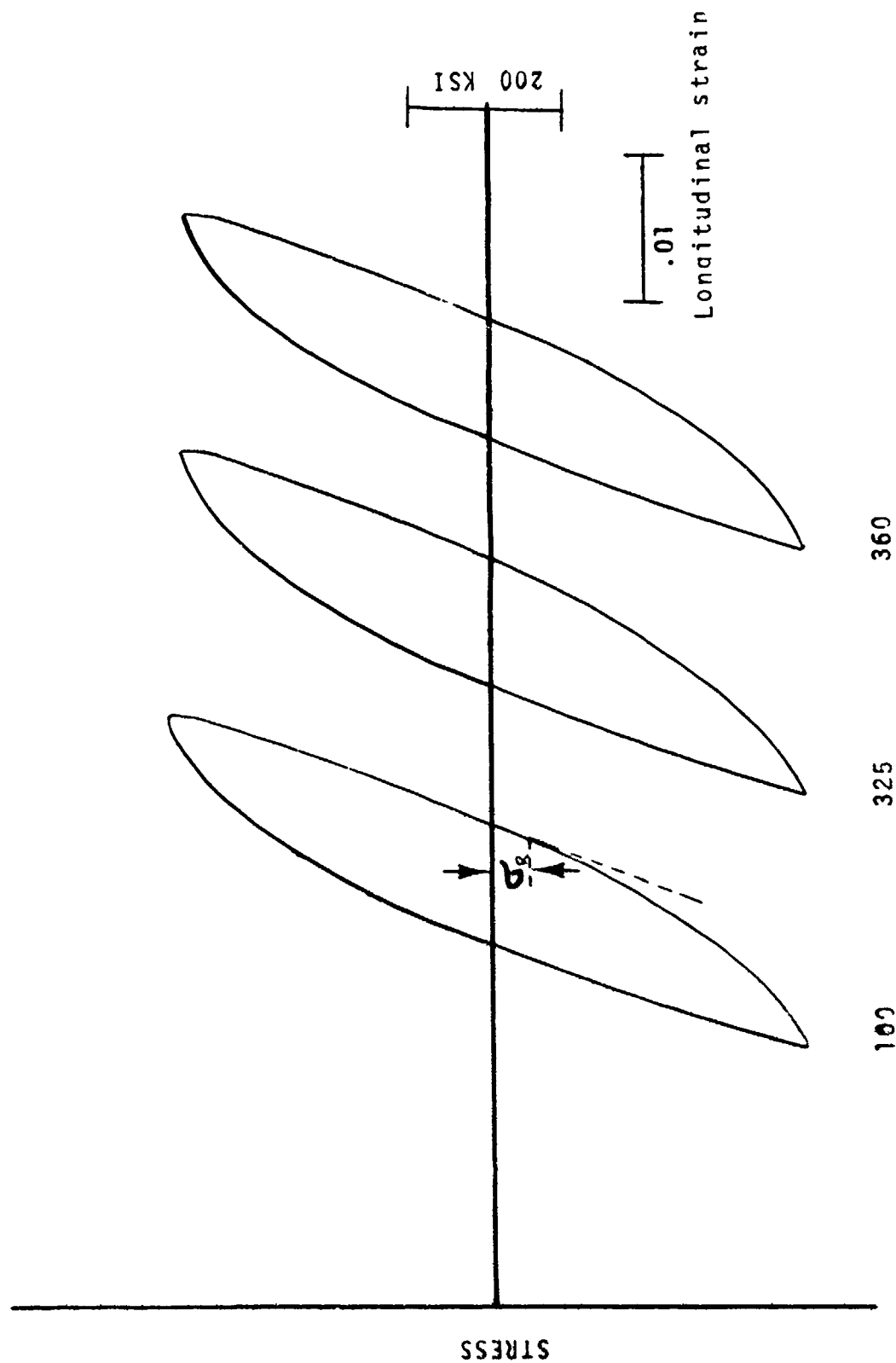


Fig. 10b. Representative hysteresis loops for AF 1410. Aged at 950°F for 5 hrs. The numbers refer to cycles and σ_R is the Bauschinger stress.

$$\Delta \epsilon_p^{\frac{1}{2}} = .803\%$$

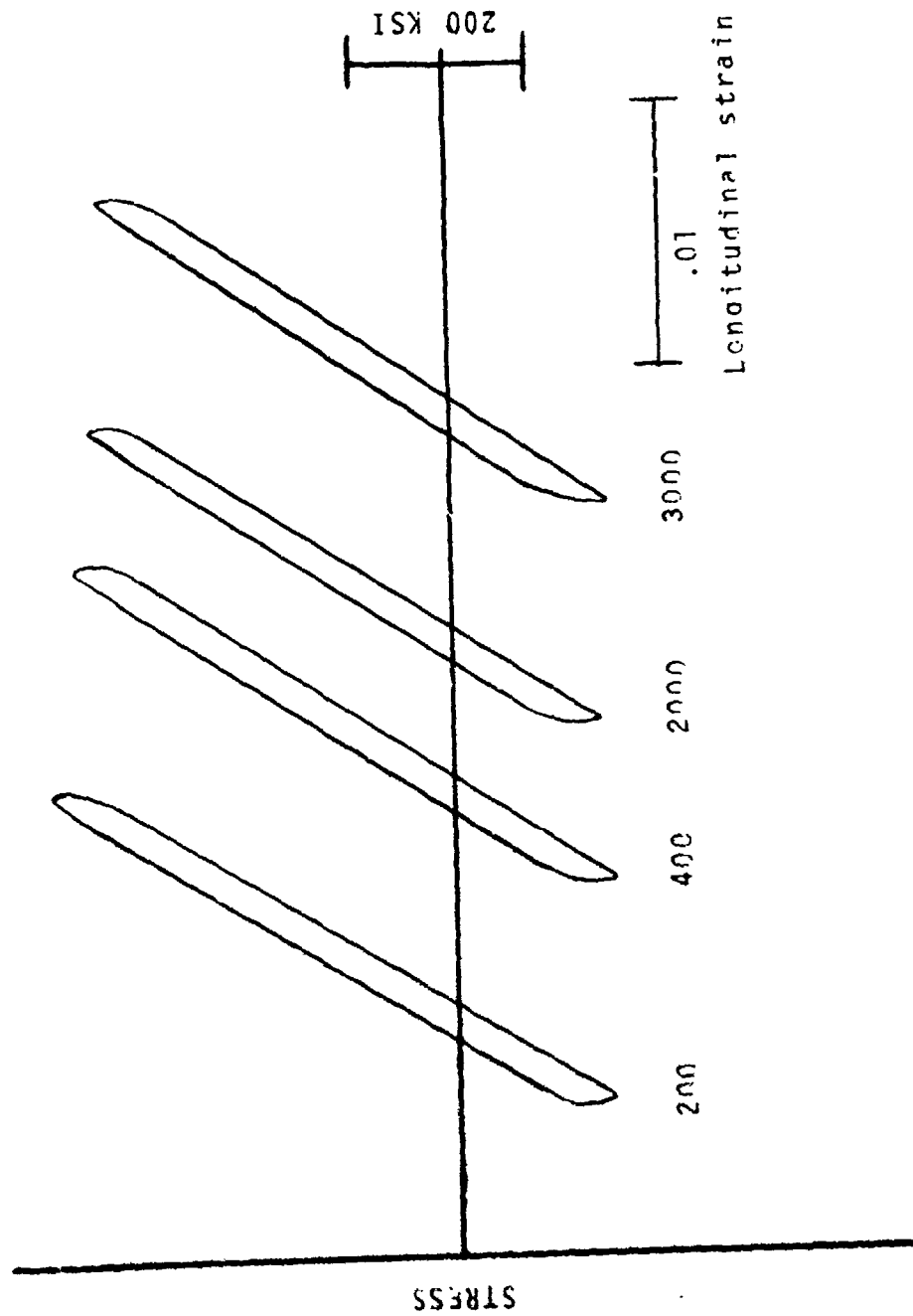


Fig. 10c. Representative Hysteresis loops for AF 1410 in the annealed condition.
The numbers refer to cycles. $\Delta\epsilon_p = 0.134\%$.

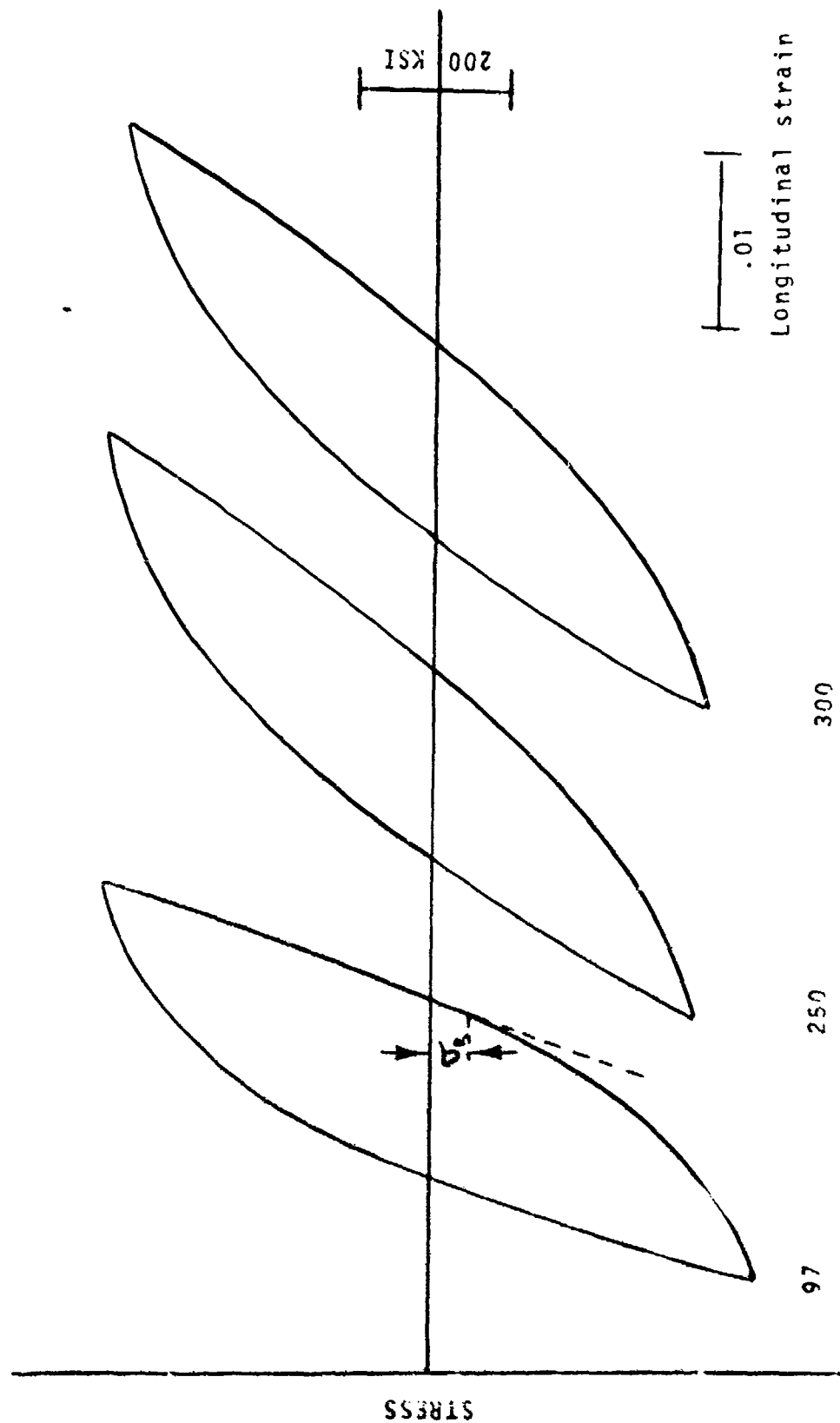


Fig. 10d. Representative hysteresis loops for AF 1410 in the annealed condition. The numbers refer to cycles and the Bauschinger stress is denoted σ_R . $\Delta\epsilon_p^2 = 0.702\%$.

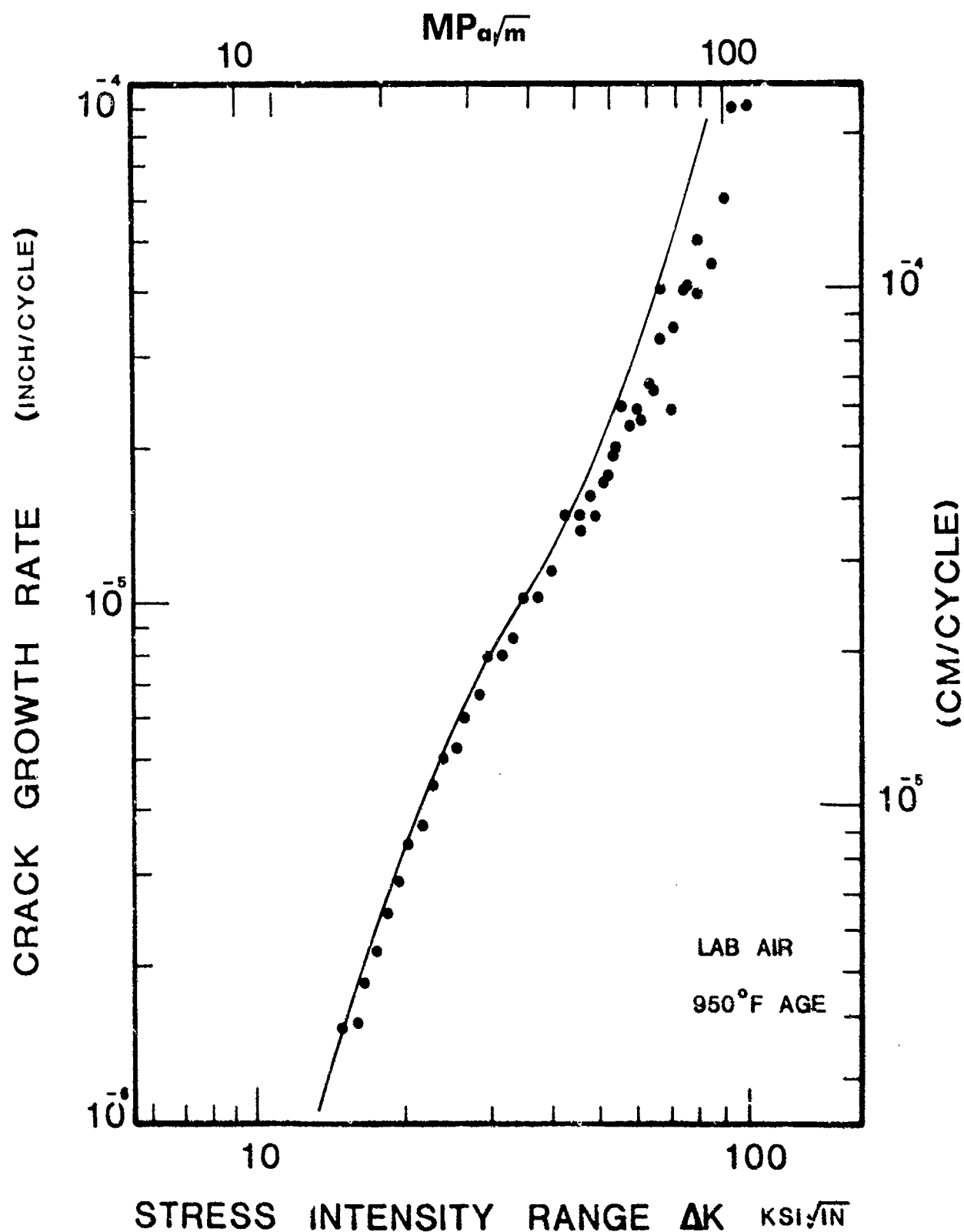


Fig. 11. Fatigue crack growth rate versus stress intensity range for AF 1410 steel aged at 950°F, tested at 10 Hz with $R = 0.1$. SEN specimen, $B = 0.08$ ". Solid line is the data fit in all FCP figures.

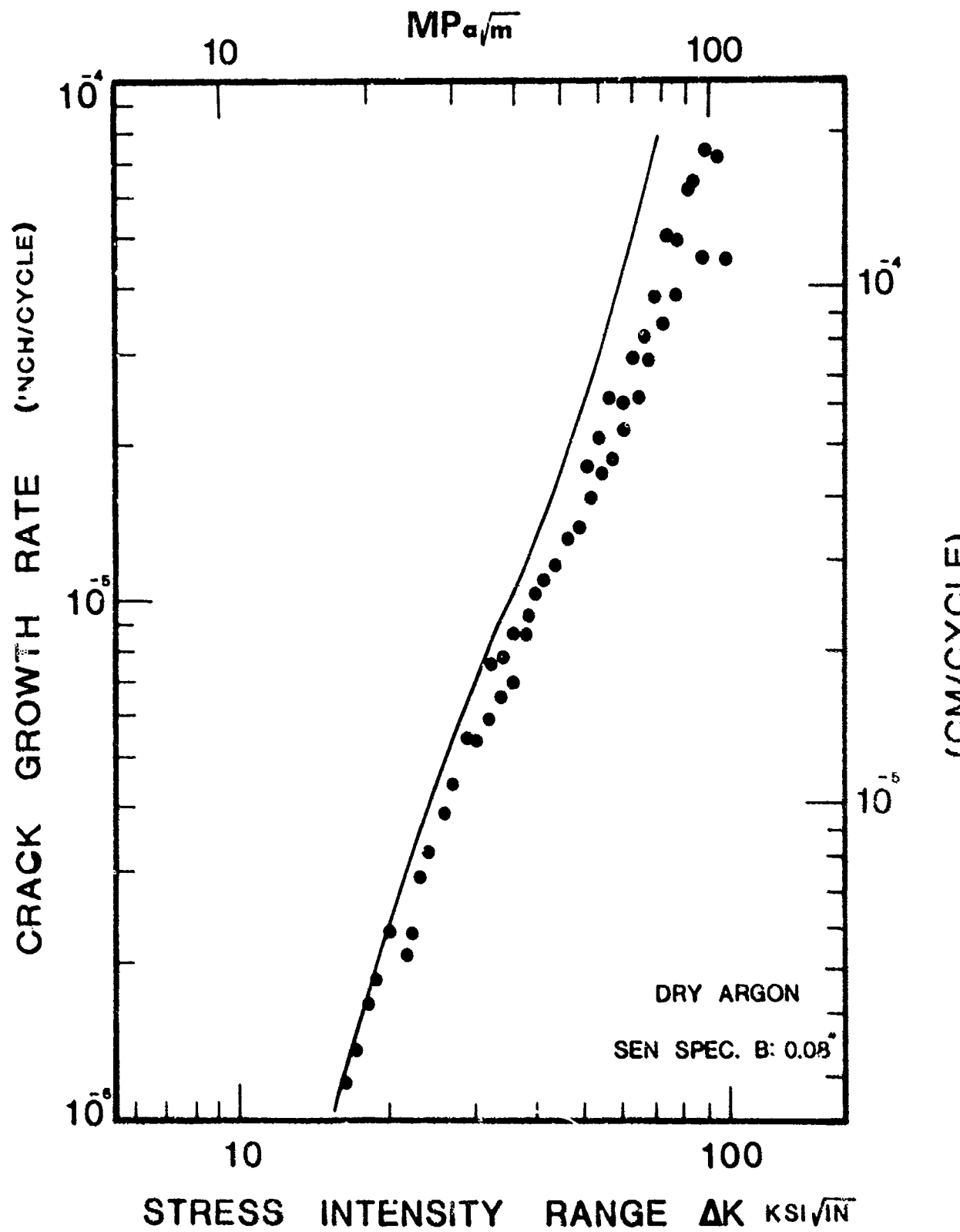


Fig. 12. Fatigue crack growth rate versus stress intensity range for AF 1410 steel, 950°F/5 hrs. age, tested at 10 Hz. and $P = 0.1$.

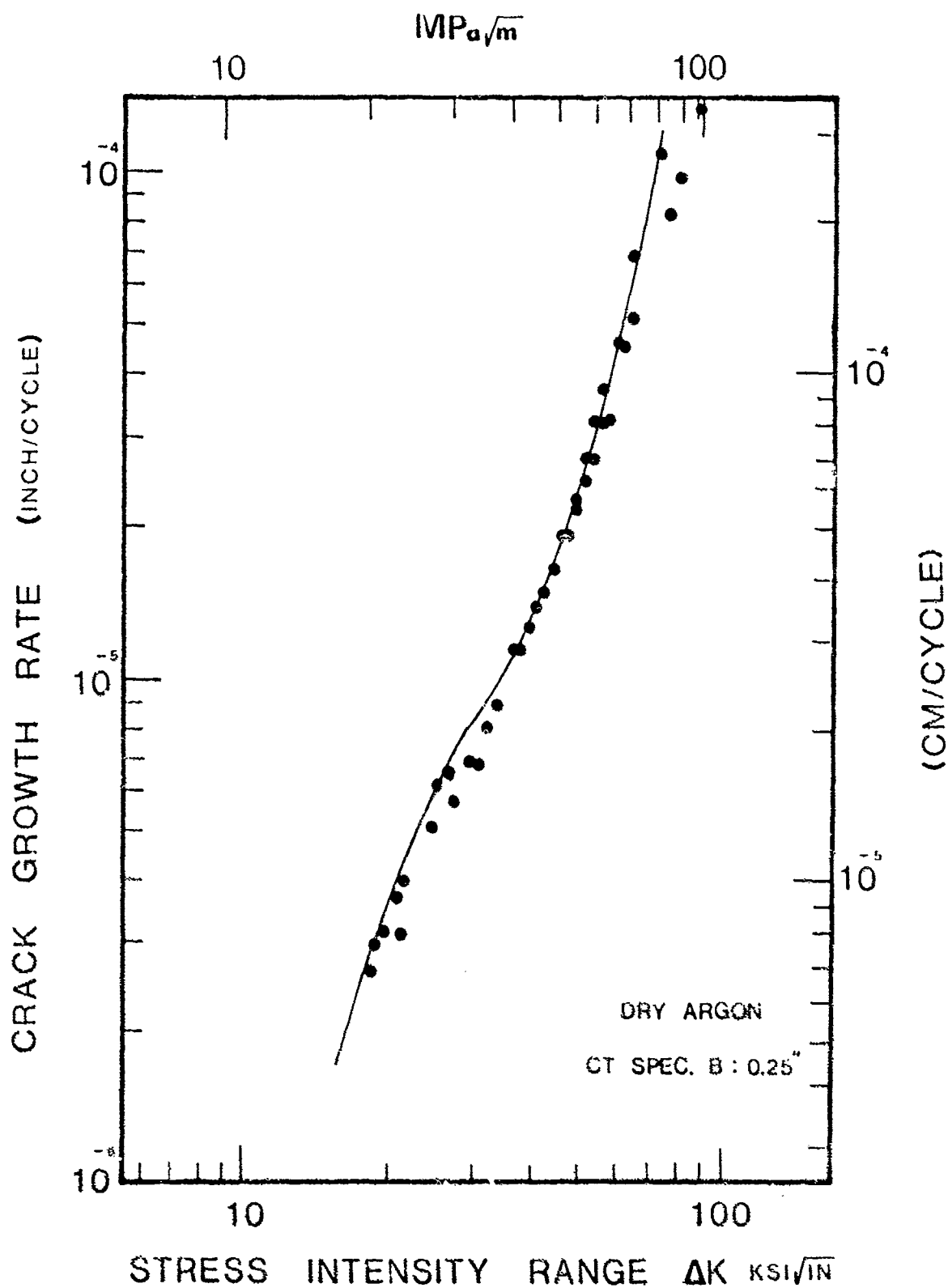


Fig. 13. Fatigue crack growth rate versus stress intensity range for AF 1410 steel, 950°F/5 hrs. age, tested at 10 Hz. and $R = 0.1$.

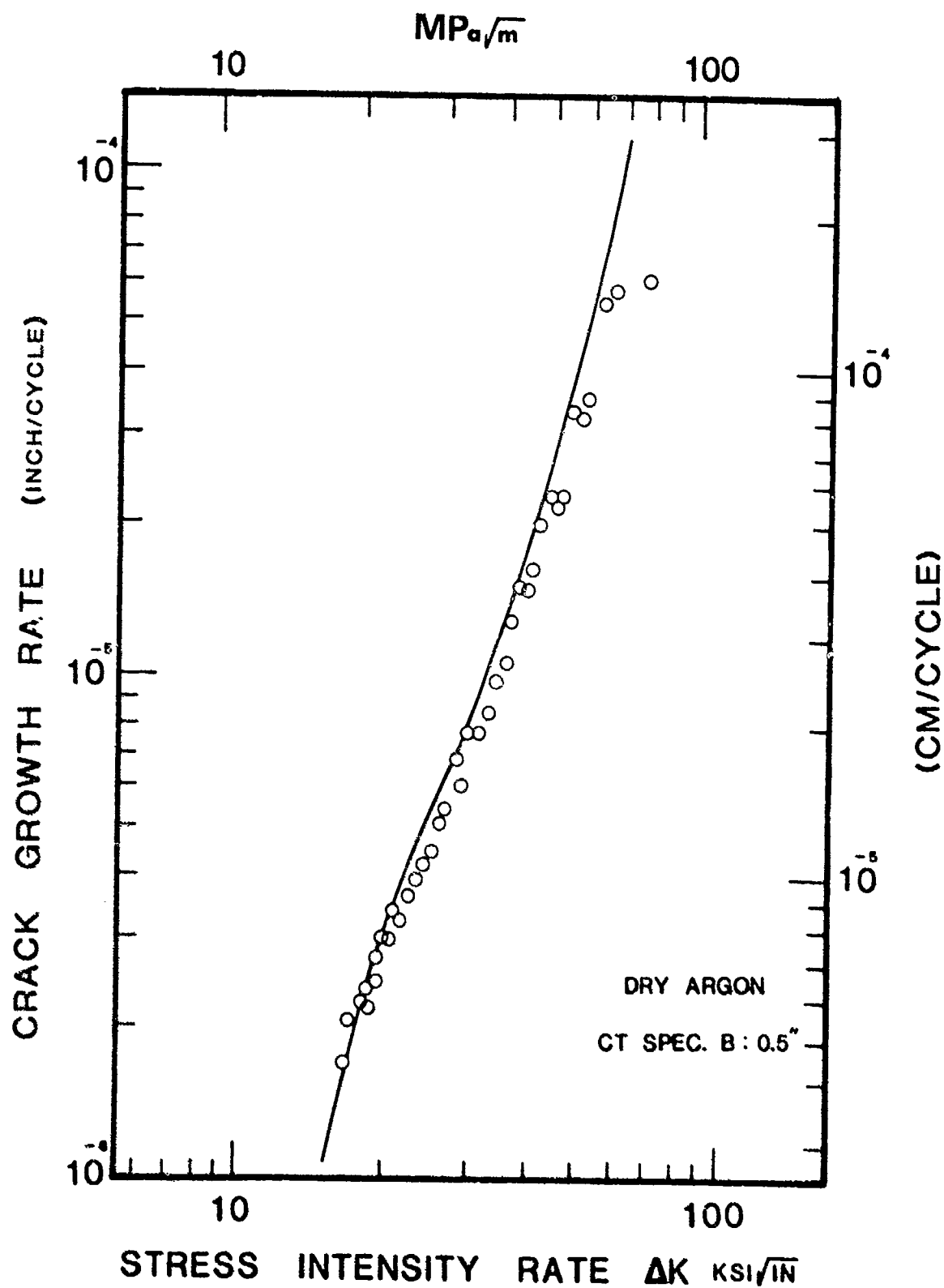


Fig. 14. Fatigue crack growth rate versus stress intensity range for AF 14°C steel, 950°F/5 hrs. age, tested at 10 Hz. and $R = 0.1$.

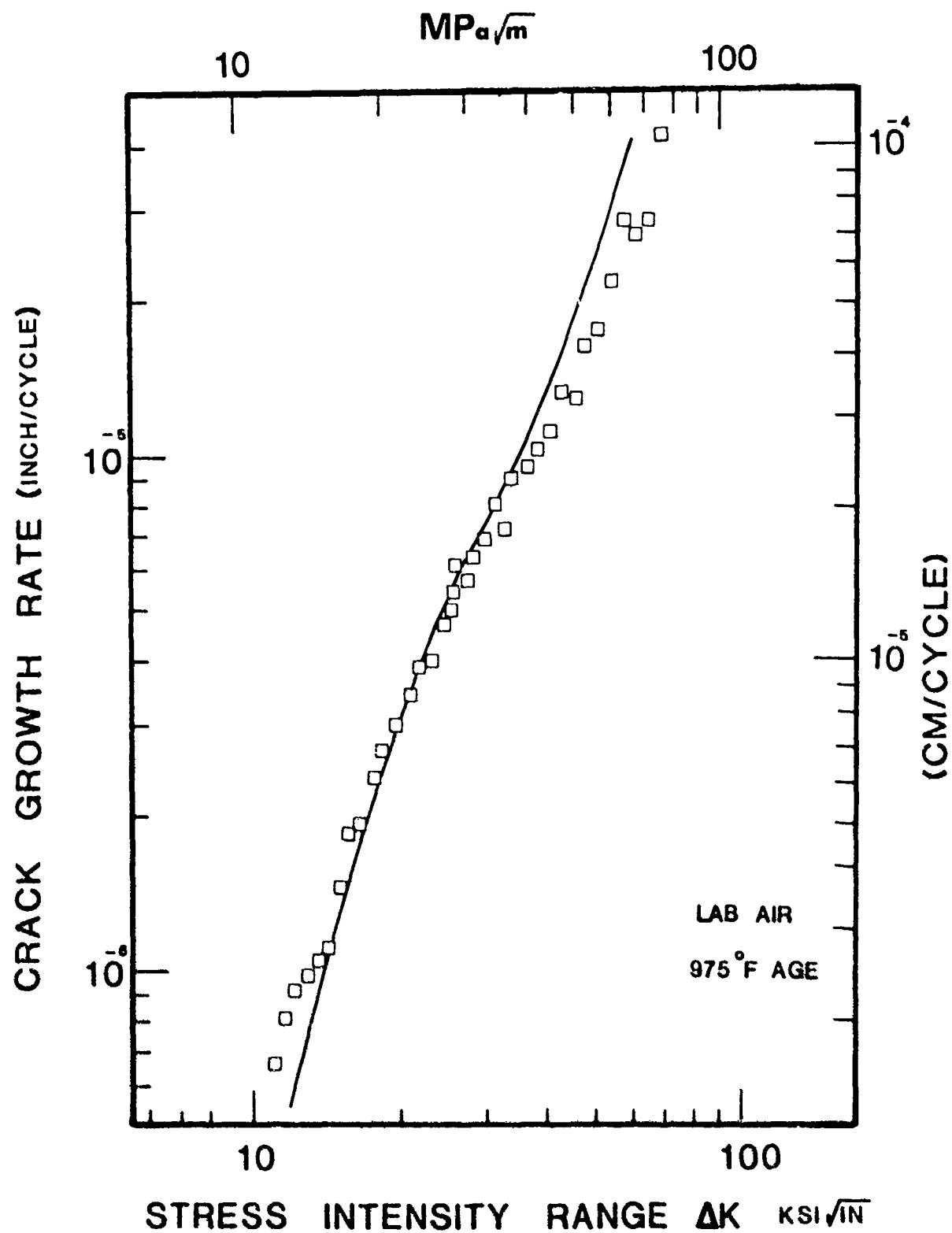


Fig. 15. Fatigue crack growth rate versus stress intensity range for AF 1410 steel aged 5 hrs. at 975°F, tested at $f = 10$ Hz. and $R = 0.1$. SEN specimen, $B = 0.08$ ".

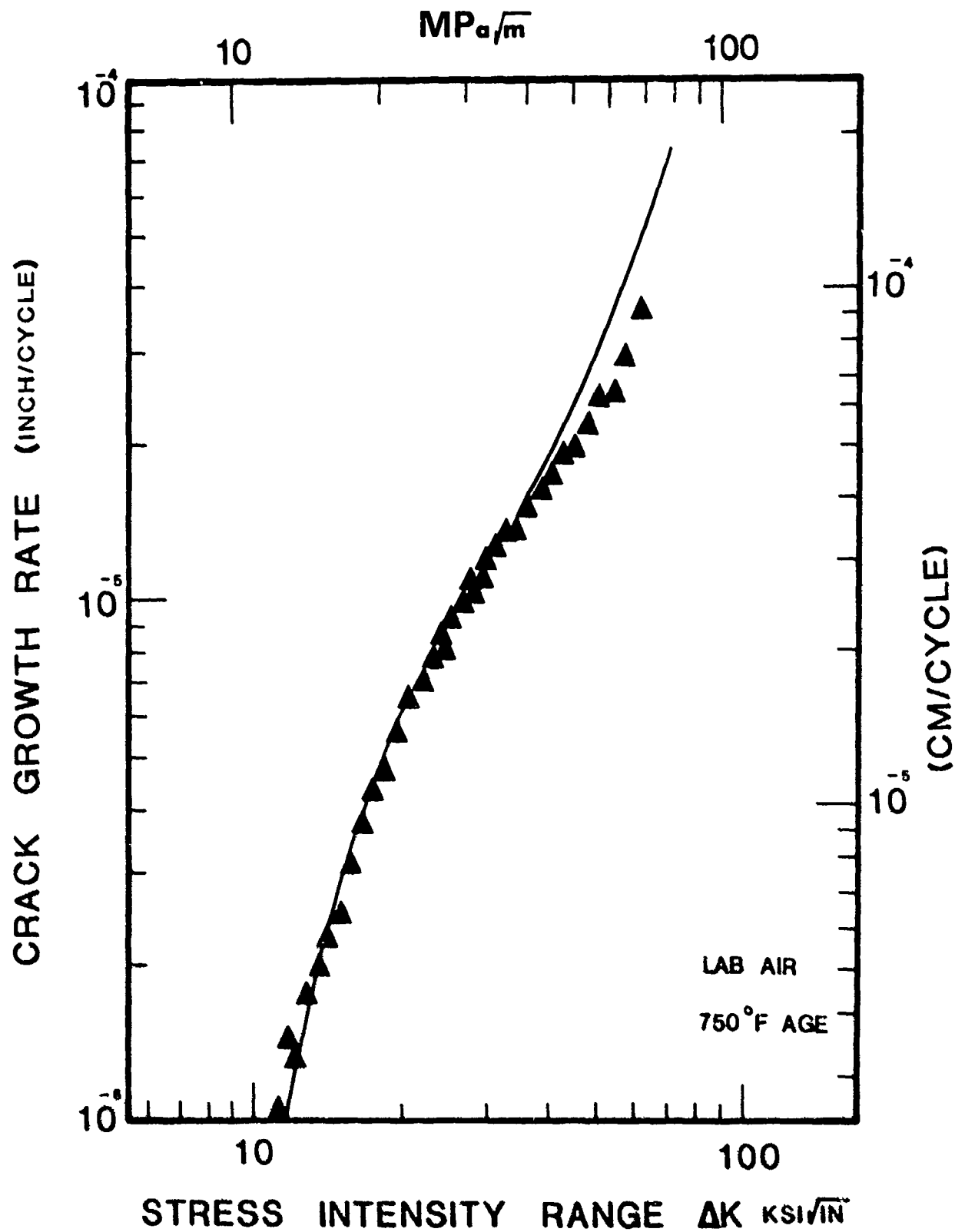


Fig. 16. Fatigue crack growth rate versus stress intensity range for AF 1410 steel aged 5 hrs. at 750°F, tested at 10 Hz. and $R = 0.1$. SEN specimens, $B = 0.08$ "

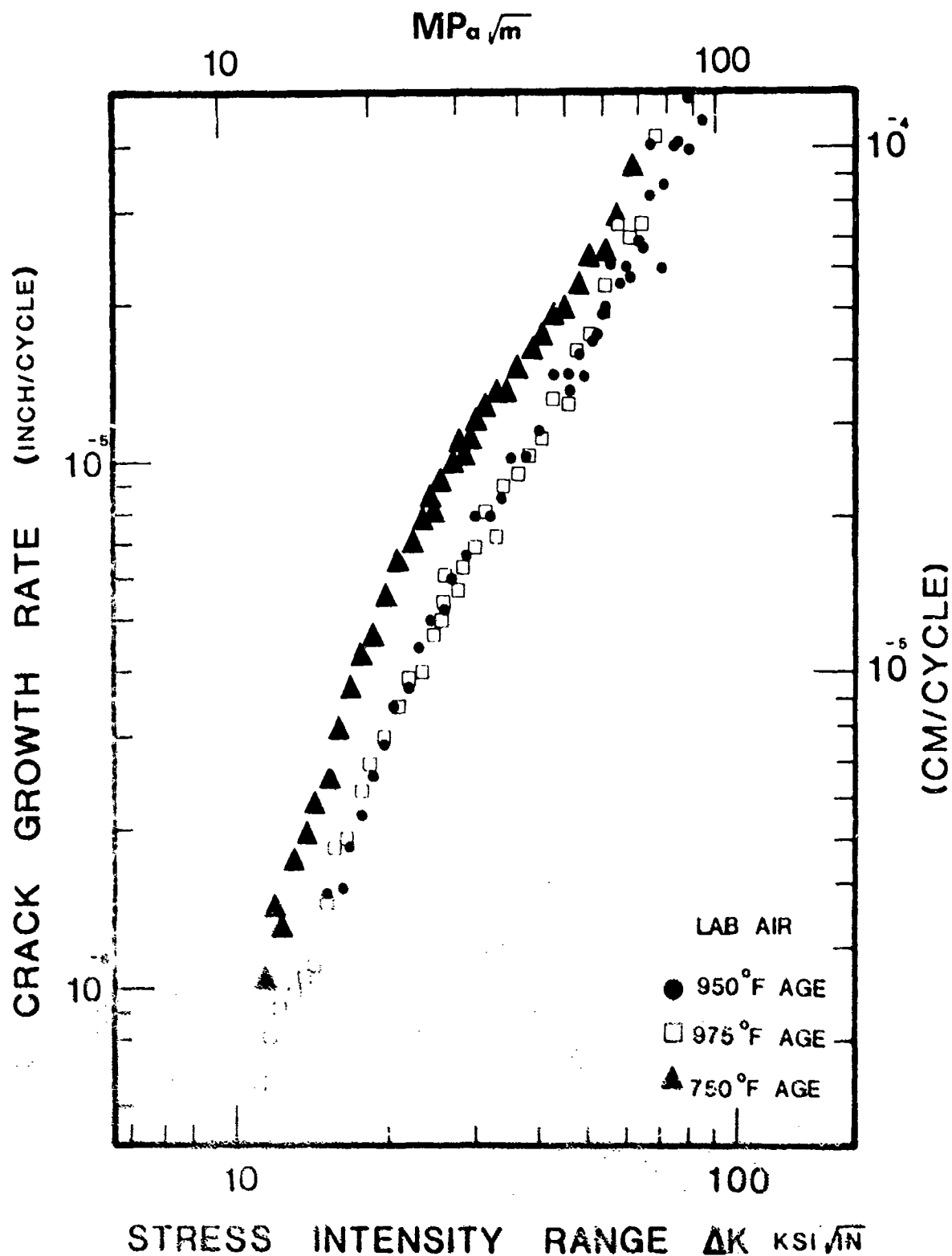


Fig. 17. Effect of ageing temperature on fatigue crack growth rate of AF-1410 steel. All tests run at 10 Hz. and $R = 0.1$. SEN specimens, $B = 0.08$.

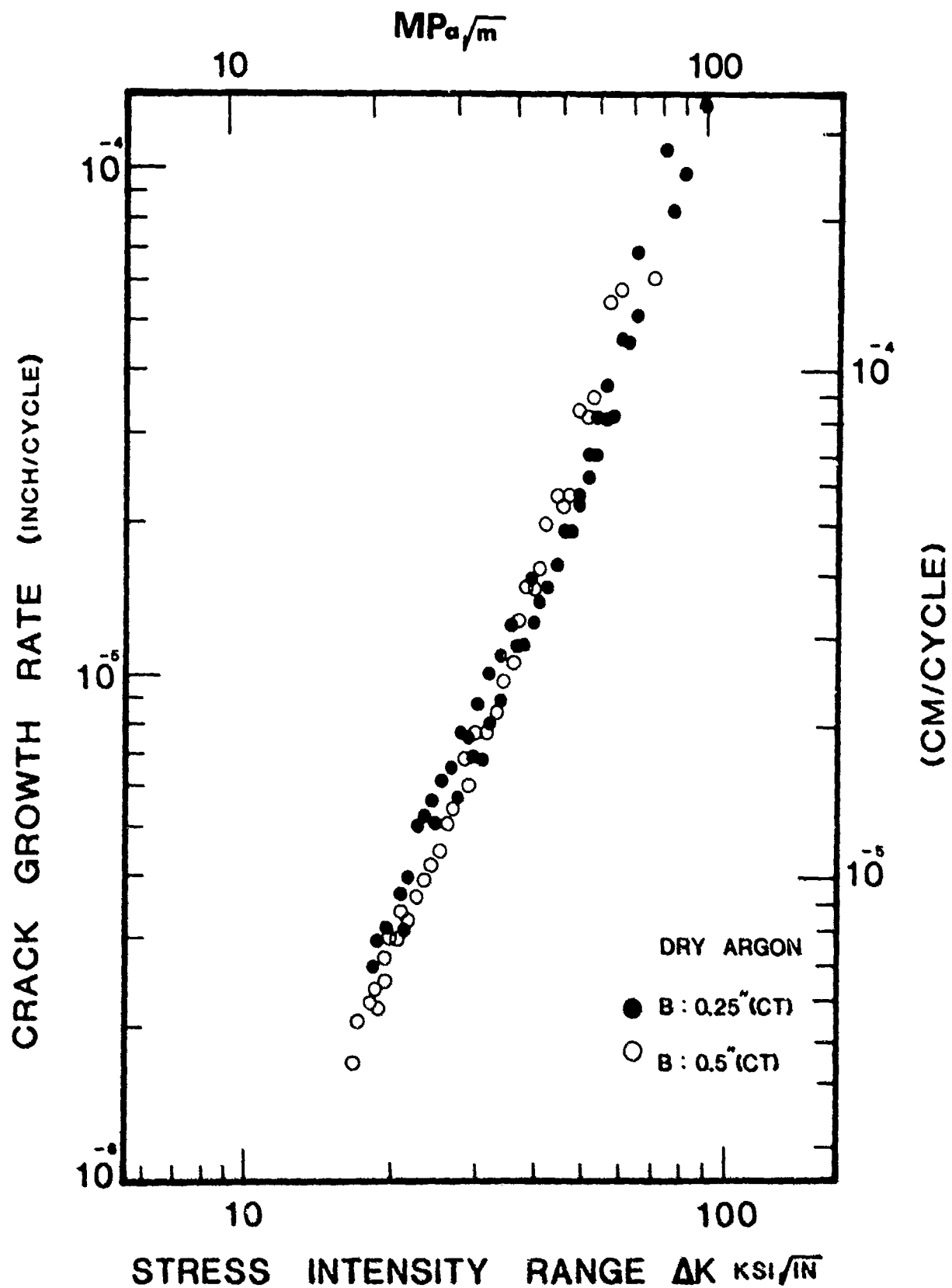


Fig. 18. Effect of thickness on fatigue crack growth rate of AF-1410 steel, 950°F/5 hrs. age, tested at 10 Hz. and R = 0.1.

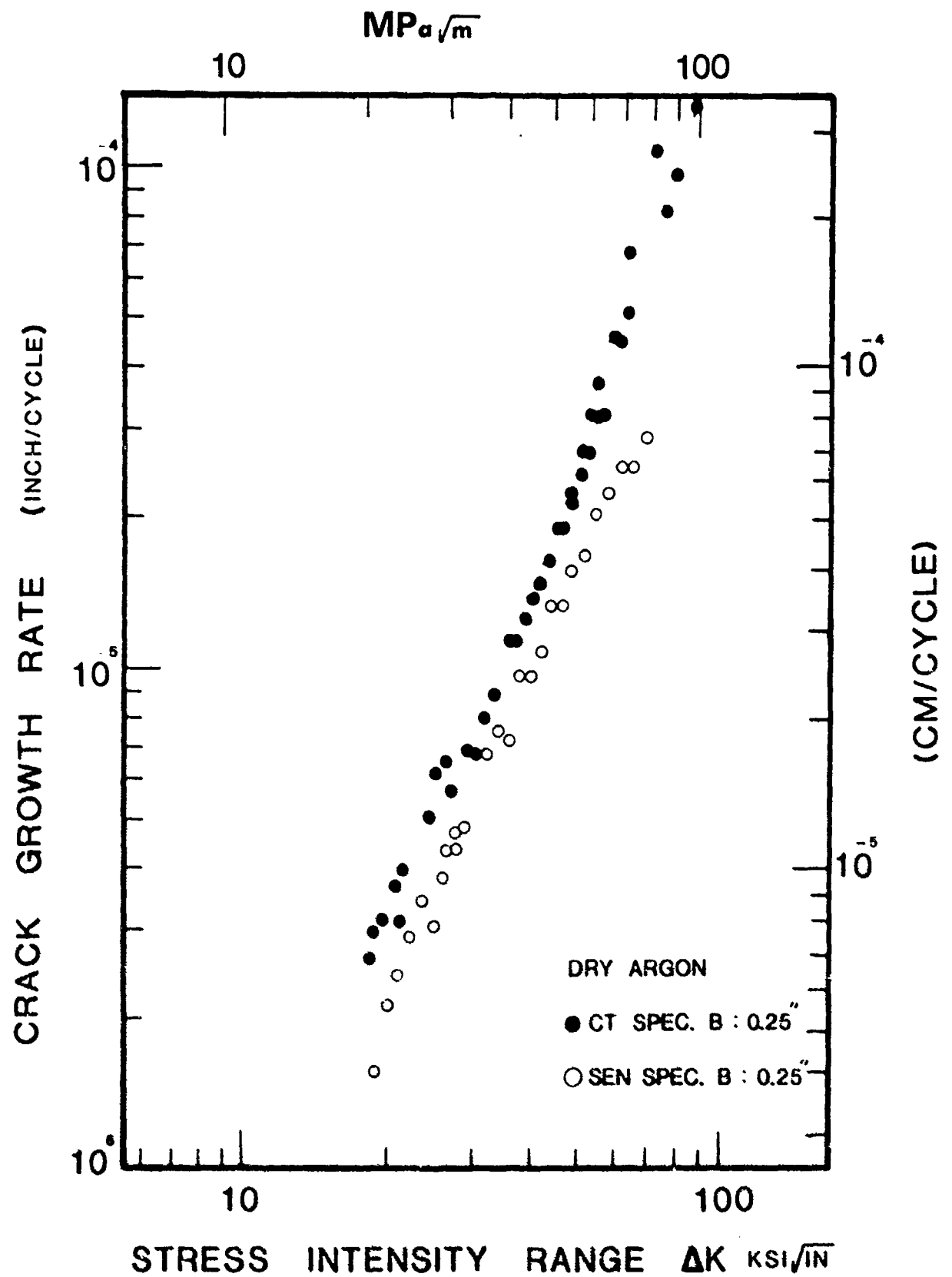


Fig. 19. Effect of specimen geometry on fatigue crack growth rate of AF-1410 steel, 950°F/5 hrs. age, tested at 10 Hz. and $R = 0.1$.

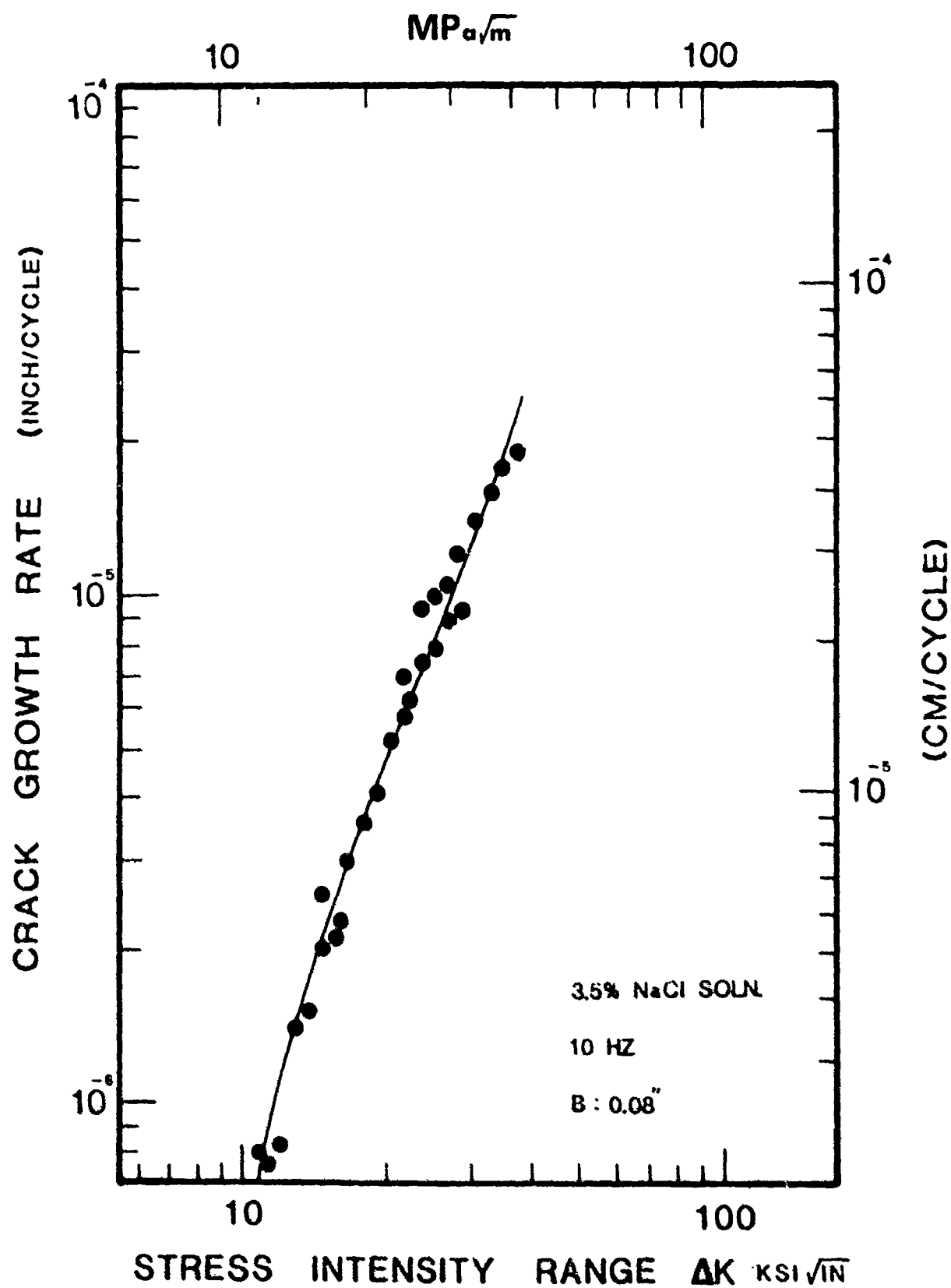


Fig. 21. FCP curve of AF-1410 steel, 950°F/5 hrs. age, in 3.5% NaCl solution, R=0.1, SEN specimen.

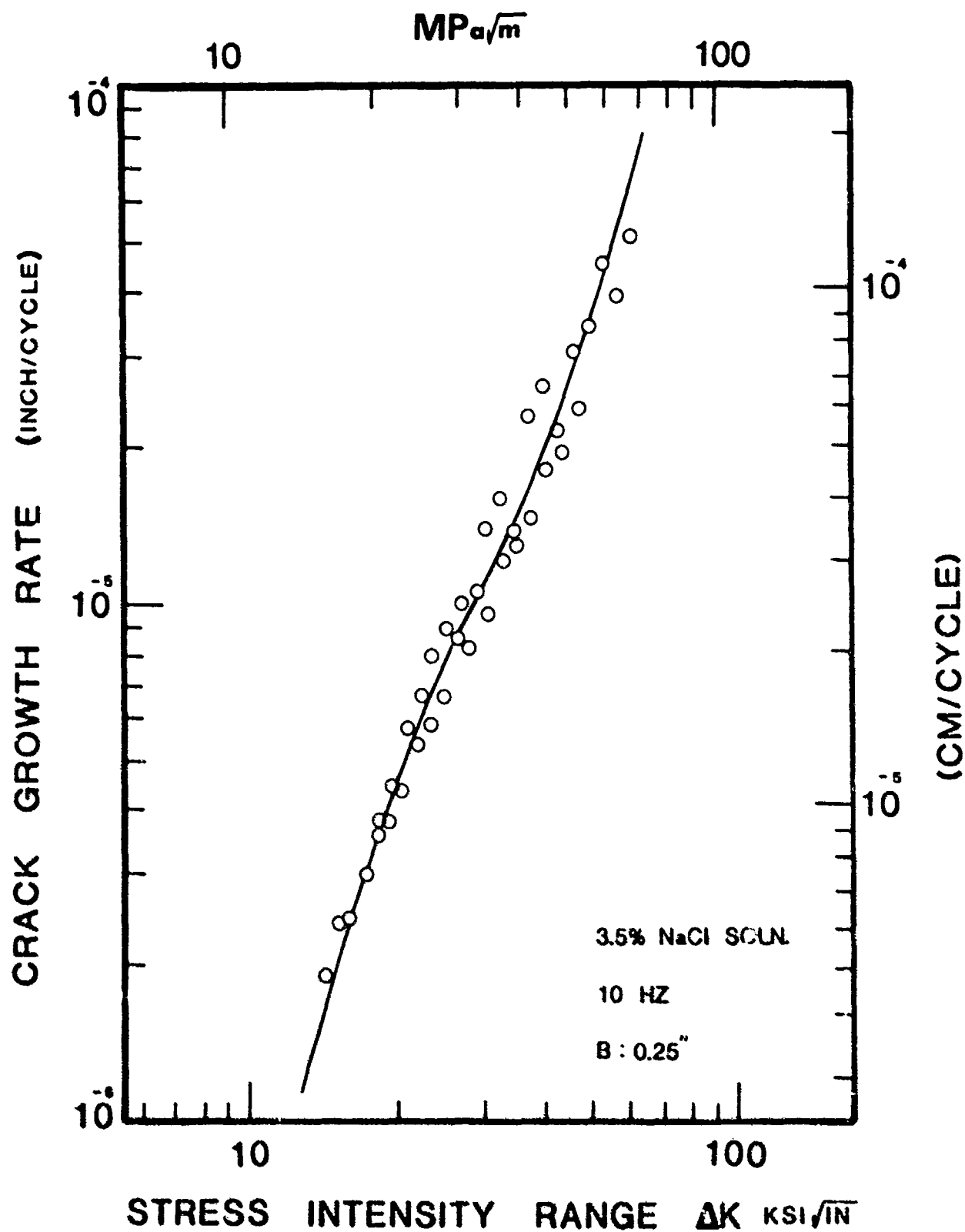


Fig. 22. FCP curve of AF-1410 steel aged at 950°F for 5 hrs. and tested in 3.5% NaCl solution. R = 0.1, SEN specimen.

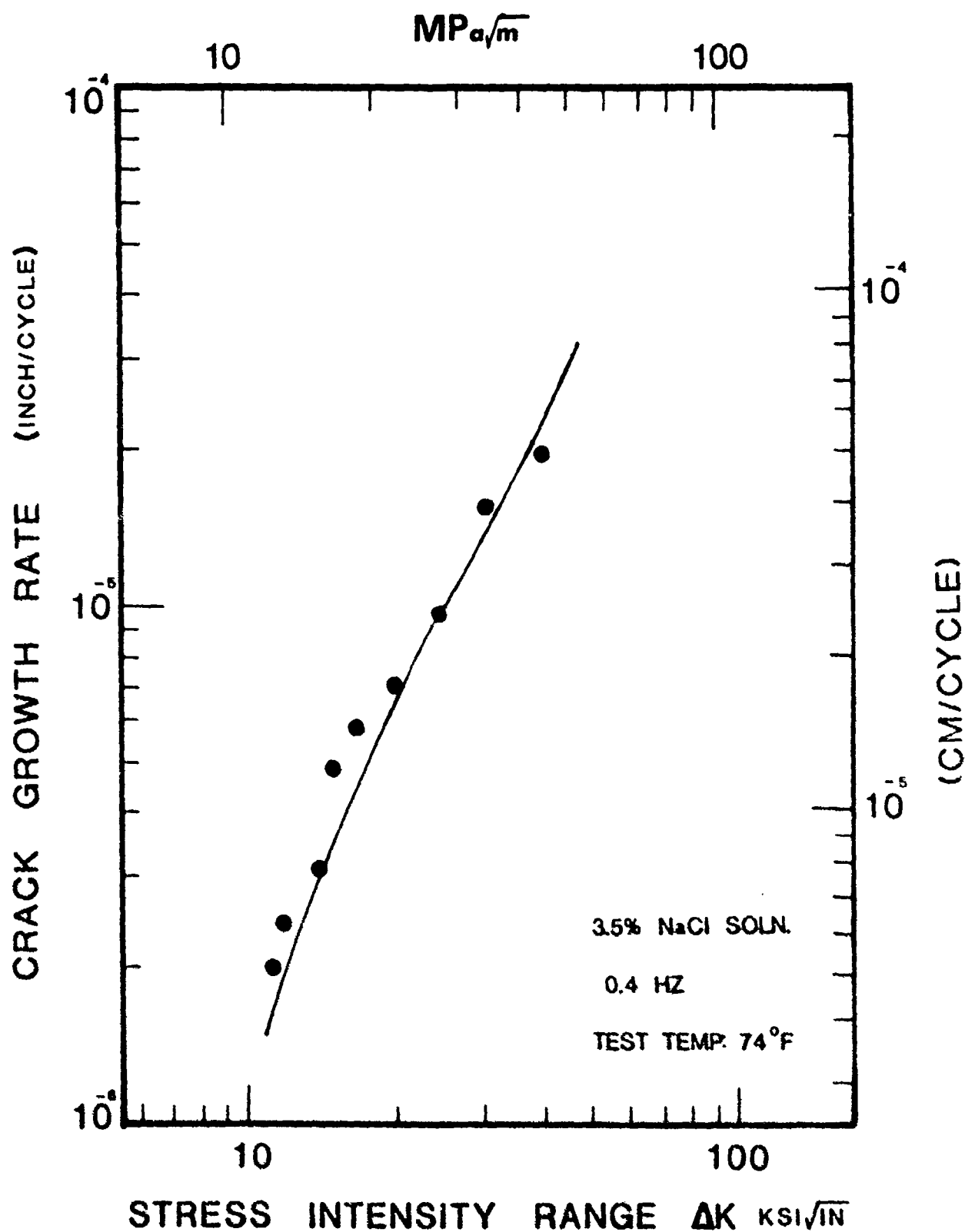


Fig. 23. FCP curve of AF-1410 steel aged at 950°F for 5 hrs., tested in 3.5% NaCl solution. $R = 0.1$, SEN specimen, $B = 0.08$ ".

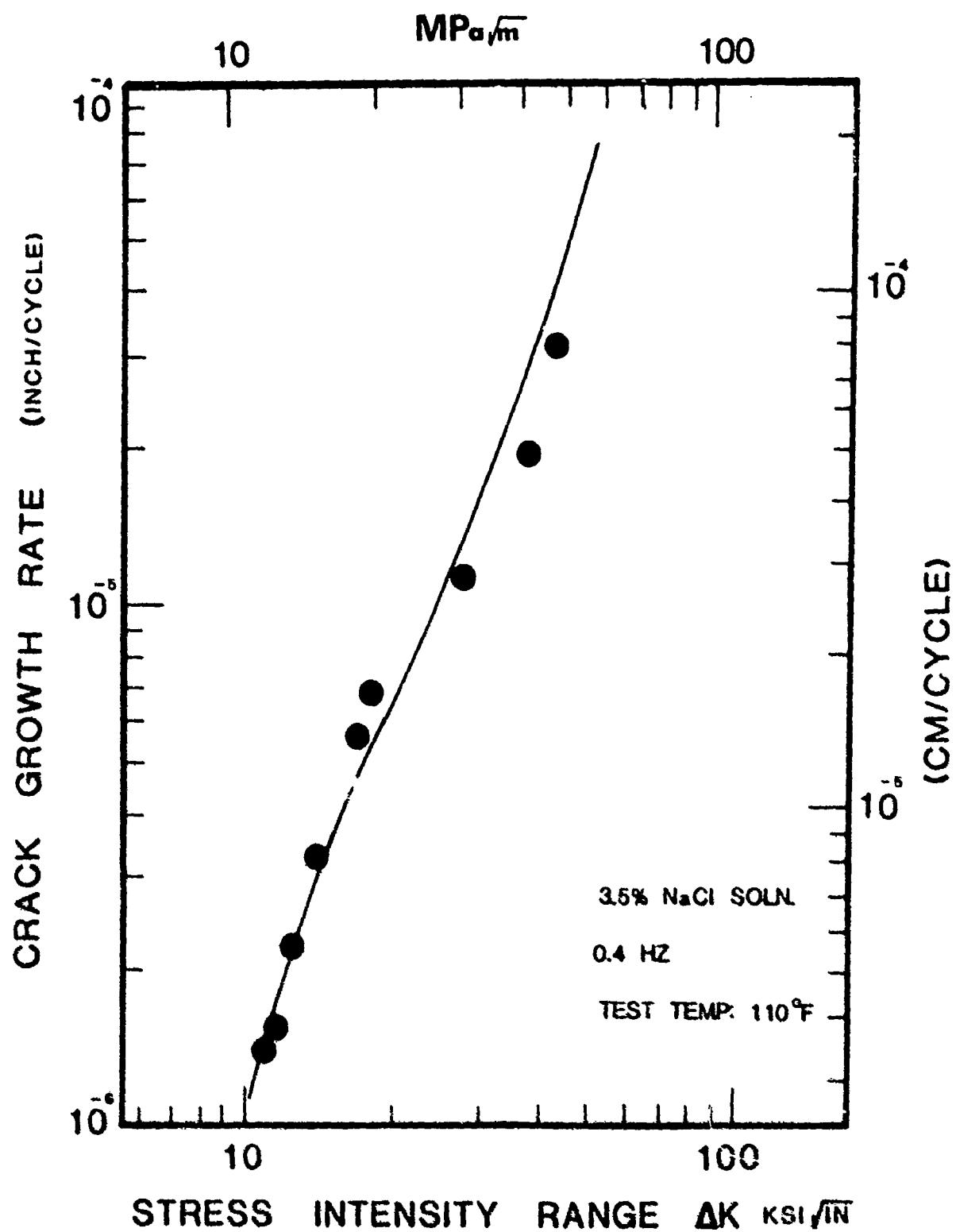


Fig. 24. FCP curve of AF-1410 steel aged at 950°F for 5 hrs., tested in 3.5% NaCl solution. R = 0.1, SEN specimen, B = 0.08".

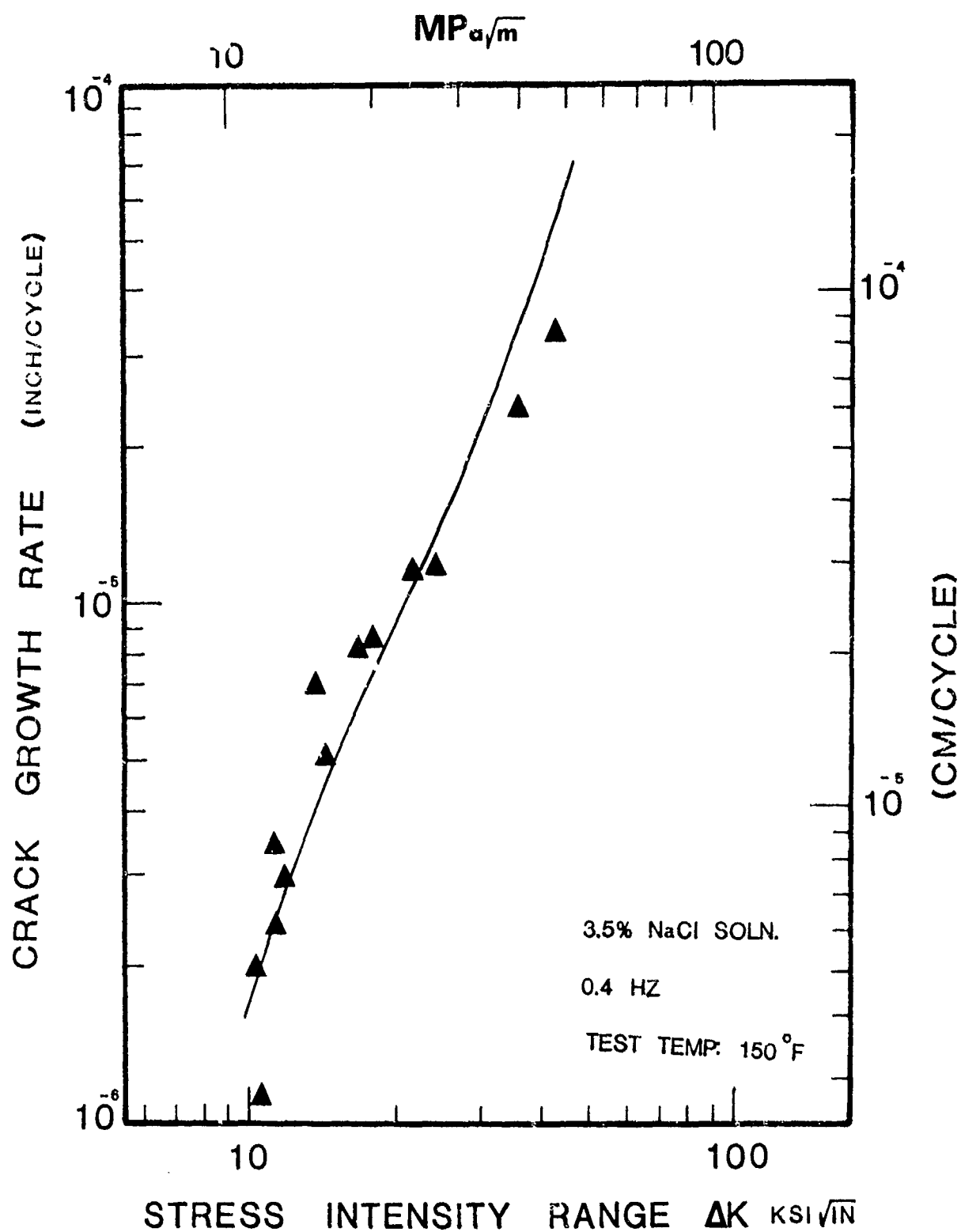


Fig. 25. FCP curve of AF-1410 steel aged at 950°F for 5 hrs., tested in 3.5% NaCl solution.
R = 0.1, SEN specimen, B = 0.08 .

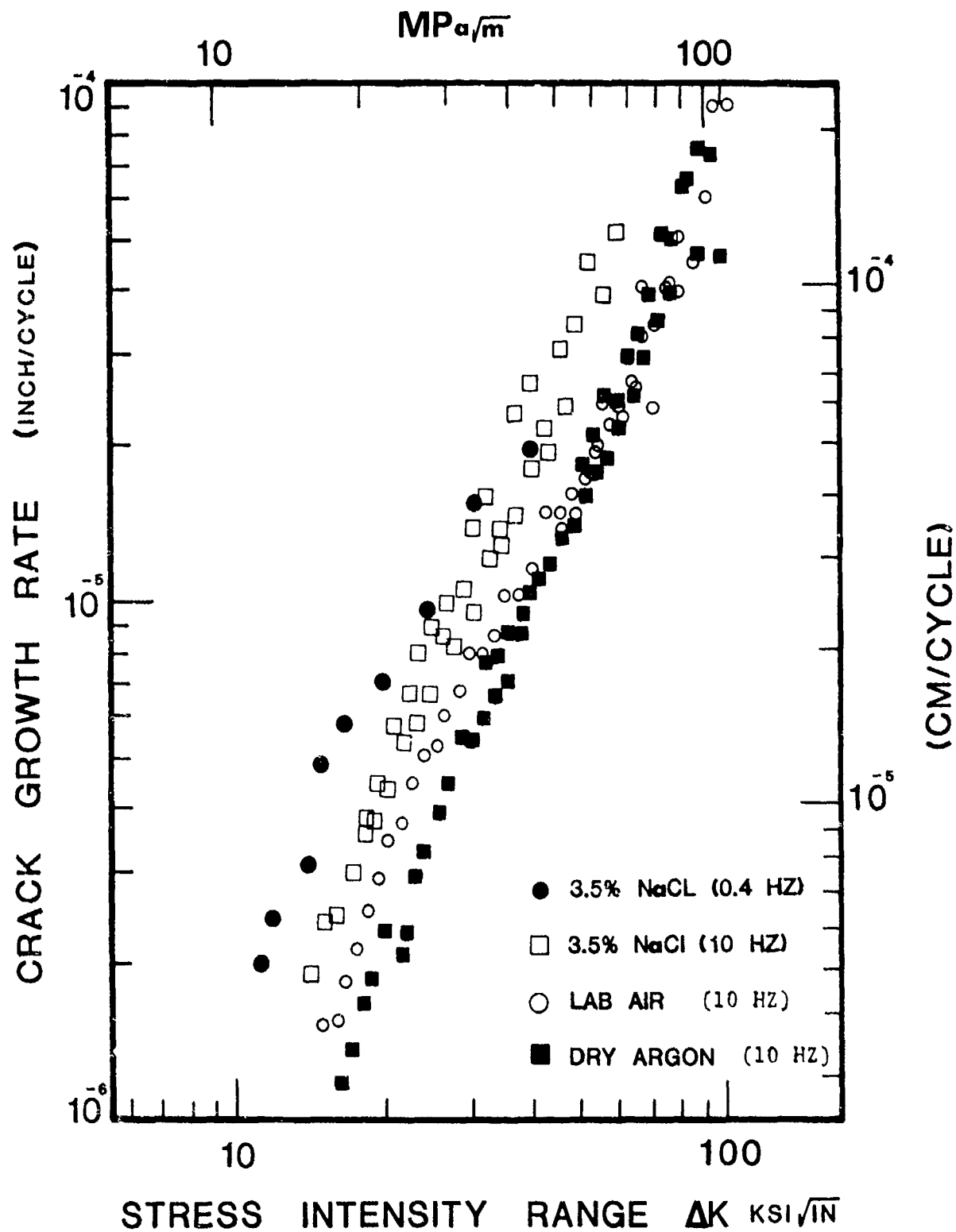
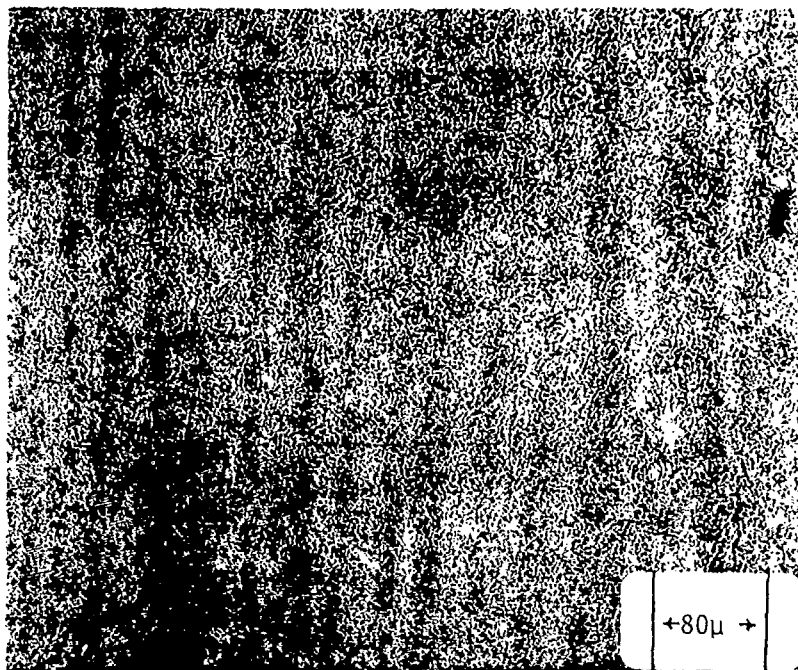


Fig. 26. Comparative fatigue crack growth rates of AF-1410 steel aged at 950°F for 5 hrs. Tested in different environments SEN specimens of 0.08" thickness were used at $R = 0.1$.

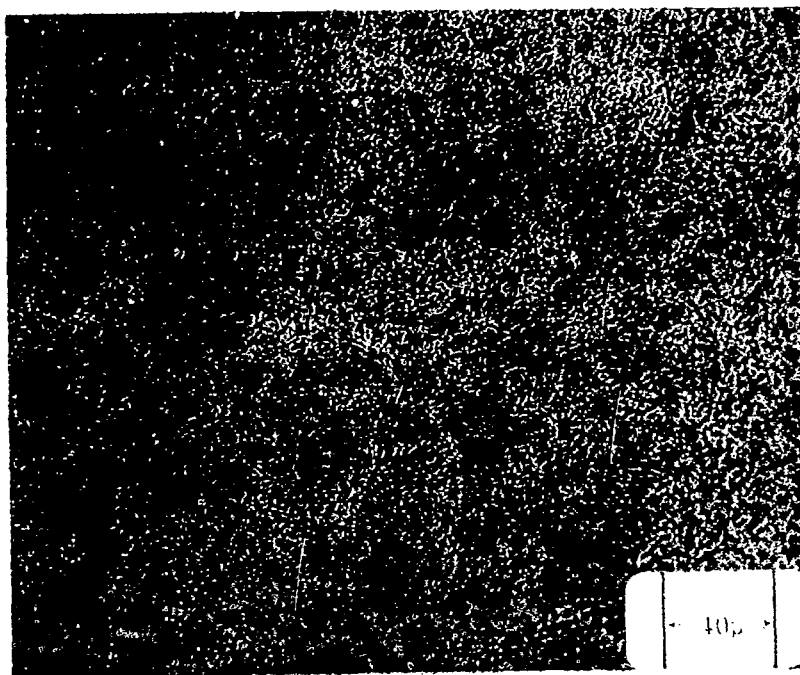


(a)

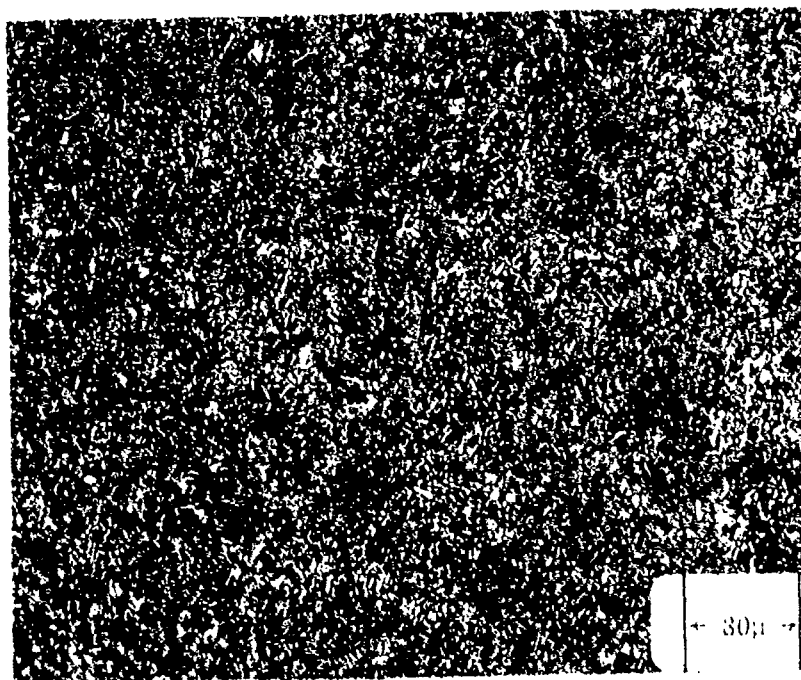


(b)

Fig. 27. Optical photomicrographs of A1-1410 steel
 (a) As-Quenced (annealed) microstructure. Note the banded structure.
 (b) 950°F/5 hrs. age microstructure. Grain size is ASTM # 16.



(c)



(d)

Fig. 27. (continued)

(c) Microstructure for the 750°F/5 hrs. age.

(d) Microstructure for the 975°F/5 hrs. age.

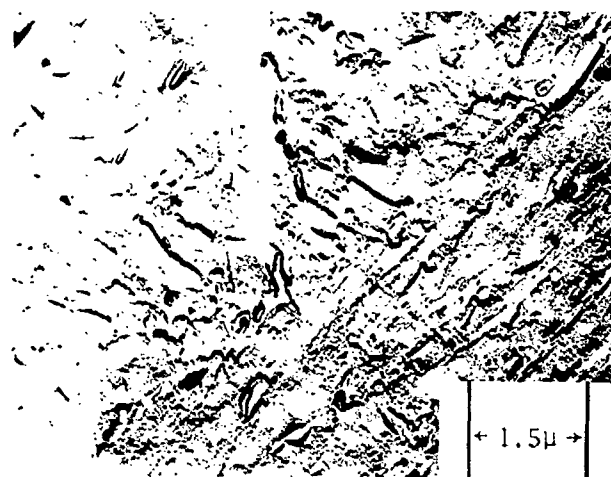


(a)

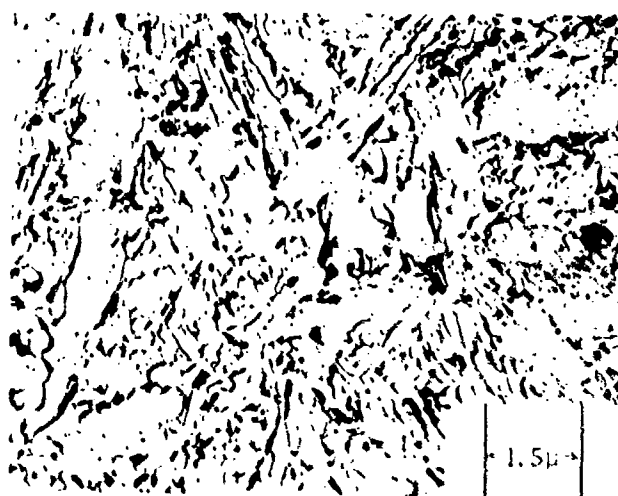


(b)

Fig. 28. Microstructure of AF 1410 steel as obtained by TEM replicas.
 (a) As-Quenched (annealed) micrograph showing the large carbides and plate shaped martensite laths.
 (b) 950°F/5 hrs. age. Fine $(\text{MoCr})_2\text{C}$ precipitates are seen.



(c)



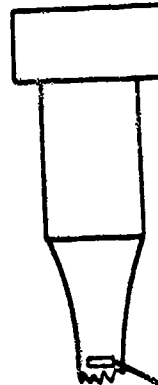
(d)

Fig. 28. (continued).

(c) 750°F/5 hrs. age microstructure. Precipitates are larger than the 950°F age.

(d) 975°F/5 hrs. age microstructure.

STRESS AXIS

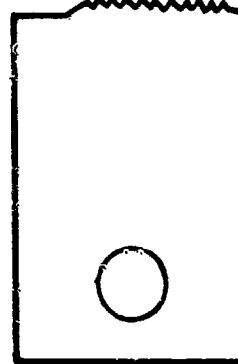


ORIENTATION OF
TEM FOIL

(a)

FRACTURED SURFACE
FOR SEM ANALYSIS

STRESS AXIS



(b)

Fig. 29. (a) Orientation of TEM foils in fractured LCF specimens
(b) Fracture surface for SFM analysis relative to the stress axis in SEN and CT specimens.

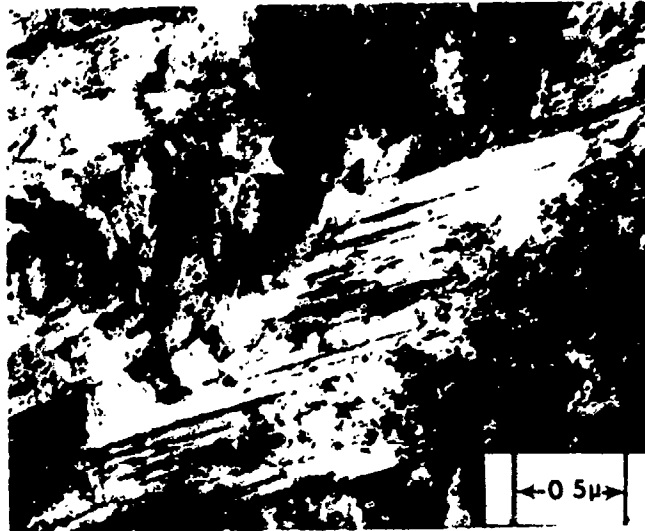
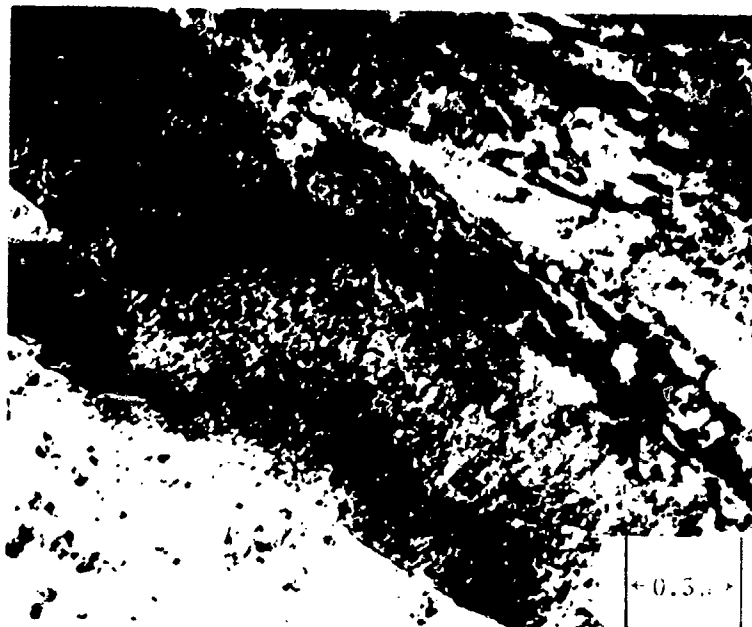
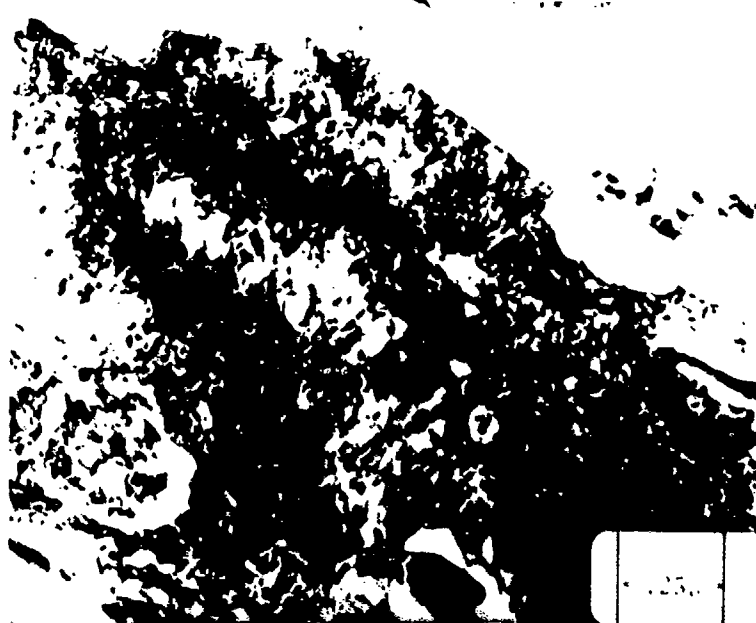


Fig. 30. TEM micrograph of the as-quenched annealed substructure showing the dislocated martensitic structure and needle shaped twins.



(a)

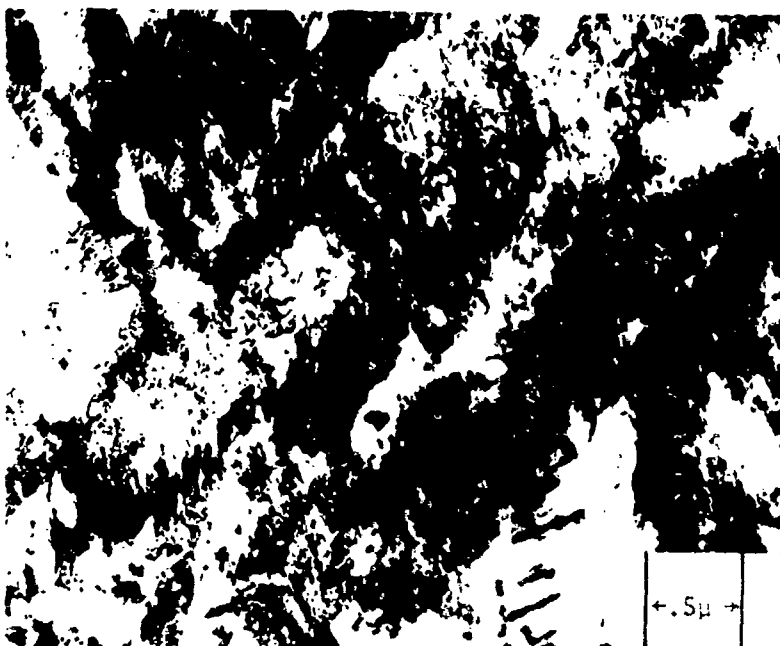


(b)

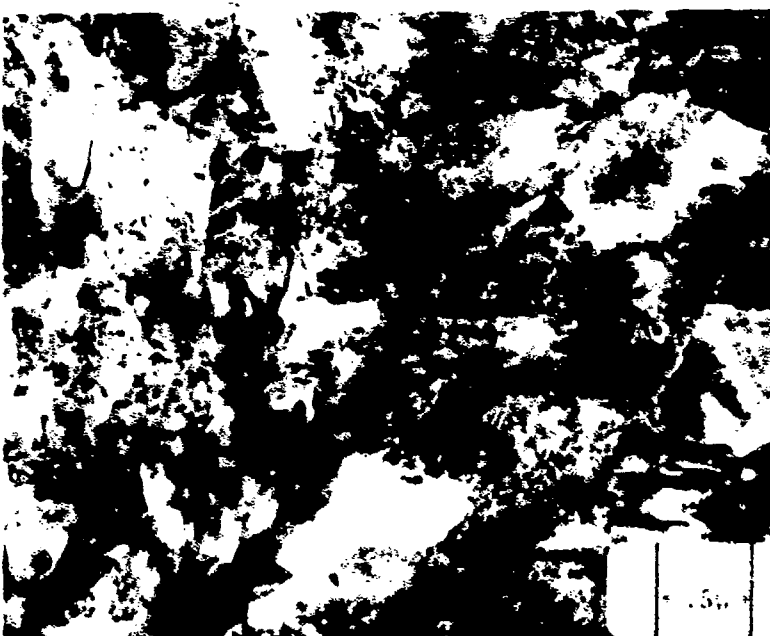
Fig. 31. TEM micrograph of the 950°F/5 hrs. ageing treatment, obtained using two beam diffracting conditions. Note the highly dislocated lath martensitic structure. Retained austenite is seen around lath boundaries and fine precipitates appear in the lath interiors apparently nucleated on dislocations.



Fig. 32. Undeformed structure of the 975°F/5 hrs. ageing treatment. Fine precipitates within and at lath boundaries are seen. Retained austenite is also present in lath boundaries.

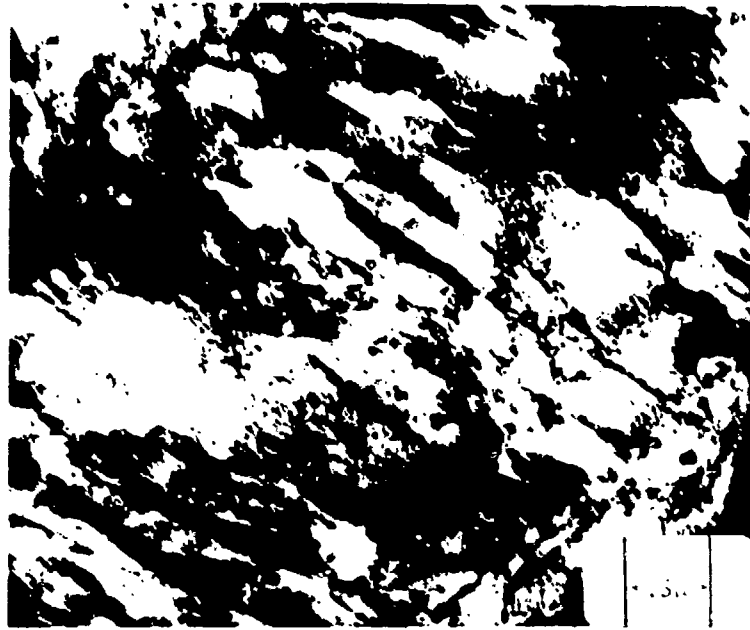


(a)



(b)

Fig. 33. Undeformed structure of the 750°F/5 hrs. ageing treatment. Carbides are much larger than were seen in the 950°F age. Internal twins and plate shaped Fe_3C precipitates are also visible.

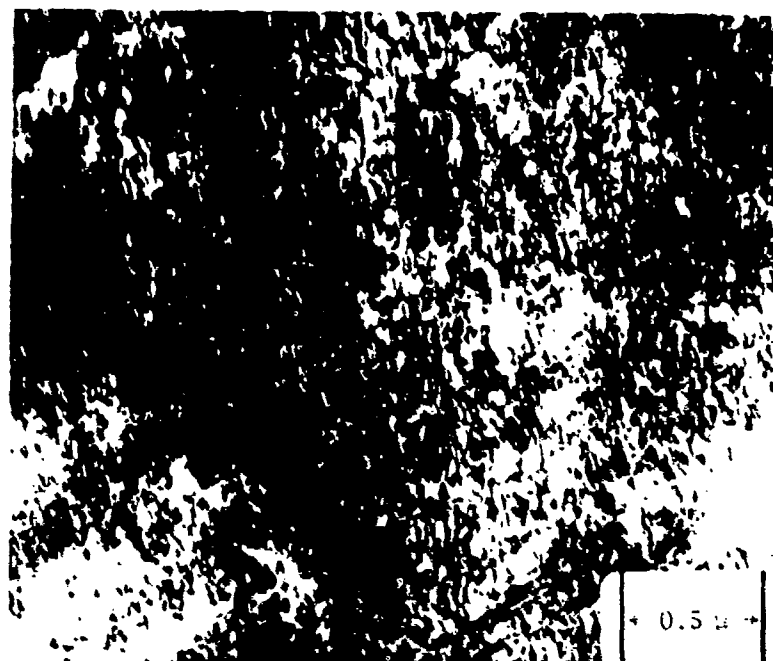


(a)



(b)

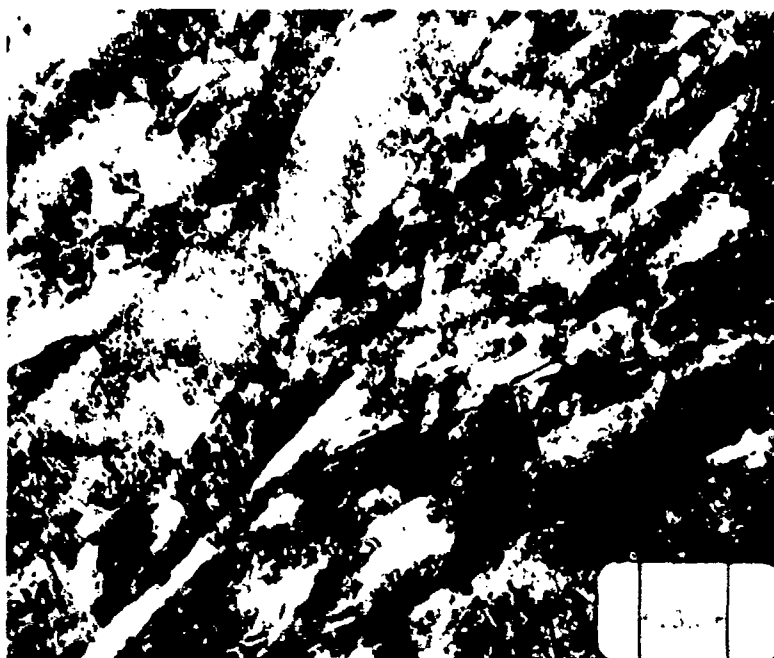
Fig. 34. TEM micrographs of 950°F age LCF specimen tested at $\Delta\epsilon_p = 0.8\%$ ($N_f = 400$ cycles). (a & b) Dislocations are rearranged into quasi cells as compared to the undeformed structure. No slip bands are seen. Microtwins appear inside martensite laths are seen in (b).



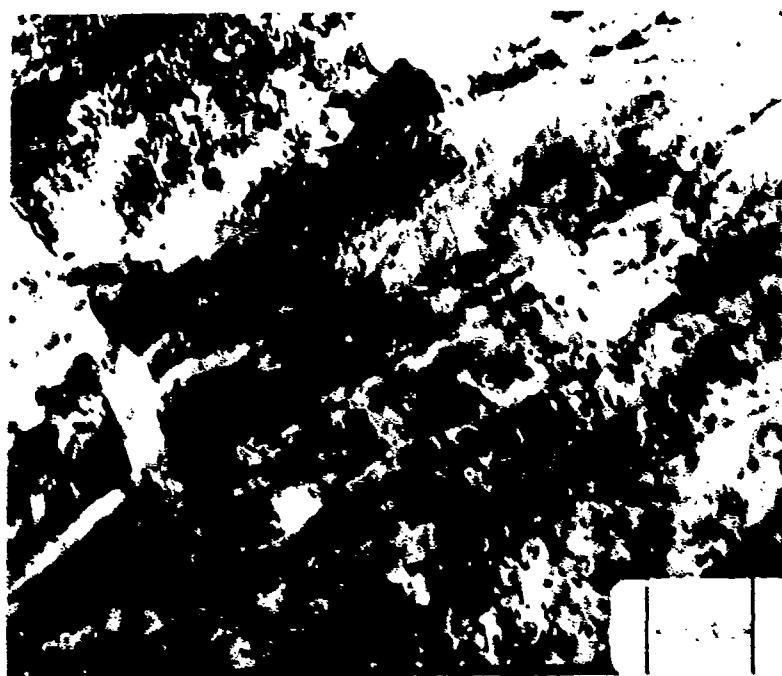
(c)

Fig. 34 (continued)

(c) Martensite lath containing extremely high dislocation density.

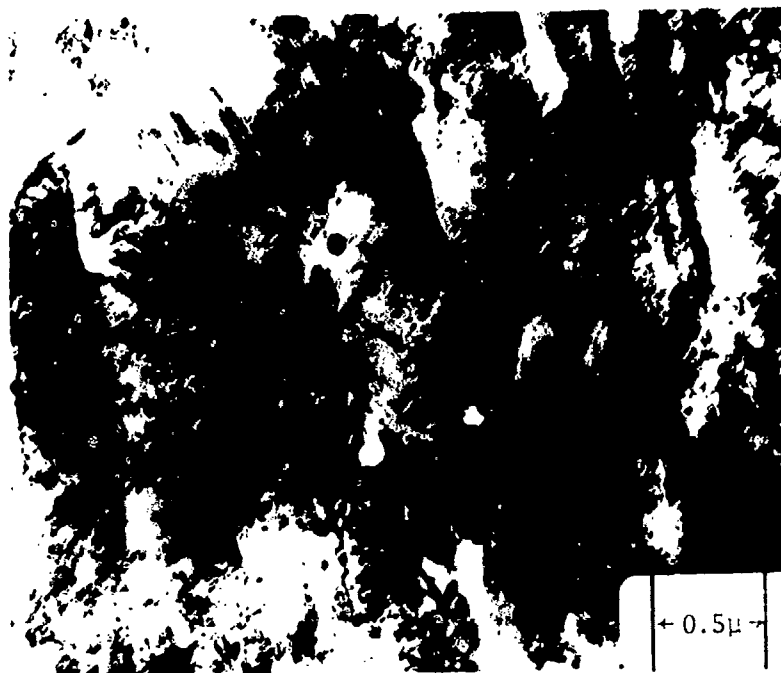


(a)



(b)

Fig. 35. Substructure of 950°F age LCF specimen tested at $\Delta\epsilon_p' = 0.03\%$ ($N_f = 5000$ cycles). No slip bands are seen and dislocations appear rearranged into quasi cells.

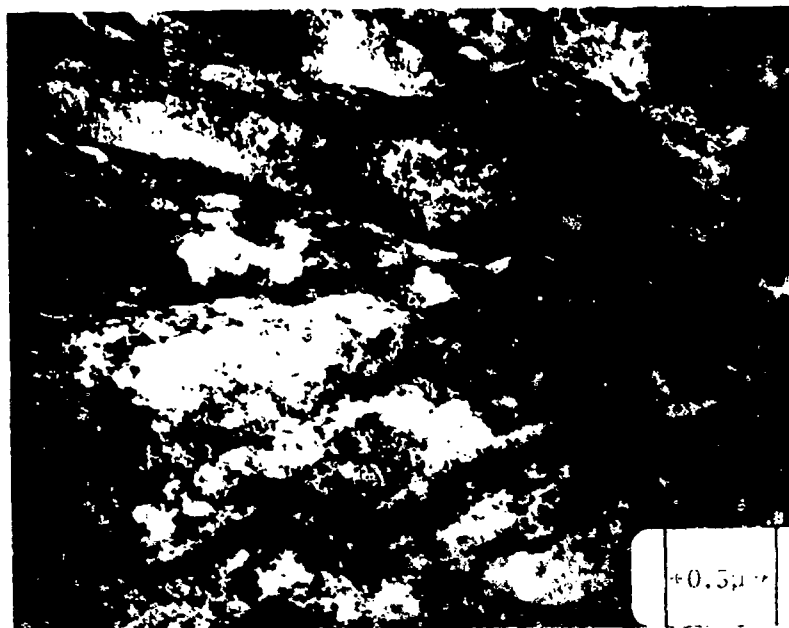


(a)

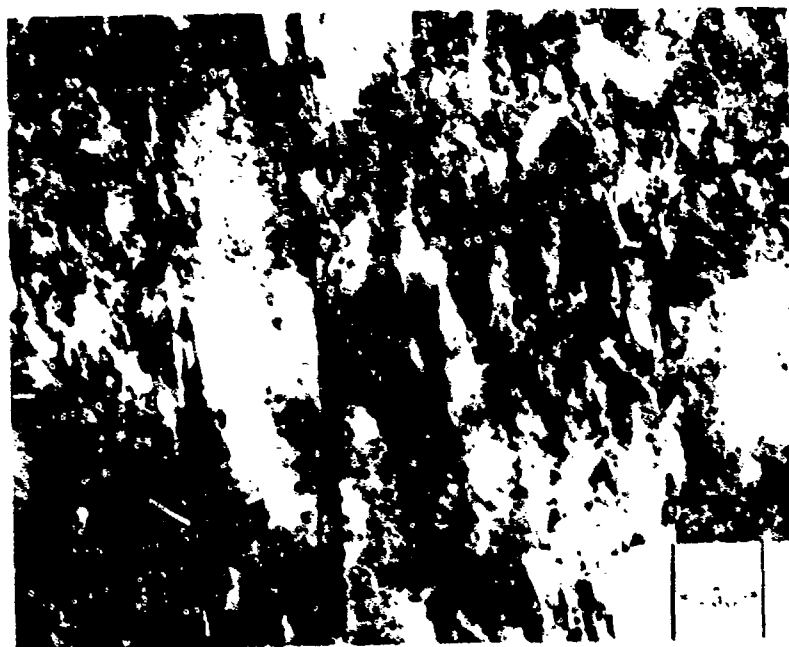


(b)

Fig. 36. TEM micrographs of 750°F age LCF specimen tested at $\Delta c_P^L = 0.14\%$. Some thin elongated twins are seen inside martensite laths along with plate shaped Fe_3C which is always located within laths.

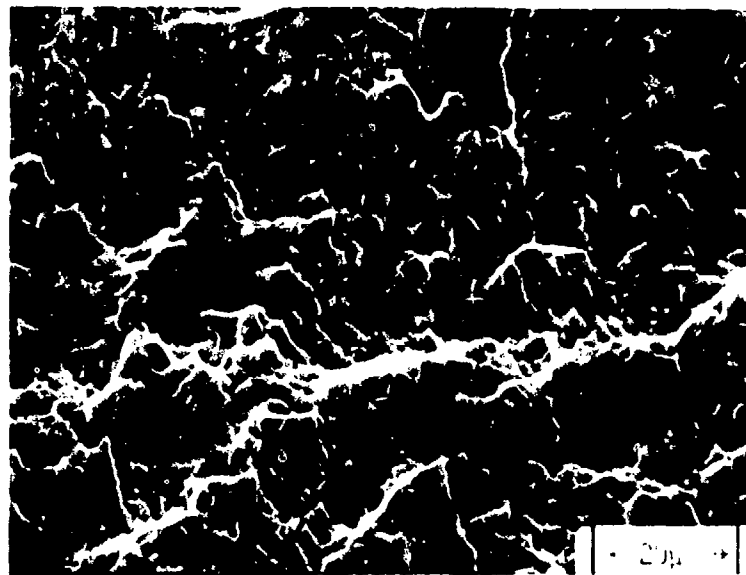


(a)

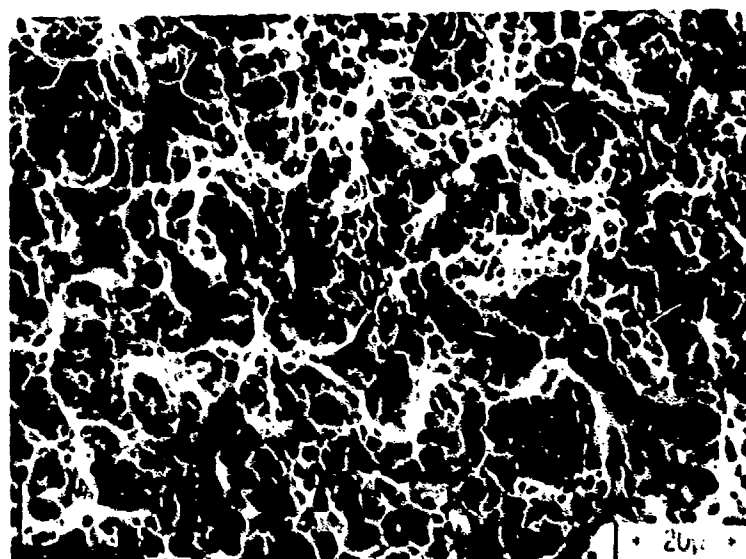


(b)

Fig. 37. TEM micrographs of 975°F age LCF specimen tested at $\Delta\epsilon_p^k = 0.14\%$. Precipitation appears along the lath boundaries in (a). A quasi cell structure appears to be developing in (b).

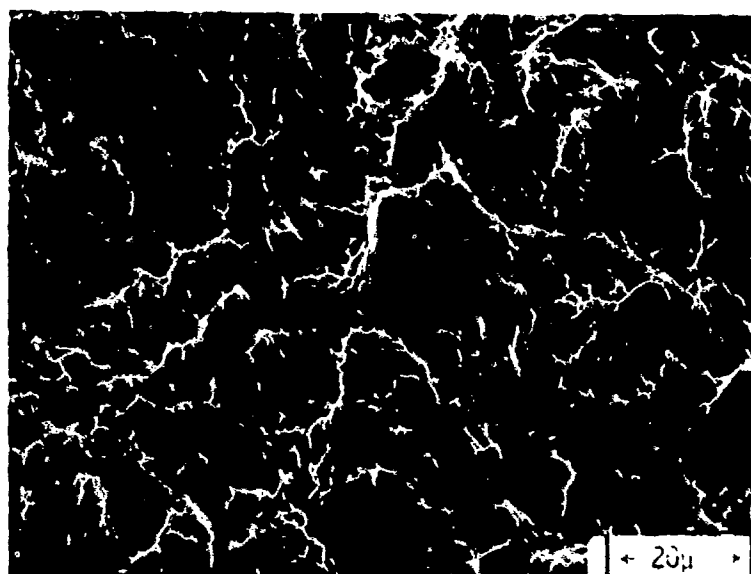


(a)



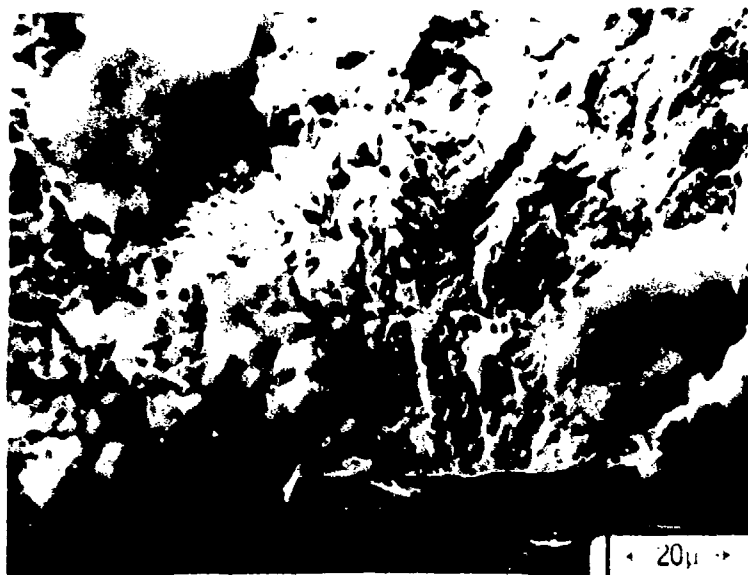
(b)

Fig. 38 - See following page for caption.

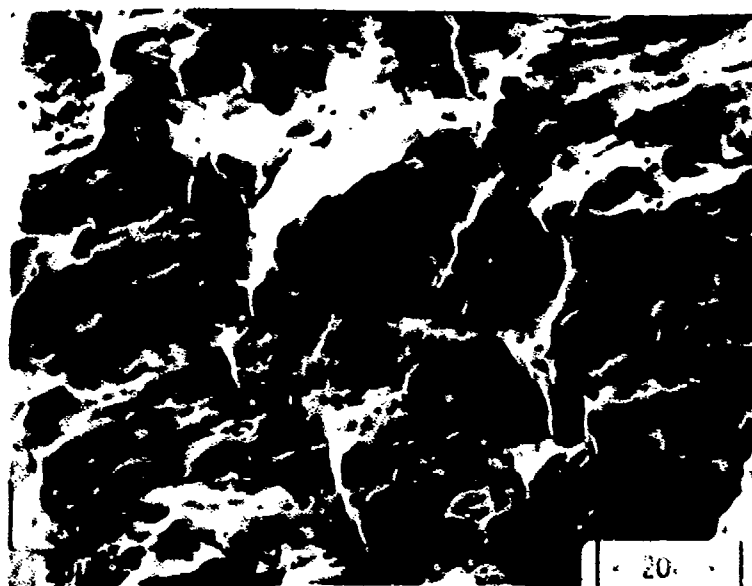


(c)

Fig. 38. SEM micrographs of the fracture surface of annealed LCF specimens. In (a) the origin of a low strain specimen is shown, while (b) is the overload region of the same specimen. In (c) the origin region of a high strain specimen is shown.

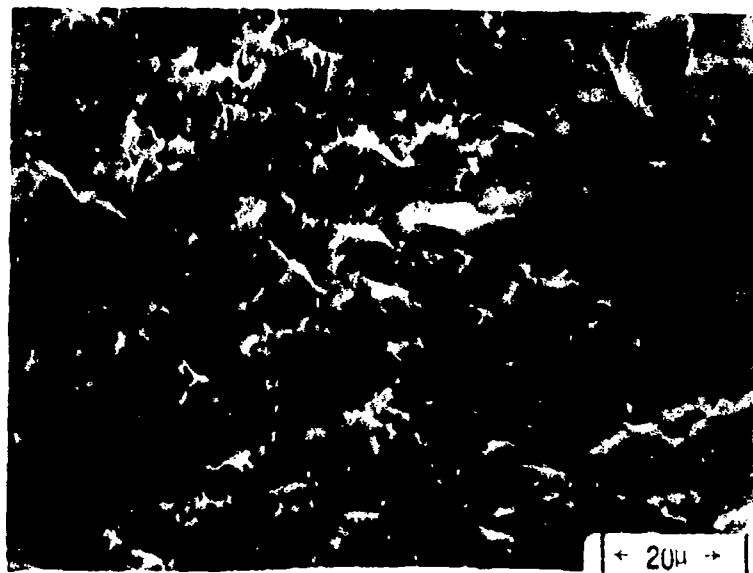


(a)

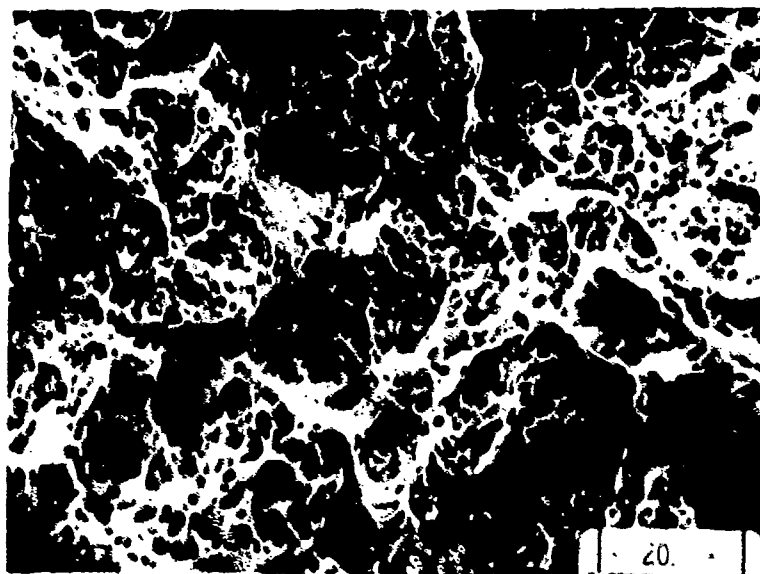


(b)

Fig. 39 - See following page for caption.



(c)



(d)

Fig. 39. SEM micrographs of the fracture surface of 950°F/5h aged LCF specimens. In (a) and (b) the origin and near-origin regions of a low strain specimen are shown while in (c) and (d) the near origin and overload regions of a high strain specimen are shown.

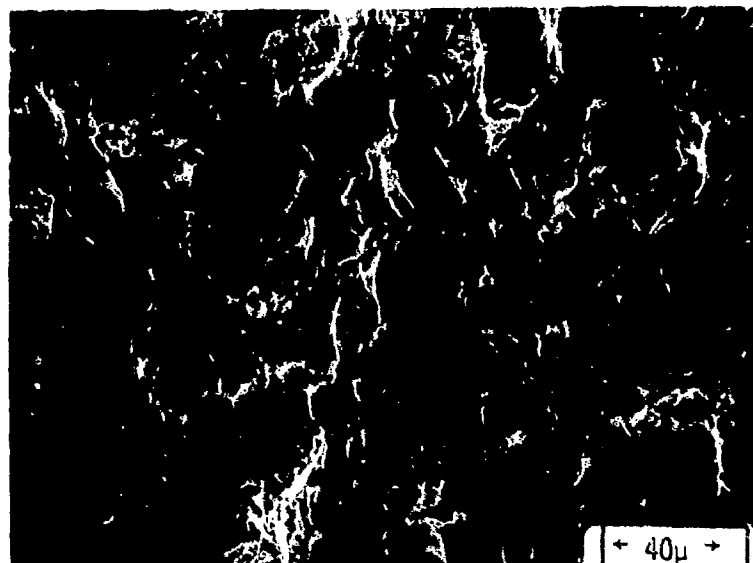


Fig. 40. SEM micrograph of LCF specimen aged at 750°F. The photograph was taken in the near-origin region.

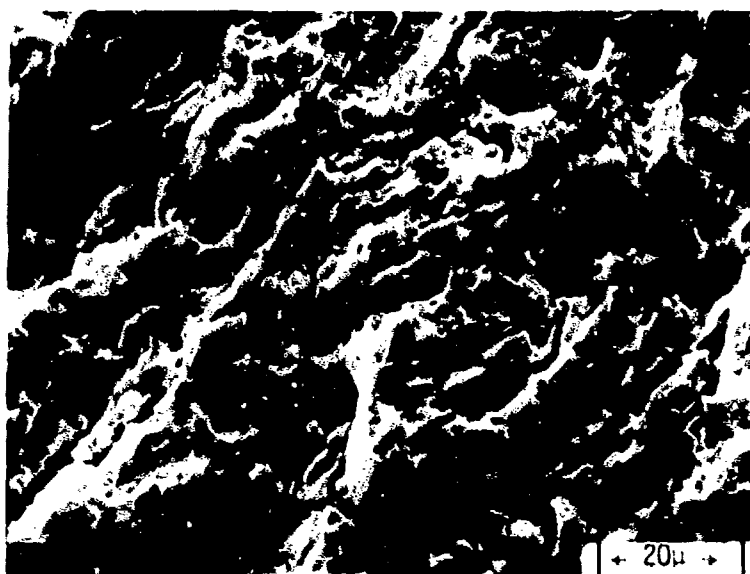
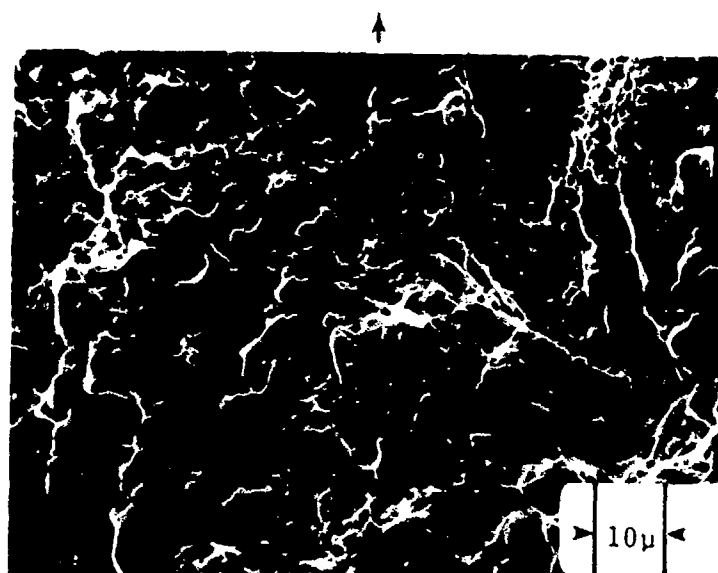
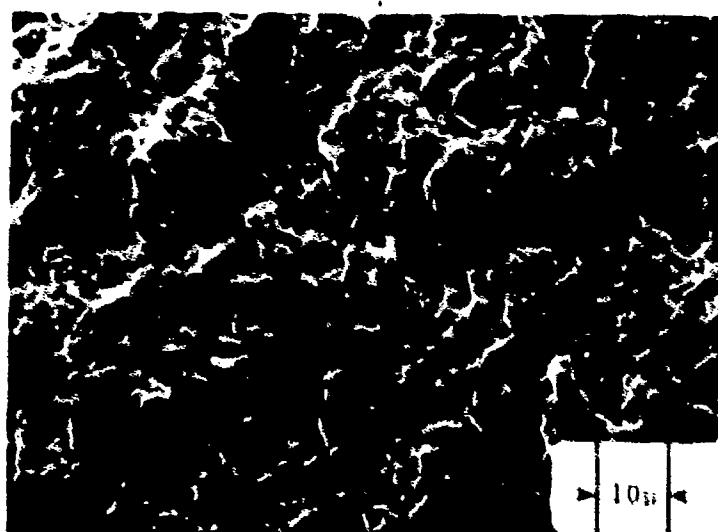


Fig. 41. SEM micrograph of fracture surface of LCF specimen that was aged at 975°F. The photo was taken in the near-origin region.



$\Delta K = 25 \text{ ksi}/\text{in}$

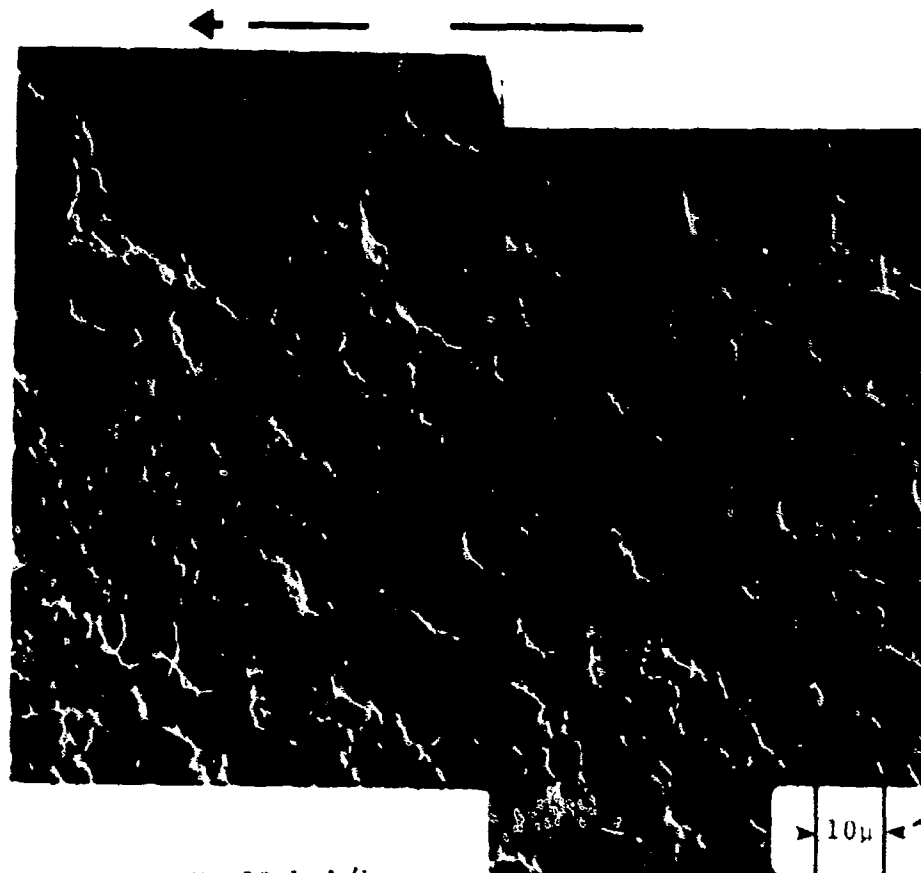
(a)



$\Delta K = 30 \text{ ksi}/\text{in}$

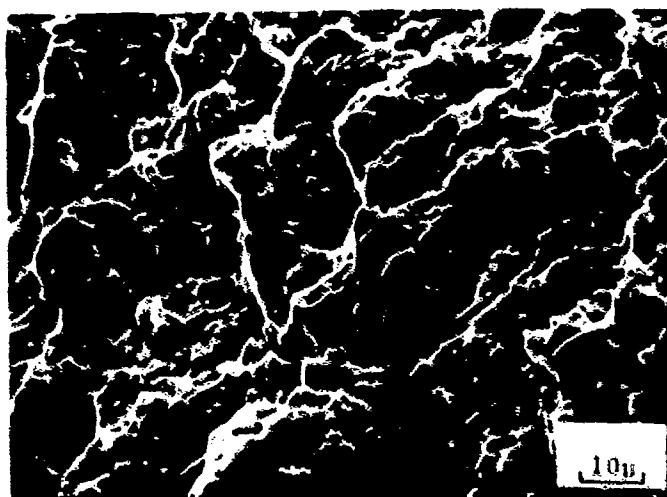
(b)

Fig. 42. SEM fractographs of 950°F for 5 hr. age FCP specimens. Stress intensity levels are indicated on each fractograph. The arrow marks the crack propagation direction. a&b are for low ΔK levels and exhibit a generally transgranular mode. Extensive branch cracking (marked A) is obvious. Note the dimples in the upper right hand corner of (a) indicative of localized normal rupture.



$\Delta K = 50 \text{ ksi}/\text{in}$

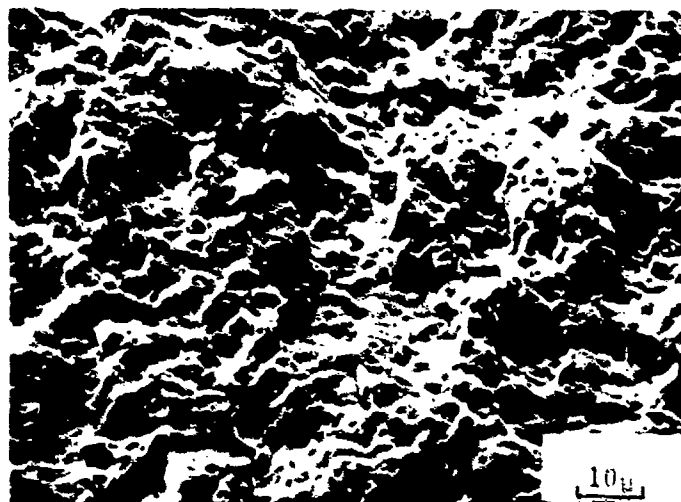
(a)



$\Delta K = 50 \text{ ksi}/\text{in}$

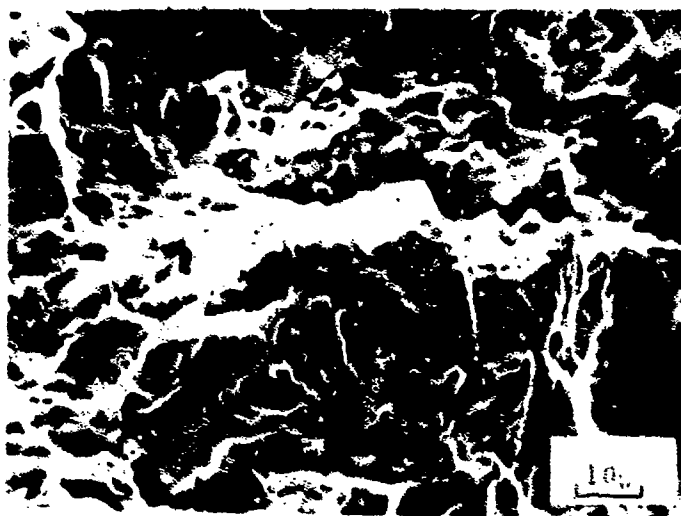
(b)

Fig. 43. SEM fractographs for 950°F for 5 hr. aged material at intermediate stress intensities.
 (a) Stereo-pair showing large branch cracks.
 (b) Small dimples indicating localized normal rupture.



$\Delta K = 70 \text{ ksi}\sqrt{\text{in}}$

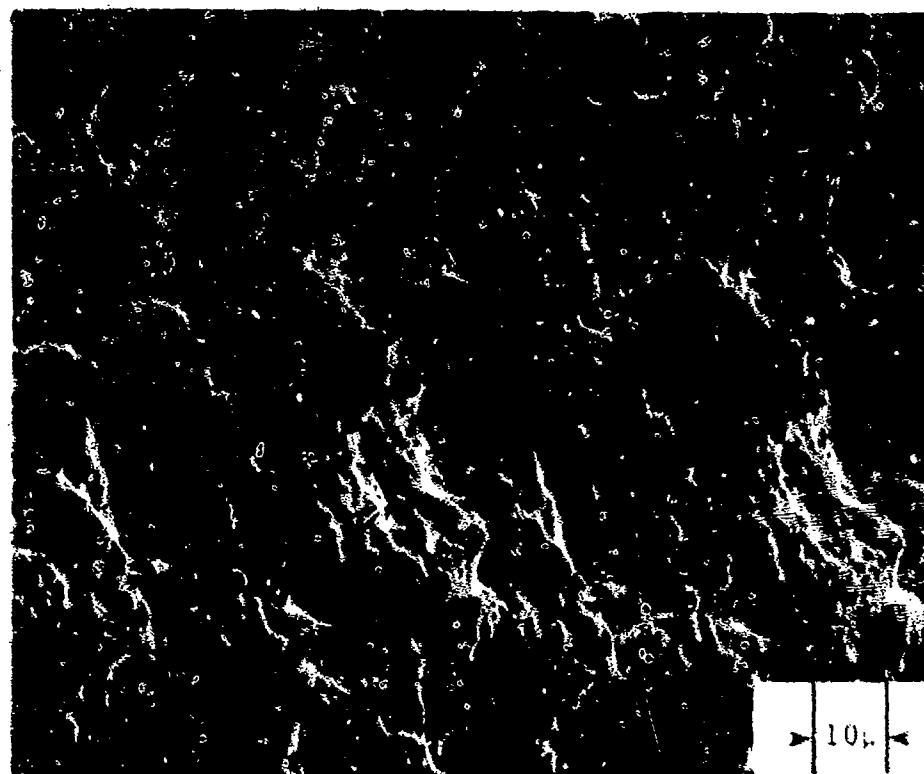
(a)



$\Delta K = 75 \text{ ksi}\sqrt{\text{in}}$

(b)

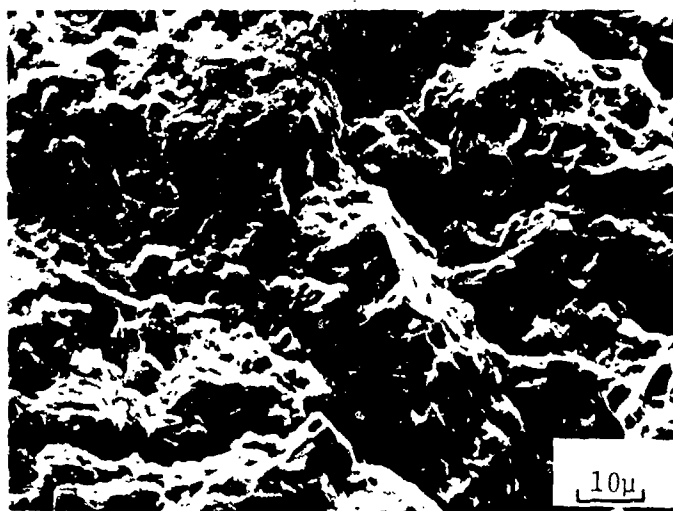
Fig. 44. SEM fractographs for 950°F for 5 hr. aged material at intermediate stress intensities.
 (a) Fracture surface is rough and dimpling is more pronounced. This fractograph was taken from a test run in lab air.
 (b) Striations, marked B, are clearly seen. FCP rate computed from these striation spacings is 4.33×10^{-5} inch/cycle as compared to the experimental rate of 3.5×10^{-5} inch/cycle. Tested in dry argon.



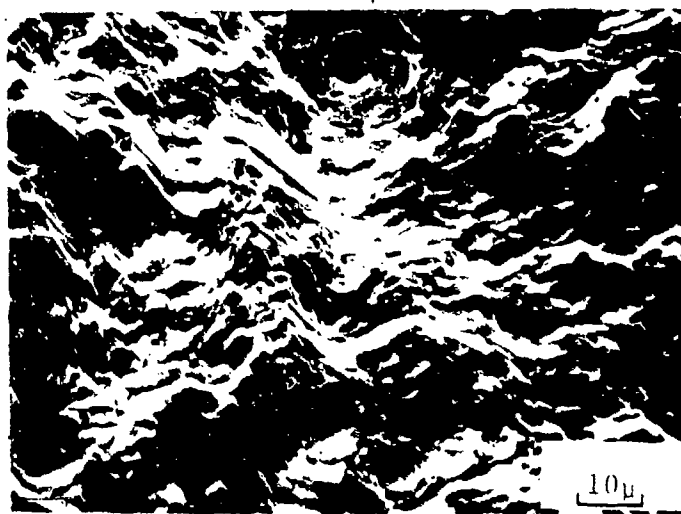
$\Delta K = 90 \text{ ksi}/\text{in}$

(a)

Fig. 45. SEM fractographs for 950°F for 5 hr. aged material at intermediate stress intensities.
 (a) Stereo-pair at a high stress intensity level. Fracture surface is rough and branch cracks are much larger than before. Again cracking is transgranular.



$\Delta K = 90 \text{ ksi/in}$
(b)



$\Delta K = 110 \text{ ksi/in}$
(c)

Fig. 45 (continued).
(b) Tensile overload region showing large dimples, indicative of normal rupture and brittle striations (marked C).
(c) Brittle striations and branch cracks.

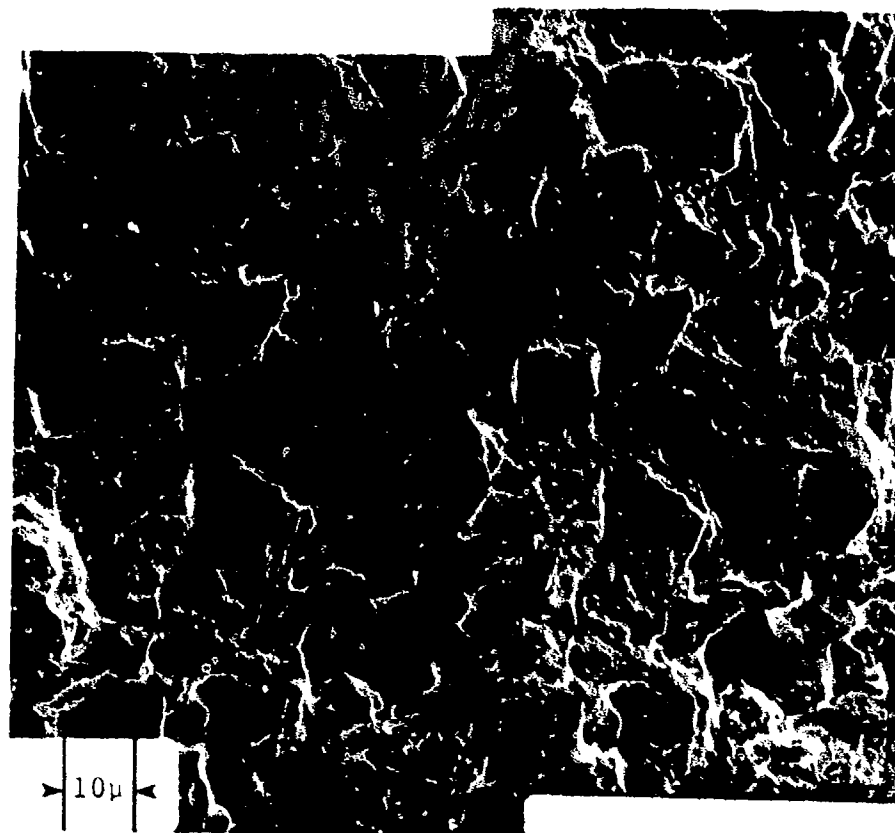
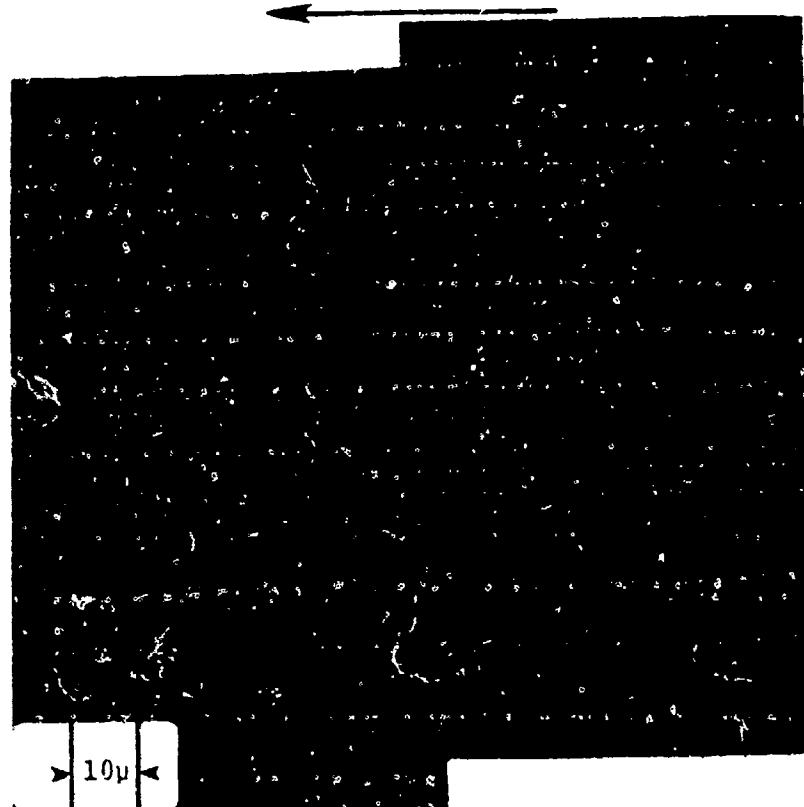


Fig. 46. SEM fractographs of 750°F for 5 hr. age FCP specimens. Stress intensity levels indicated on the fractographs.
(a) Stereo-pair at low stress intensity level. Extensive carbide cleavage is obvious. No striations or branch cracking is seen.

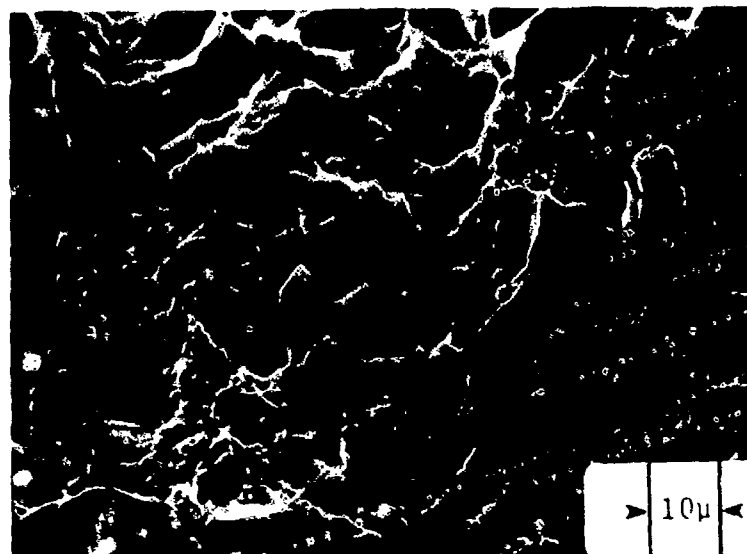


$\Delta K = 25 \text{ ksi}/\text{in}$

(b)

Fig. 46 (continued)

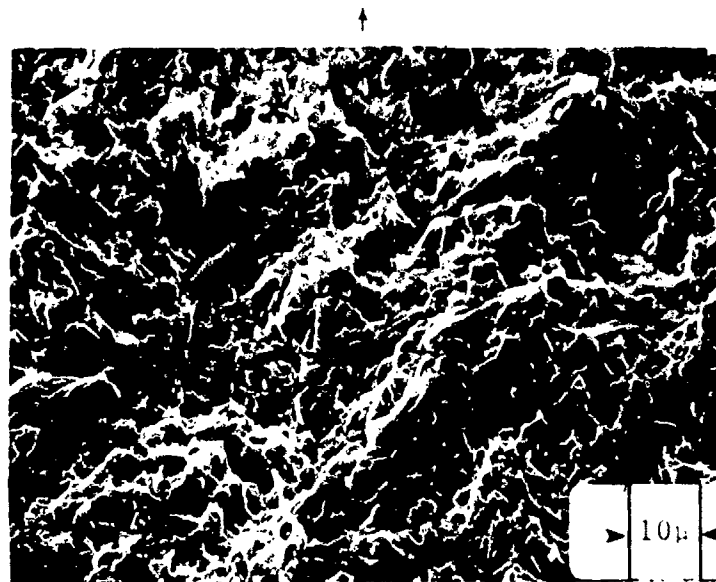
(b) Stereo-pair at slightly higher ΔK .



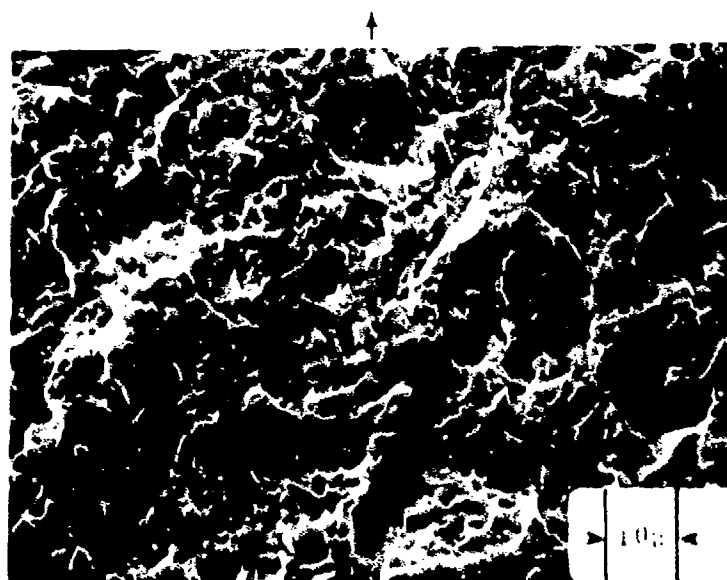
$\Delta K = 50 \text{ ksi}/\text{in}$

(a)

Fig. 47. SEM fractograph of material aged at 750°F for 5 h. and tested at intermediate ΔK levels. In (a) extensive cleavage of carbides is seen along with some fine dimples.

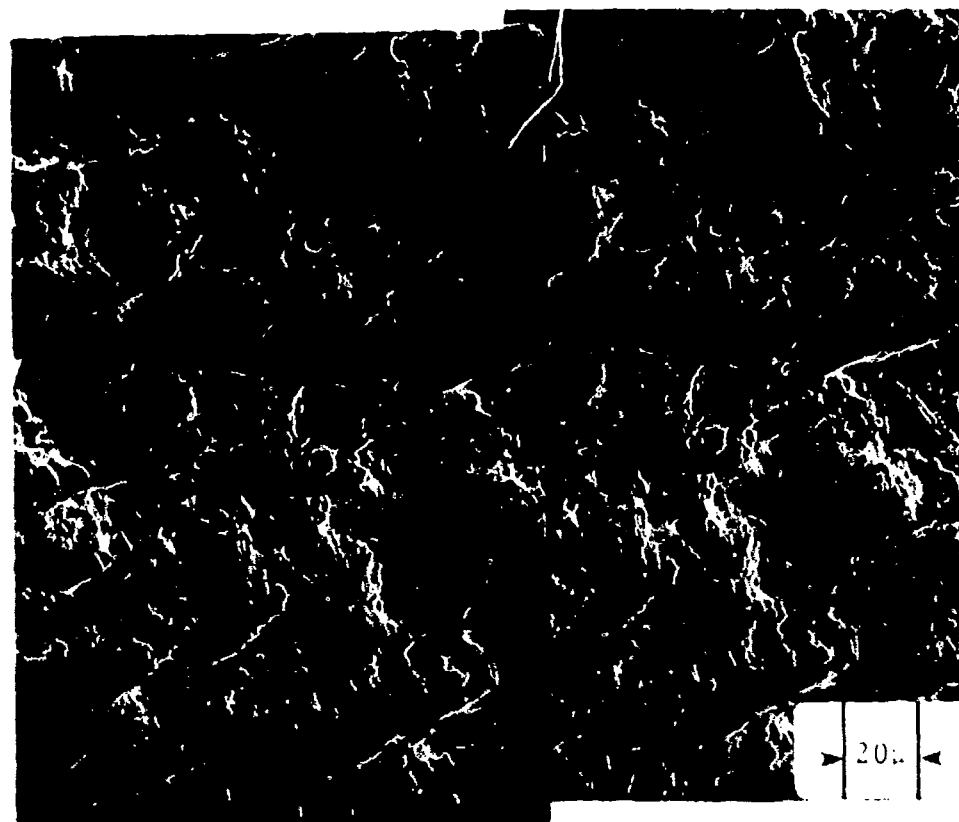


$\Delta K = 20 \text{ ksi}\sqrt{\text{in}}$
(a)



$\Delta K = 30 \text{ ksi}\sqrt{\text{in}}$
(b)

Fig. 48. SEM fractographs of 975°F for 5 hr. age FCP specimens. Stress intensity levels are indicated on each fractograph. Arrows indicate the crack propagation direction.
In (a) and (b) branch cracking and a few areas of carbide cleavage are visible. Cracking appears to be transgranular.



$\Delta K = 60 \text{ ksi}/\text{in}$

(c)

Fig. 48 (continued)
(c) Stereo-pair showing rough fracture surface and extensive branch cracking.

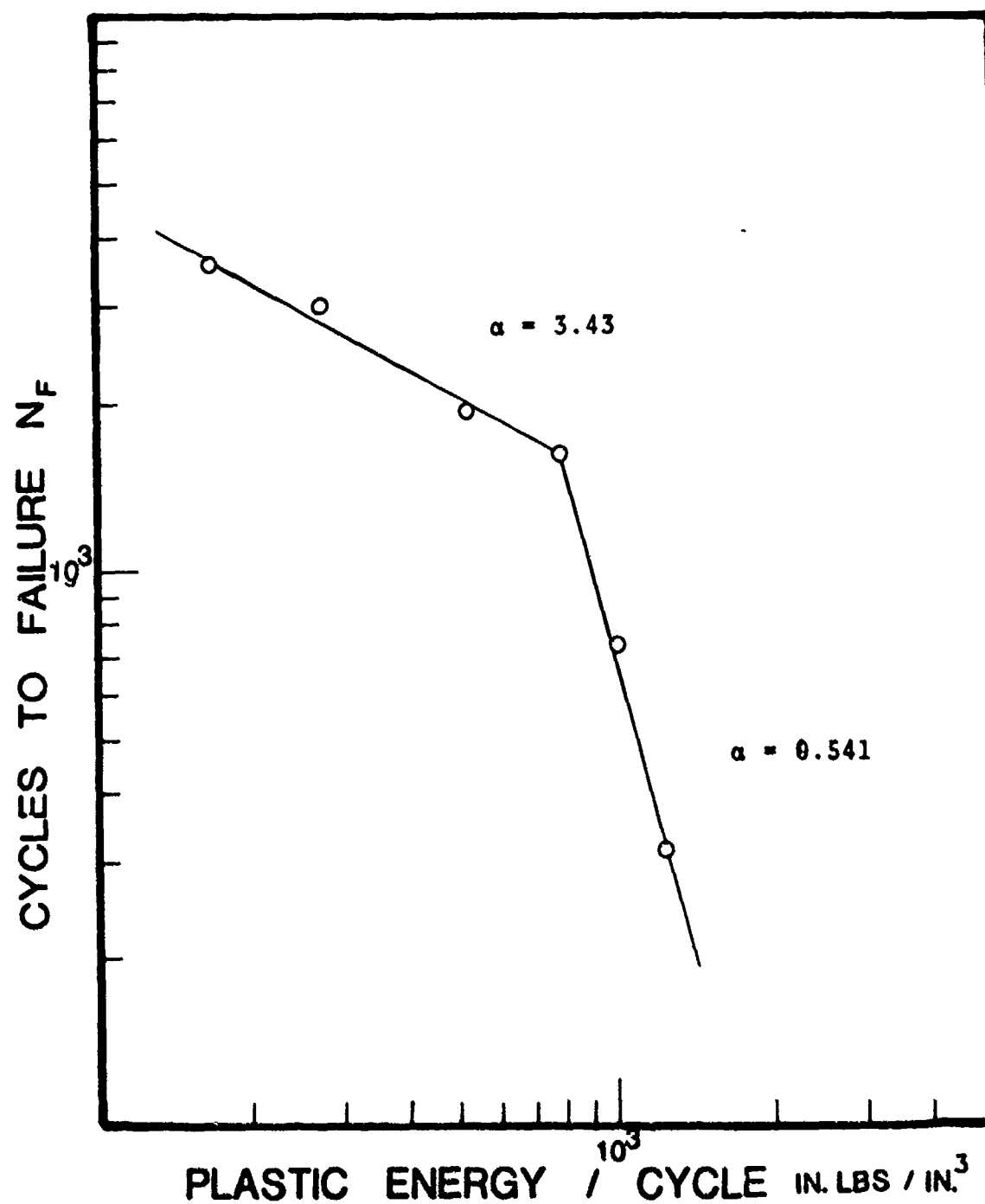


Fig. 49. Cycles to failure vs. plastic work/cycle for AF 1410 in the annealed condition.

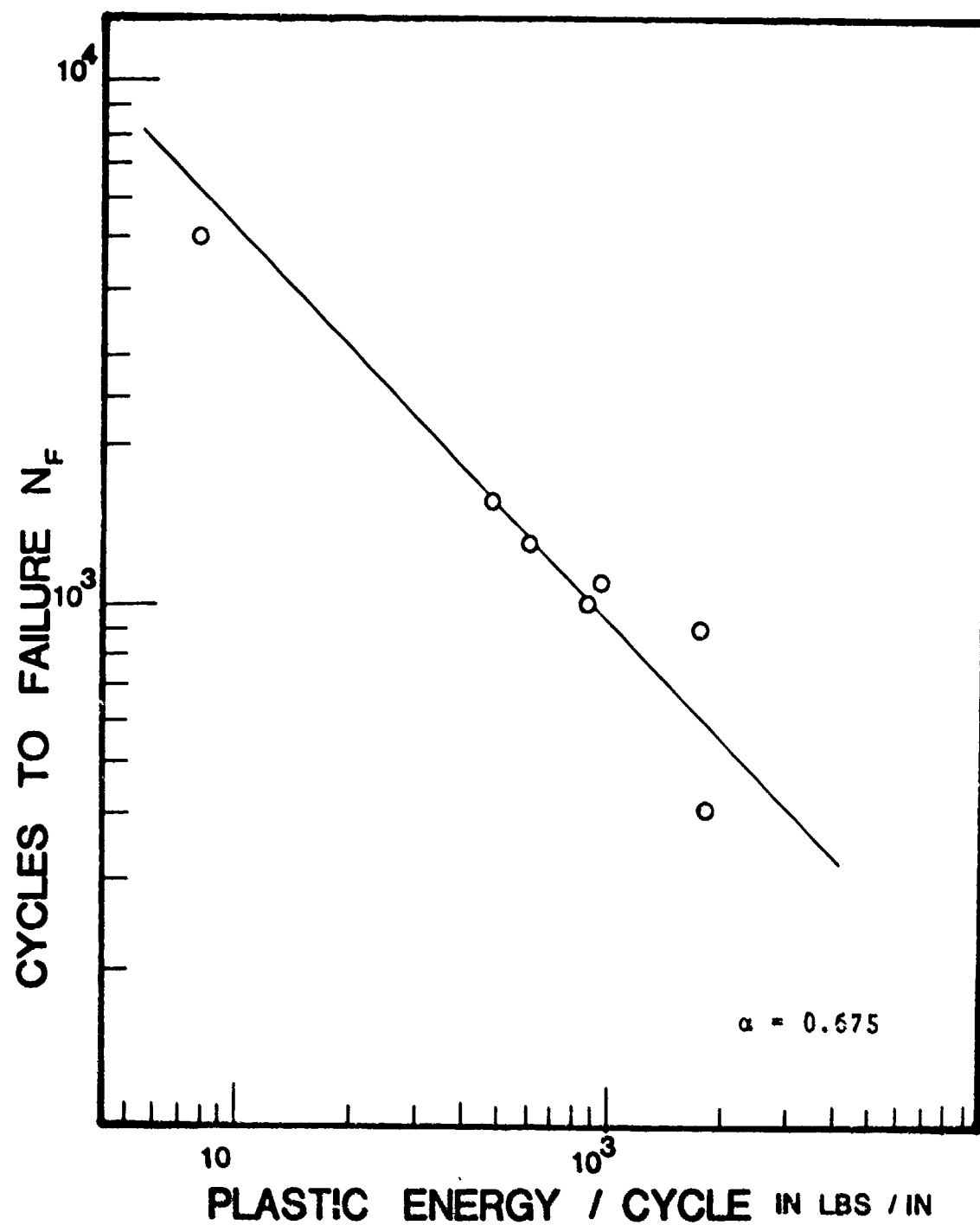


Fig. 50. Cycles to failure vs. plastic work/cycle for AF 1410 aged at 950°F for 5 hrs.

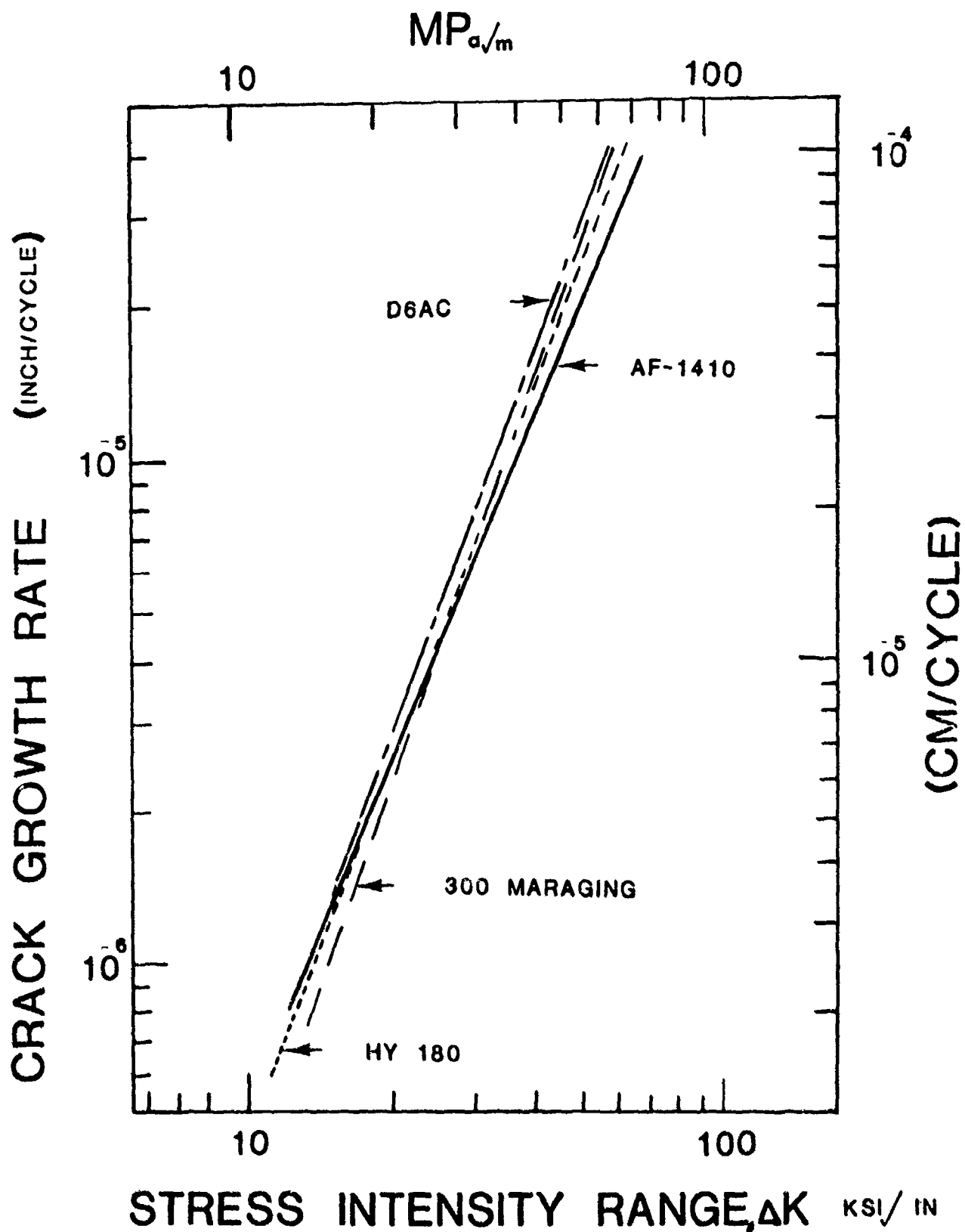


Fig. 51. Comparison of fatigue crack growth behavior of AF 1410 steel with D6Ac, HY 180 and 300 maraging steel. Data for these materials, except AF 1410 steel, obtained from ref. 28.

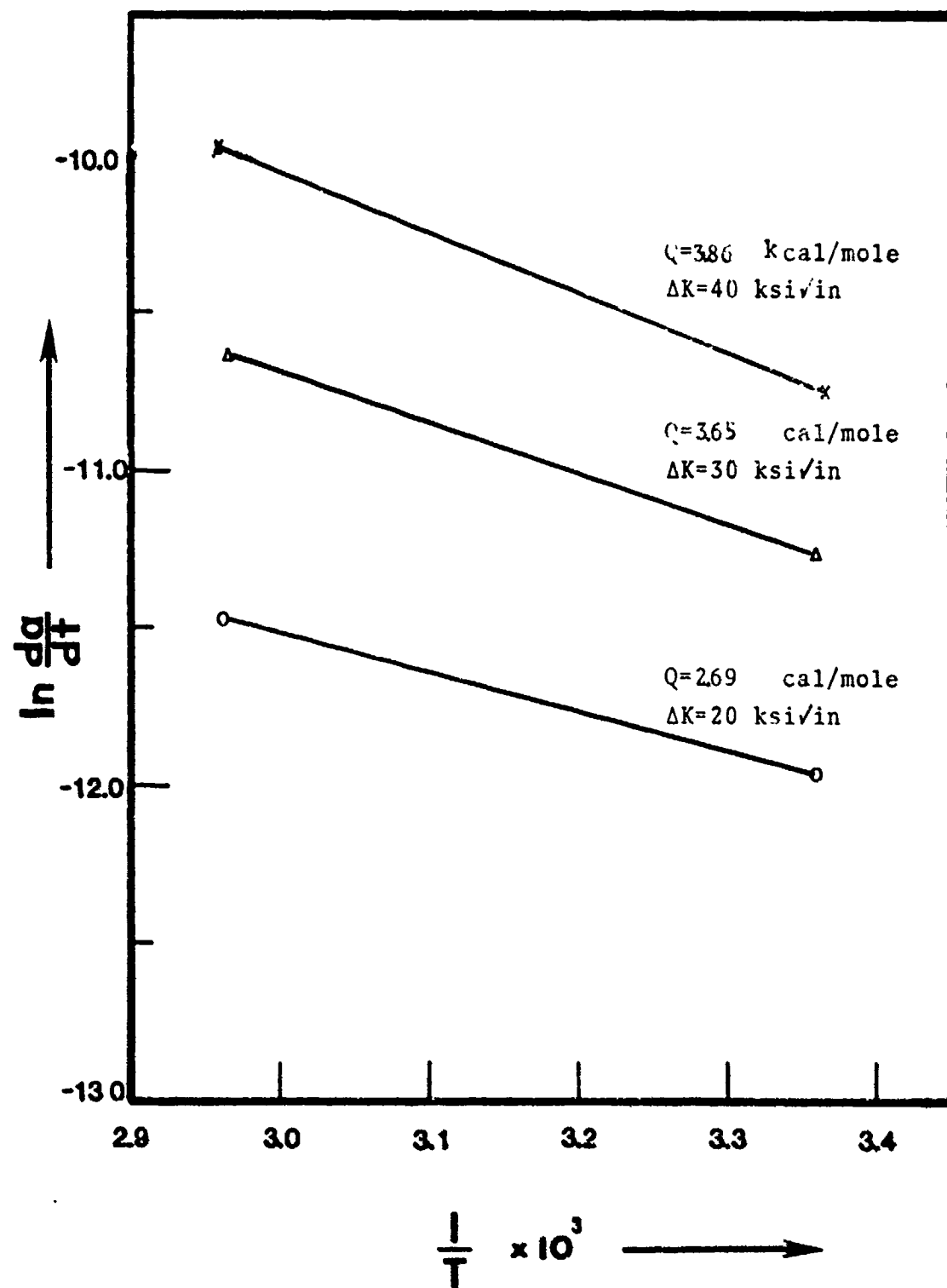


Fig. 52. Plot of $\ln \left(\frac{da}{dT} \right)_{cf}$ versus $\frac{1}{T} (^{\circ}\text{K}^{-1})$ at indicated stress intensity levels.

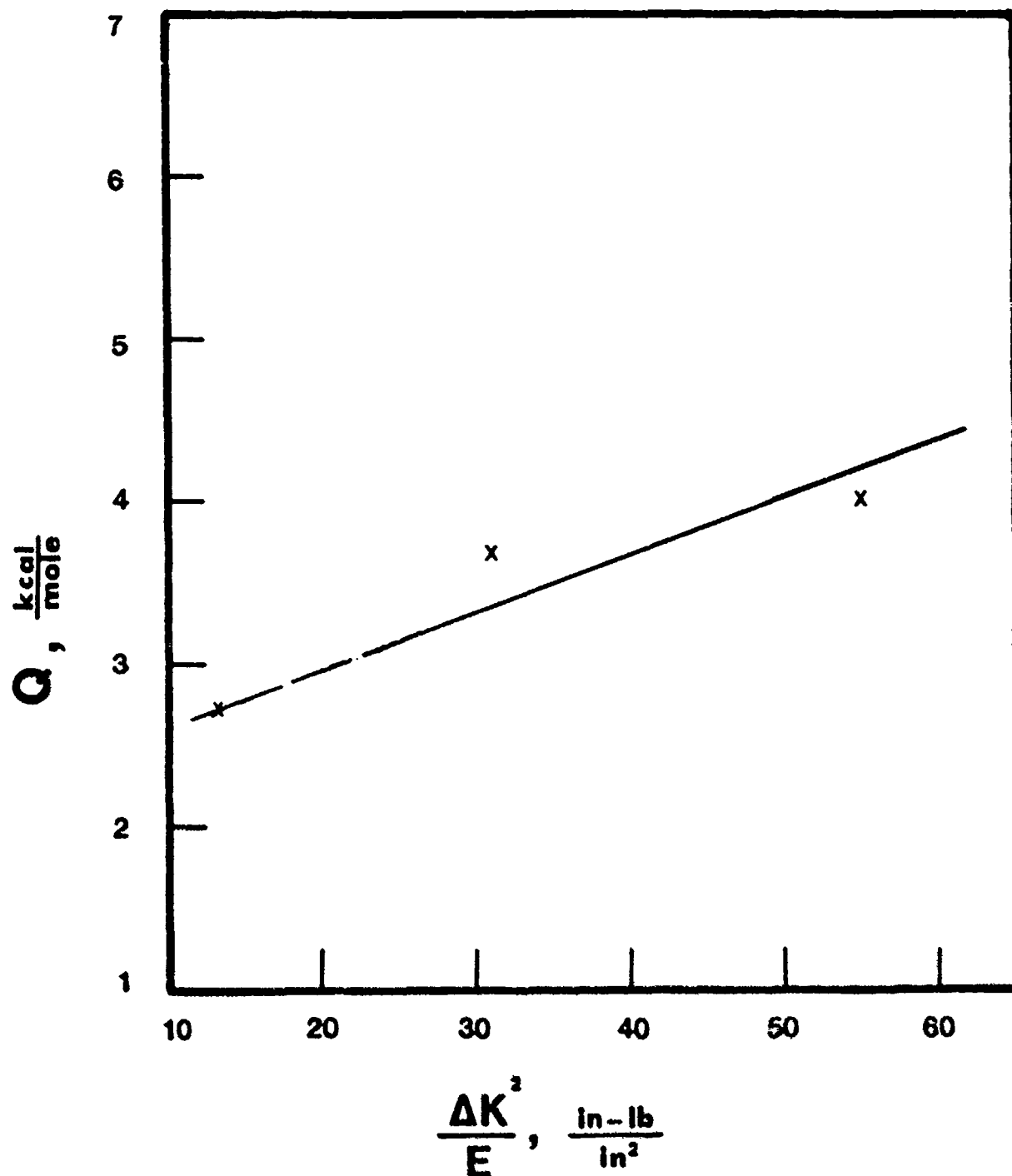


Fig. 53. Plot of Q versus $\frac{\Delta K^2}{E}$ to obtain the characteristic activation energy. ($E=29 \times 10^3$ ksi)

REFERENCES

1. J. A. Snide, Ph.D. Dissertation, The Ohio State University, 1975.
2. G. R. Speich, D. S. Dabkowski and L. F. Porter: Met. Trans., 4, 1973, p. 303.
3. C. D. Little and P. M. Machmeier: AFML-TR-75-148, Sept. 1975.
4. J. R. Patel and M. Cohen: Acta.Met., 1, 1953, p. 504.
5. Stephen D. Antolovich and B. Singh: Met. Trans., 2, 1971, p. 2135.
6. Stephen D. Antolovich, Ashob Saxena and G. R. Chanani: Met. Trans., 5, 1974, p. 623.
7. Stephen D. Antolovich: Trans. AIME, 242, 1968, p. 2371.
8. Stephen D. Antolovich and Dieter Fahr: Eng. Fr. Mech., 4, 1972, p. 133.
9. Stephen D. Antolovich, T. R. Risbeck, A. Saxena and Y. Kawabe: Paper in press, Eng. Fr. Mech. To appear in 1980.
10. James E. Collipriest Jr. and Richard M. Ehret: Rockwell International Space Division, Report #SD-74-CE-0001, 1974.
11. P. B. Hirsch, A. Howie, R. B. Nicholson, D. W. Pashley and M. J. Whelan: Electron Microscopy of Thin Crystals, Butterworths, London, 1965.
12. C. E. Feltner and C. Laird: Acta. Met., 15, 1967, p. 1621.
13. A. Aizaz: M.S. Thesis, University of Cincinnati, 1978.
14. Shahid Bashir, Philippe Taupin and Stephen D. Antolovich: Met. Trans., 10A, 1979, p. 1481.
15. M. Clavel and A. Pineau: Met. Trans., 9A, 1978, p. 471.
16. T. H. B. Sanders: Ph.D. Dissertation, Georgia Institute of Technology, 1974.
17. J. Morrow: ASTM STP 378, 1965, p. 45.

18. Ashok Saxena and Stephen D. Antolovich: Met. Trans., 6A, 1975, p. 1809.
19. B. Tomkins: Phil. Mag., 18, 1968, p. 1041.
20. D. S. Dugdale: J. Mech. Phys. Solids, 8, 1960, p. 100.
21. L. F. Van Swam, R. N. Pelloux and N. J. Grant: Met. Trans., 6A, 1975, p. 45.
22. J. T. McGrath and W. J. Bratina: Acta. Met., 15, 1967, p. 329.
23. O. T. Woo, B. Ramaswami, O. A. Kupcis and J. T. McGrath: Acta. Met., 22, 1974, p. 385.
24. R. A. Fournelle, E. A. Grey and M. E. Fine: Met. Trans., 7A, 1976, p. 669.
25. A. Abel and R. K. Ham: Acta. Met., 14, 1966, p. 1489.
26. S. K. Das and G. Thomas: ASM Trans. Quart., 62, 1969, p. 659.
27. G. Thomas: Iran and Steel Intul, 1973, p. 454.
28. J. M. Barsom, E. J. Imhof and S. T. Rolfe: Eng. Fr. Mech., 2, 1971, p. 301.
29. P. J. Bania and Stephen D. Antolovich: ASTM STP 610, 1976, p. 157.
30. Li Chung Jea: M.S. Thesis, University of Cincinnati, 1974.
31. G. Limestahl: M.S. Thesis, University of Cincinnati, 1976.